

NUREG/CR-1509/3of4  
SAND80-1304/3of4

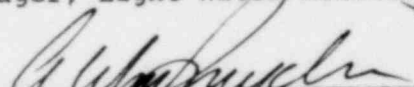
LIGHT WATER REACTOR SAFETY RESEARCH PROGRAM  
QUARTERLY REPORT, JULY-SEPTEMBER 1980

Person in Charge: Marshall Berman

Date Published: February 1981

APPROVED:

  
\_\_\_\_\_  
Manager, Light Water Reactor Safety Department

  
\_\_\_\_\_  
Director, Nuclear Fuel Cycle Programs

Sandia National Laboratories  
Albuquerque, NM 87185  
Operated by  
Sandia Corporation  
for the  
U.S. Department of Energy

Prepared for  
Division of Reactor Safety Research  
Office of Nuclear Regulatory Research  
U.S. Nuclear Regulatory Commission  
Washington, D.C. 20555  
Under Memorandum of Understanding DOE 40-550-75  
NRC FIN Nos. A-1019, -1030, -1227, -1237

8104230928

## CONTENTS

	<u>Page</u>
1. Molten Fuel/Concrete Interactions Study	11
1.1 Summary	11
1.2 CORCON Model Development	13
1.2.1 Improvements to CORCON-MODO	13
1.2.2 Models for Mel. Phase Liquidus and Solidus Temperatures	15
1.2.3 Decay Heat Generation Model	17
1.2.4 Code Comparison Test Analysis	18
1.3 References	28
2. Steam Explosion Phenomena	29
2.1 Summary	29
2.1.1 Small Scale Experiments	30
2.1.2 Fully Instrumented Test Series	30
2.1.3 Modelling and Analysis of Steam Explosions	31
2.1.4 Containment Failure Analysis	31
2.2 Small Scale Experiments	31
2.2.1 Controlled Atmosphere Chamber	31
2.2.2 Iron-Oxide Drop Experiments Performed in Argon	31
2.2.3 Debris Particle Sizes	31
2.2.4 Effect of Melt Viscosity on Steam Explosions	33
2.3 Fully Instrumented Test Series	37
2.3.1 FITS Experiments	41
2.3.2 Conclusions	47
2.4 Modelling and Analysis of Steam Explosions	50
2.5 Containment Failure Analysis	50
2.6 References	50
3. Separate Effects Tests for TRAP Code Development	53
3.1 Chemical Experiments	53
3.2 Interim Raman System	54
3.3 Fission-Product Reaction Facility (FPRF)	58
3.4 References	61

CONTENTS (Cont'd)

	<u>Page</u>
4. Containment Emergency Sump Performance	63
4.1 Summary	63
4.2 Test Facility	63
4.3 Test Program Planning Status	65
4.4 Data Analysis	66
4.5 Preliminary Data	66
5. Hydrogen Program	75
5.1 Summary	75
5.2 The Hydrogen Compendium	75
5.3 Hydrogen Mitigation Techniques for Sequoyah	76
5.3.1 Deliberate Ignition	76
5.3.2 Water Fogging	77
5.3.2.1 Water Fogs in Deflagrations	77
5.3.2.2 Water Fogs in Detonations	80
5.3.3 Halon Inerting	81
5.4 Combustion Analyses	82
5.4.1 Combustion Code Development	83
5.4.2 Detonation Code Development	85
5.4.3 CSQ Detonation Calculations	93
5.5 Hydrogen Instrumentation	93
5.5.1 Introduction	93
5.5.2 Gas Detection Equipment Suppliers	98
5.5.3 Gas Detection Equipment	99
5.5.4 Comments on Equipment	100
5.6 References	102
6. Combustible Gas in Containment Program	105
6.1 Summary	105
6.2 Zinc Inventory Investigation	105
6.3 Study of Hydrogen Generation Rates	107

## ILLUSTRATIONS

<u>Figure</u>		<u>Page</u>
1.1	Liquidus and Solidus Temperatures for Fe-Cr-Ni System	16
1.2	Effect of Mass Loss on the Core Decay Power	19
1.3	Melt Temperature Sensitivity to Selected Time Step	20
1.4	Melt Layer Temperatures as a function of Time	22
1.5	Melt Layer Mass as a function of Time	23
1.6	Melt Layer Density as a function of Time	24
1.7	Melt Layer Void Fraction as a function of Time	25
1.8	Interfacial Layer Depth as a function of Time	26
1.9	Maximum Axial and Radial Penetration as a function of Time	27
2.1	Experimental Apparatus for High Ambient Pressures	32
2.2	Cumulative Mass Average Debris Distribution for Test N-79-3	34
2.3	Debris Mass Average Diameter as a function of Applied Peak Pressure	35
2.4	Debris Mass Average Diameter as a function of Explosion Peak Pressure	36
2.5	Alumina-Silica Debris from a Droplet Experiment with no Explosion	38
2.6	Water Phase Pressure History near the wall for FITS Test-3A	42
2.7	Chamber Air Pressure History for FITS-3A	43
2.8	FITS-3A Particle Size Data	45
2.9	FITS-4A Particle Size Data	46
2.10	Experimental Water Chamber used for FITS-5A	48
2.11	FITS-5A Particle Size Data	49

ILLUSTRATIONS (Cont'd)

<u>Figure</u>		<u>Page</u>
3.1	Vapor Pressure of CsI and CsOH	55
3.2	Schematic Diagram of the Interim Cell	56
3.3	Schematic Diagram of the Experimental Raman Setup	57
3.4	Pure rotational Stokes Raman spectra of hydrogen recorded in the interim cell	59
3.5	Plot of the rotational term value, $F_0(J)$ , versus the logarithm of normalized intensity	60
3.6	Schematic diagram of the Fission Product Reaction Facility (FPRF)	62
4.1	Plan and Sections of the Facility	64
4.2	Vortex Strength and Void Fraction for a Steady State Test (30 Minutes)	67
4.3	Hydraulic Gradient for the Two Outlet Pipes for a Steady State Test (30 Minutes)	68
4.4	Vortex Strength and Void Fraction for a Steady State Test (30 Minutes)	70
4.5	Vortimeter Revolutions for the Two Outlet Pipes for a Steady State Test (30 Minutes)	71
4.6	Typical Initial Results for Average Vortex Strength as Functions of Flow Rate and Submergence	72
4.7	Typical Air Core Vortex in the Containment Sump at a Low Water Level	73
4.8	Typical Air Core Vortex in the Containment Sump at a High Water Level	74
5.1	Effect of Droplet Vaporization on Adiabatic Isochoric Hydrogen Combustion	78
5.2	Effect of Droplet Vaporization on Adiabatic Isochoric Hydrogen Combustion	79
5.3	Frame of Reference Stationary Relative to (a) Detonation Wave Approaches the Wall (b) Reflected Shock Wave Leaves the Wall	87
5.4	Theoretical Detonation Properties	88
5.5	Theoretical Detonation Properties	89

ILLUSTRATIONS (Cont'd)

<u>Figure</u>		<u>Page</u>
5.6	Theoretical Detonation Properties	90
5.7	Density Field in Zion CSQ Calculation at 25 ms	94
5.8	Density Field in Zion CSQ Calculation at 35 ms	95
5.9	Density Field in Zion CSQ Calculations at 45 ms	96
5.10	Pressure at center of Zion roof	97

TABLES

<u>Table</u>		
1.1	Power Comparison (Large PWR)	17
1.2	Input Values for Analysis of Code Comparison Test #1	21
2.1	Viscosities of Melts which Participated in Steam Explosions in Sandia's Laboratory Scale Experiments	29
2.2	Viscosities of Melts Reported to have Exploded in Steam Explosion Interactions	40
2.3	FITS 2A Initial Conditions	41
2.4	FITS 4A Initial Conditions	44
2.5	FITS 5A Initial Conditions	47
6.1	Inventory of Zinc in Several LWR Power Plant Containments	106

LIGHT WATER REACTOR SAFETY RESEARCH PROGRAM  
QUARTERLY REPORT, JULY-SEPTEMBER 1980

1. Molten Fuel/Concrete Interactions Study

(T. J. Bartel, R. K. Cole, M. L. Corradini, J. F. Muir, D. A. Powers)

1.1 Summary

The Molten Fuel Concrete Interactions (MFCI) study is comprised of experimental and analytical investigations of the chemical and physical phenomena associated with interactions between molten core materials and concrete. Such interactions are possible during hypothetical fuel melt accidents in light water reactors (LWR's). Our main purpose is to identify and understand the dominant phenomena in order to evaluate the following:

1. The generation rate and nature of evolved noncondensable gases.
2. The effects of gas generation on fission product release.
3. The mechanism, rate, and directional nature of concrete erosion by the melt.

In addressing this objective, the experimental program was divided into four distinct areas:

1. Deposition of Corium-type melts onto concrete.
2. Kinetics and stoichiometry of the thermal decomposition of concrete.
3. Response of concrete to high heat fluxes at one surface.
4. Simulation experiments exploring phenomena at the interface between a melt and a decomposing solid.

The analytical program is directed toward the development of a computer model of molten core material concrete interactions capable of providing quantitative estimates of reactor fuel-melt accident situations. This effort was undertaken in two phases:

1. Development of a preliminary interaction model based on the earliest results from the experimental program - INTER.
2. Development and assessment of an improved interaction model that involves a more detailed and refined treatment of the interaction phenomena - CORCON.

CORCON development activities during the quarter encompassed a variety of subjects including numerical and coding changes and improvements, the development of new phenomenological models, and the application of CORCON-MOD0<sup>+</sup> to the Code Comparison Test Analysis.

Code improvement activities included: modifications to the concrete and melt enthalpy calculation procedures; incorporation of pool heat transfer coefficient correlations; corrections to the void fraction, level swell, and bubble size and velocity calculations;

clean-up and simplification of coding; correction of miscellaneous programming and modelling errors; user oriented modifications of the input/output sections; and improvement of the plot routines. An improved version of the code, CORCON-MOD1, is nearing completion. A topical-report/users-manual describing this version is in preparation.

Subroutines CONFND and CPENTH were modified to permit extrapolation of liquid-phase enthalpies below, and solid-phase enthalpies above, the normal melting temperature of any condensed species. This allows the latent heats of fusion of all species in a mixture to be accounted for between the mixture liquidus and solidus temperatures. For simplicity, we assume a constant specific heat between all-species-liquid and all-species-solid states at the corresponding temperatures. Further, the enthalpy change associated with other phase changes, or with melting of a species in a non-interacting mechanical mixture, is spread over an arbitrary range of  $\pm 5^\circ\text{C}$  around the normal species melting temperature.

Curve fits of enthalpy versus temperature built into the code for the three default concretes were replaced with an internal enthalpy calculation. This was done to eliminate an inconsistency between the enthalpies calculated for the solid concrete surrounding the molten pool the molten concrete after it enters the pool. The new procedure duplicates the one used to generate the original curves. It is consistent with the scheme for computing the enthalpy of core melt constituents and uses the data base embodied in CPENTH and CONFND.

The constant pool heat transfer coefficients employed in CORCON-MOD0 were replaced with empirically-based correlations recommended by F. G. Blottner. Although these introduced more realism into the model, they resulted in substantially higher interlayer and pool surface heat transfer and excessive cooling of the melt. In an effort to improve the realism of the correlations without changing their formulations, the pure liquid viscosity contained therein was replaced with a two-phase slurry viscosity to account for the appearance of suspended solids when the melt temperature falls below the liquidus line. The results of this modification are still being assessed, and further work in this area is clearly needed.

Two new models were developed for inclusion in CORCON. The first, which is essential to many of the modifications mentioned above, consists of a method for determining the liquidus and solidus temperatures of the metallic and oxidic phases of the melt. A scheme for the metallic phase, based on the Cr-Fe-Ni ternary system, has been completed, checked-out, and incorporated into CORCON. The situation for oxidic mixtures is much more complex and is hampered by a dearth of experimental data. Several models are possible and are currently being investigated.

The second model determines the internal heat generation within the melt due to nuclear decay of radioactive elements in the melt. It considers the composition of the melt at the time it is deposited on the concrete (i.e., the elemental mass loss during the meltdown phase), the elemental decay from accident initiation, and the mass loss by aerosol generation during the melt/concrete interaction. The model has been programmed and checked as a stand-alone code and is presently being incorporated into CORCON.

Calculations using two slightly different versions of CORCON-MOD0<sup>+</sup> (improved initial version) were performed as part of a continuing analysis of Code Comparison Test No. 1. A preliminary study of the sensitivity of the predictions to timestep size showed them to be independent of step size for timesteps less than  $\sim 15$  s. Comparison



of the measured and predicted melt temperature histories reveals that: 1. quantitative agreement is relatively good, the differences being less than  $\sim 60^\circ\text{C}$ , and 2. After an initial sudden drop in temperature (exhibited by both), the data follow a pronounced linearly upward trend while the code predictions exhibit a steady, almost imperceptible decrease in temperature with time. Possible causes of the differences between the experimental and predicted variations include the use of too high an initial melt temperature and too low a concrete ablation temperature in the computations. Both of these effects are being investigated.

## 1.2 CORCON Model Development

Development of an improved molten core/concrete interaction model, CORCON, continued. CORCON is a user oriented computer program written in a modular structure in which most computational units are contained in separate subroutines. Maximum use is made of existing codes and subroutines. Phenomenological models developed for the code have relied heavily on existing techniques, and experimental data and correlations available in the literature. Numerous input options provide a flexibility that enables a variety of problems to be solved by merely changing input data.

### 1.2.1 Improvements to CORCON-MOD0

A major concern in CORCON continues to be proper modelling of the thermodynamic properties of the melt when the temperature of a layer (phase) is either near the freezing point of one of its constituents, or between the liquidus and solidus temperatures of the mixture. To this end, we rewrote subroutine CONFND, which provides access to specific heat data for the calculation of enthalpies and chemical potentials. This was done primarily to allow extrapolation of species liquid properties below their normal freezing points so that the latent heats of fusion of the constituents of a mixture could be accounted for between the mixture liquidus and solidus temperatures. The revised routine will return for each species,  $i$ , either: 1. values appropriate to the isolated species in its equilibrium phase at the mixture temperature; 2. values for the species liquid phase, extrapolated below its freezing temperature, if necessary; and 3. values for the species solidus phase, extrapolated above its melting temperature, if necessary. The choice is controlled by a parameter in the calling statement. The second and third choices are, of course, invalid for gaseous species. For the equilibrium case, 1. a change was made to eliminate the discontinuity in the enthalpy of a species at its freezing point (latent heat of fusion) by the use of an effective specific heat in the temperature range  $T_{i\text{freezing}} \pm 5^\circ\text{C}$ . This defines effective "liquidus" and "solidus" temperatures for the species and allows linear interpolation in species enthalpy over the prescribed freezing temperature range.

The specific heat data structure was also modified so that only handbook values (no derived quantities) appear in the data tables. This facilitates checking and updating of the tables. For convenience, the updating procedure has been automated.

Subroutine CPENTH, which generates appropriate calls to CONFND and then evaluates the specific heat and enthalpy of a mixture, was also modified. The routine will now return results appropriate either to a mechanical mixture (with each species melting at its normal melting point) or to a solution (with all latent heat accounted for between the liquidus and solidus temperatures of the solution). In the latter case, species liquid properties (extrapolated if necessary) are used above

the liquidus point, solid properties below the solidus, and a constant effective specific heat is assumed between these temperatures.

CORCON-MOD0 contains fits to curves of enthalpy versus temperature for each of the three default concretes built into the code. These curve fits are used to evaluate the change in concrete enthalpy as the virgin concrete is heated to its ablation temperature. The change in enthalpy of condensed concrete ablation products from ablation temperature to pool temperature, however, is calculated using subroutine CPENTH. These two procedures have been found to be inconsistent, with the result that the total energy necessary to raise virgin concrete to the pool temperature is a function of the ablation temperature. To rectify this, the curve fits have been replaced by an internal enthalpy calculation that duplicates the one used to generate the original curves, but uses the data base embodied in CPENTH and CONFND. In addition to being consistent, the new procedure simplifies the input needed for a non-standard concrete in that the concrete heat of ablation is no longer required.

Convective heat transfer within the molten pool (bulk-to-periphery and between layers) is modelled in CORCON-MOD0 using constant heat transfer coefficients. These have been replaced with correlations recommended by F. G. Blottner.<sup>1,2</sup> Unfortunately, subsequent calculations for the Code Comparison Test conditions have shown that these correlations yield interlayer heat transfer substantially higher than anticipated, resulting in excessive cooling of the melt. We are presently investigating whether this is caused by the inability of the correlations to properly model the physical phenomena involved or by incorrect values of the material properties used in the correlations.

In their original form, the heat transfer coefficient correlations apply only to a completely liquid melt. To obtain realistic results at melt temperatures below metallic or oxidic phase liquidus temperatures, the correlations must be modified to account for partial freezing of the melt (i.e., the precipitation of solids). As a simple first attempt in this regard, we have replaced the pure liquid viscosity in the correlations with a two-phase slurry viscosity, using the Kunitz<sup>3</sup> two-phase multiplier to account for suspended solids when the temperature drops below the liquidus value. We are currently evaluating this factor at the layer interface temperature, rather than at its bulk temperature, because it is felt that this will be more representative of conditions in the outer region of the thermal boundary layer. Further work in this area is clearly needed. We are not entirely satisfied with the changes described above, and feel that improvement of the heat transfer correlations should have a high priority in future CORCON development activities.

The level-swell calculation in CORCON-MOD0 is not fully self-consistent. A z-dependent void fraction,  $\alpha(z)$ , is computed using start-of-timestep pool layer (i.e., melt material) locations; the quantity  $(1 - \alpha(z))A_R(z)dz$  is then integrated using end-of-timestep concrete cavity geometry and pool layer volumes to find end-of-timestep layer interfaces. Thus, the void fraction used to calculate the swell of one layer could have been determined from properties of a different layer. In some cases, this was found to lead to an "alternation instability," with one layer geometry on even-numbered timesteps and another on odd-numbered. Therefore, subroutine LEVSWL was rewritten to combine the two calculations, so that  $\alpha(z)$  is calculated for the melt material actually present during the integration to determine interfaces. This has eliminated the problem.

Changes were also made in subroutine BUBBLE, which computes bubble sizes and velocities, to conserve the number of bubbles crossing layer interfaces and to eliminate the nucleate and patchy bubbling regimes used in determining the size of bubbles formed when the concrete decomposition gases enter the pool. The nucleate bubbling regime was found to yield extremely small bubbles and very large void fractions. Experimental evidence available to date does not indicate that these conditions exist for core/concrete interactions.

Additional CORCON improvement activities included: clean-up and simplification of coding; correction of miscellaneous programming and modelling errors; user oriented modifications of the input/output sections; and improvement of the plot routines. An improved version of the code, CORCON-MOD1, is in the final stages of preparation. A topical report/users manual is being written to document this version of CORCON. Sections describing the essential characteristics of the code and providing basic code documentation information (including subroutine descriptions, use of common, program flow chart, and subroutine call and called-from information) were written.

### 1.2.2 Models for Melt Phase Liquidus and Solidus Temperatures

Several of the changes described in the previous section require a knowledge of the liquidus and solidus temperatures for metallic and oxidic mixtures. In CORCON-MOD0 these were determined in a routine (SOLLIQ) adapted from the INTER code. This routine is no longer considered adequate, and is being replaced for CORCON-MOD1.

For metallic mixtures (at least late in the accident when freezing is likely) the principle constituents should be Cr, Fe, and Ni. Therefore, we have constructed a simple fit to the ternary Cr-Fe-Ni phase diagram,<sup>4</sup> with due consideration to the associated binary phase diagrams.<sup>5</sup> The liquidus and solidus fits are given by:

$$\begin{aligned}
 T_{liq} = \min & (1857 - 510W_{Fe} - 1140W_{Ni} , \\
 & 1536 - 90W_{Cr} - 440W_{Ni} , \\
 & 1455 - 200W_{Cr} - 40W_{Fe} , \\
 & 1520 - 230W_{Cr} - 130W_{Ni}) \quad (^\circ\text{C}) \\
 T_{sol} = \min & (1857 - 730W_{Fe} - 3310W_{Ni} , \\
 & 1536 - 90W_{Cr} - 560W_{Ni} , \\
 & 1455 - 250W_{Cr} - 100W_{Fe} , \\
 & 1510 - 310W_{Cr} - 140W_{Ni} , \\
 & 1340) \quad (^\circ\text{C})
 \end{aligned}$$

where  $W_{Cr}$ ,  $W_{Fe}$ , and  $W_{Ni}$  are the weight fractions of Cr, Fe, and Ni, respectively. These expressions agree with the original curves within a few tens of degrees. The corresponding contour maps are shown in Fig. 1.1.

The current coding ignores the presence of other elements in the metallic phase, and renormalizes so that  $W_{Cr} + W_{Fe} + W_{Ni} = 1.0$ . In later versions, it may be possible to include the effects of carbon

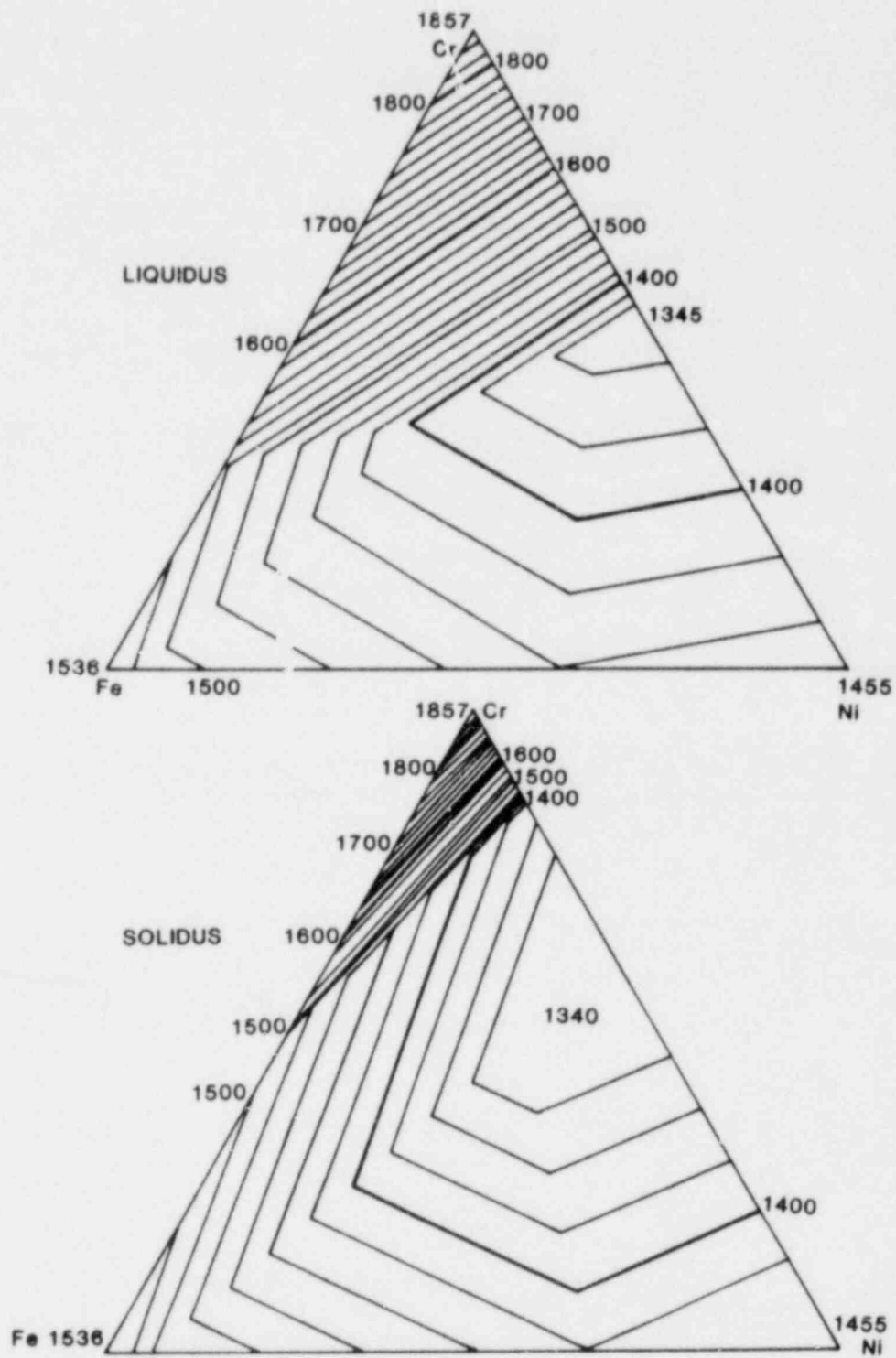


Figure 1.1 Liquidus and Solidus Temperatures for Fe-Cr-Ni System.

and zirconium, using a scheme similar to that which will be described for oxidic mixtures.

The situation for oxidic mixtures is much more complicated. It might be possible (though very difficult) to fit the ternary  $\text{CaO}$ ,  $\text{SiO}_2$ ,  $\text{Al}_2\text{O}_3$  system representing the principle constituents of concrete. The addition of  $\text{UO}_2$ ,  $\text{ZrO}_2$ , and metal oxides to such a fit seems practically impossible. Therefore, we intend to treat "concrete" as a species with liquidus and solidus temperatures either input by the user or given by built-in data. The liquidus and solidus temperatures for more general oxidic mixtures will be found from an empirical or semi-analytic representation of either a binary or a ternary system. In the binary case, the components would be concrete plus metal oxides and  $\text{UO}_2$  plus  $\text{ZrO}_2$ . For the ternary, they might be concrete, metal oxides, and  $\text{UO}_2$  plus  $\text{ZrO}_2$ , although the presence of metal oxides in concrete complicates the issue. Analytic expressions may be constructed assuming ideal solutions with either 1. a complete solubility in both liquid and solid phases, or 2. complete solubility in the liquid phase and complete insolubility in the solid phase. Work continues in evaluating these possibilities against very scanty experimental data.

### 1.2.3 Decay Heat Generation Model

A decay heat generation model has been developed, written and checked for CORCON. This model determines the internal heat generation in the melt region due to nuclear decay of radioactive elements in the melt. Three phenomenological considerations comprise the model: elemental decay, initial composition at the time of the concrete interaction, and mass loss during the interaction.

#### Elemental Decay

The model considers the decay of the important fission products, activated material, and actinides; 27 elements comprise the current list. Elements which did not contribute appreciable power during the 2000 frame under consideration, or were extremely volatile, e.g., Kr and Xe, were not included. Table 1.1 illustrates the difference between the decay power predicted by the present model and that computed with the SANDIA-ORIGEN code<sup>6</sup> (which considers over 100 isotopes). Although the deviation at early times appears large, it is due mainly to the contribution of Kr and Xe (not included in the model), which amounts to 8.1% and 4.2% at times of 0 and 0.1 day, respectively. The remaining difference is due to the numerous fast decay elements, e.g., Ga, Ge, As and Se.

Table 1.1

Power Comparison (Large PWR)			
-(day)	Present Model (MWt)	Sandia-ORIGEN (MWt)	Deviation (%)
0.	181.4	205.	11.5
.1	30.05	32.19	6.6
.4	21.33	21.41	.25
1.4	14.76	14.75	.05
4.0	10.40	10.44	.38

### Initial Composition

Several references<sup>7,8</sup> were evaluated for this phase of the model. It was concluded that the available prototypical data is at best sparse and contradictory. It was decided, therefore, that the loss fractions from WASH-1400<sup>7</sup> would provide a reasonable default estimate of the elemental masses at the initiation of the melt/concrete interaction. With the realization that these are scenario dependent, the code contains options which allow the initial masses or loss coefficients to be user-defined.

### Melt-Concrete Mass Loss

This phase of the process was the most difficult to model because virtually no data exist on this phenomenon. To the knowledge of the authors, the Powers experimentally determined aerosol generation model<sup>9</sup> is unique in this field. This model describes the amount of aerosol produced by vaporization, chemical reaction, and mechanical sparging. It was used to determine the mass loss from the melt during the interaction. The model determines an aerosol mass as a function of volumetric gas flow, melt temperature, and superficial gas velocity. The mass is then partitioned between the various chemical groups, e.g., alkali metals, dioxides, metals, etc. A simple exponential function is used to rapidly remove volatile elements remaining in the melt at the start of the interaction. A ten-minute half-life is assumed and the elemental masses reduced exponentially for three time constants. The fourth half-life is modelled as a linear ramp to zero mass.

### Model Evaluation

Figure 1.2 shows the effect of the mass loss models, both meltdown and concrete interaction, on the decay heat power. The calculations were made for a large PWR core. The upper curve represents the decay from the 27 elements in the model with no mass loss, while the lower curve incorporates the loss models described above. Consider the large displacement of the curves, approximately 3 - 6 MWt, in this time frame. This represents a significant fraction of the power available to the melt. The main reason for the difference is the release of the volatile elements Ba and I.

#### 1.2.4 Code Comparison Test Analysis

Further CORCON calculations were performed during the quarter as the analysis of Code Comparison Test No. 1 (CC-1) continued. The input values for these calculations are summarized in Table 1.2. A preliminary investigation was performed to evaluate the sensitivity of the predictions to time step size. This was conducted using CORCON-MOD0<sup>+</sup> (an improved initial version of the code containing constant bulk-to-interface heat transfer coefficients in the pool). The time step size was arbitrarily varied from 5 to 150 s. The results are shown in Figure 1.3.

DECAY HEAT GENERATION MODEL  
(LARGE PWR CASE)

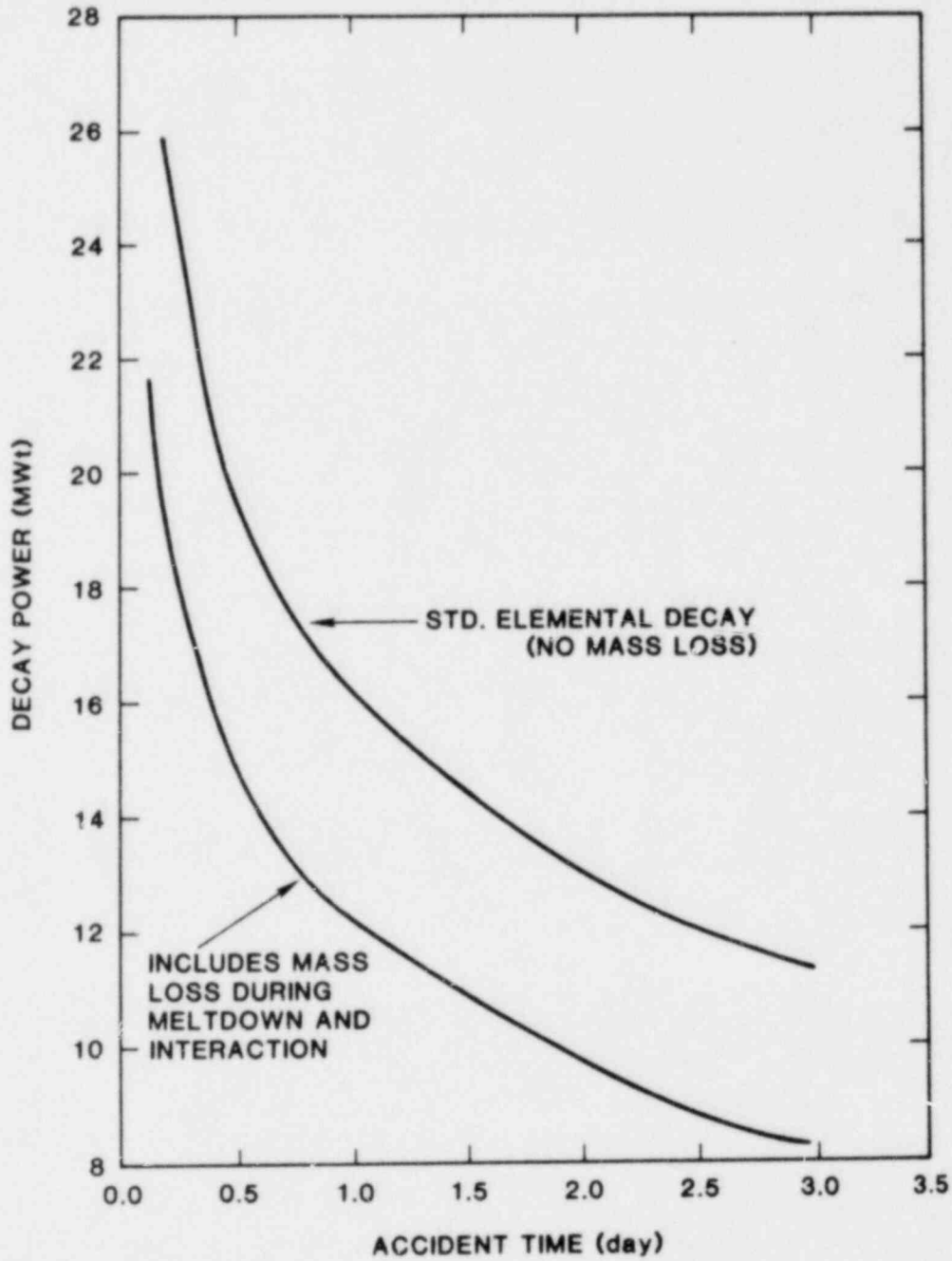


Figure 1.2 Effect of Mass Loss on the Core Decay Power.

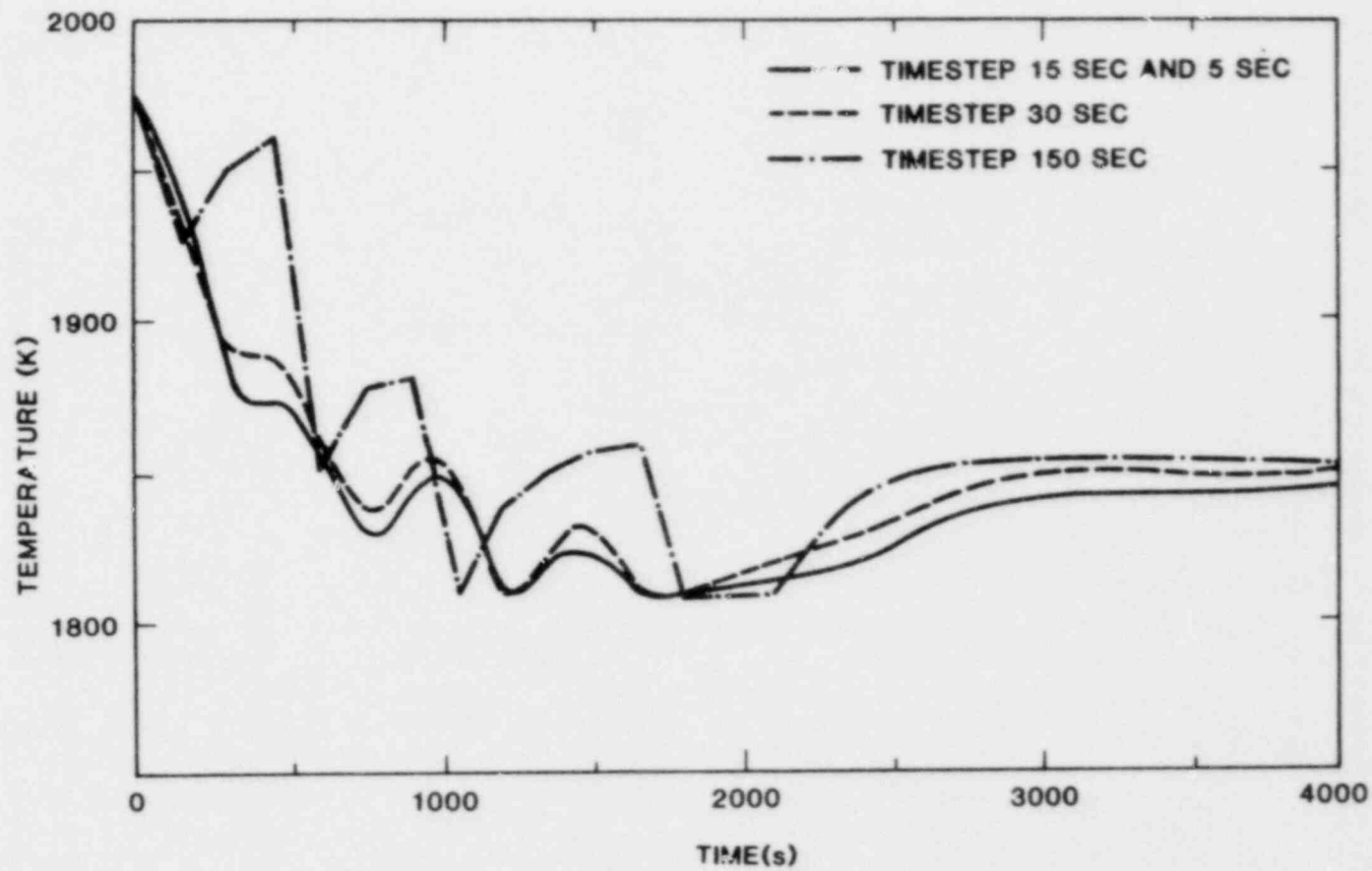


Figure 1.3 Melt Temperature Sensitivity to Selected Time Step.



Table 1.2

Input Values for Analysis of Code Comparison Test #1

Melt

Composition - Type 304 Stainless Steel  
 Mass - 205 kg  
 Temperature - 1975 K

Concrete

Composition - CRBR Limestone Concrete  
 Cavity Size - 19 cm radius  
                   38 cm height  
                   1 cm corner radius  
 Temperature - 300 K  
 Solidus-Liquidus Temp. - 1690 - 1875 K

Atmosphere

Composition - 20<sup>a</sup>/o H<sub>2</sub>, 25<sup>a</sup>/o CO, 35<sup>a</sup>/o CO<sub>2</sub>,  
                   1<sup>a</sup>/o H<sub>2</sub>O, 19<sup>a</sup>/o N<sub>2</sub>  
 Pressure - 0.083 MPa  
 Temperature - 473 K  
 Volume - 0.25 m<sup>3</sup>

Energy is supplied to the melt by an induction coil (~ 80 kW). The experimental power history curves have been reported previously<sup>9</sup>.

Note that the initial temperature oscillations superimposed on the melt cooldown are caused by an intermittent power history. Power to the induction heater was shut off periodically in order that melt temperature measurement could be made.

For  $\Delta t = 150$  s the code exhibited unphysical temperature oscillations early in the test when the steel melt was rapidly cooling down and when the power was being intermittently shut off. Later in time, it shows good agreement with the results using smaller timesteps. As the timestep was decreased to  $\Delta t = 15$  s, the temperature predictions converged to a single set of values. For timesteps smaller than  $\Delta t = 15$  s the results were unchanged. As the real problem time increases, it may be possible to increase the timestep size without sacrificing accuracy because the melt temperatures, ablation rates and other processes change much more slowly at longer times.

Further calculations were made following incorporation of the Blottner pool heat transfer coefficient correlations into CORCON. These calculations were made using a timestep of 15 s. The resulting temporal variations in the principal variables are presented in Figures 1.4 through 1.9. Once again, the curves exhibit variations (most noticeable in the temperature and void fraction variations) that correspond to the six intervals during the test when the power was shut off to make melt temperature measurements. The data from these measurements are included for comparison in Figure 1.4.

There are two observations that can be made at this time. First, the qualitative trend in the data is linearly upwards after a sharp initial cooldown. Secondly, the code predictions are always within 50 - 60°C of the data although the trend is a slow steady (almost imperceptible) cooldown, rather than a heatup, after 500 sec. One

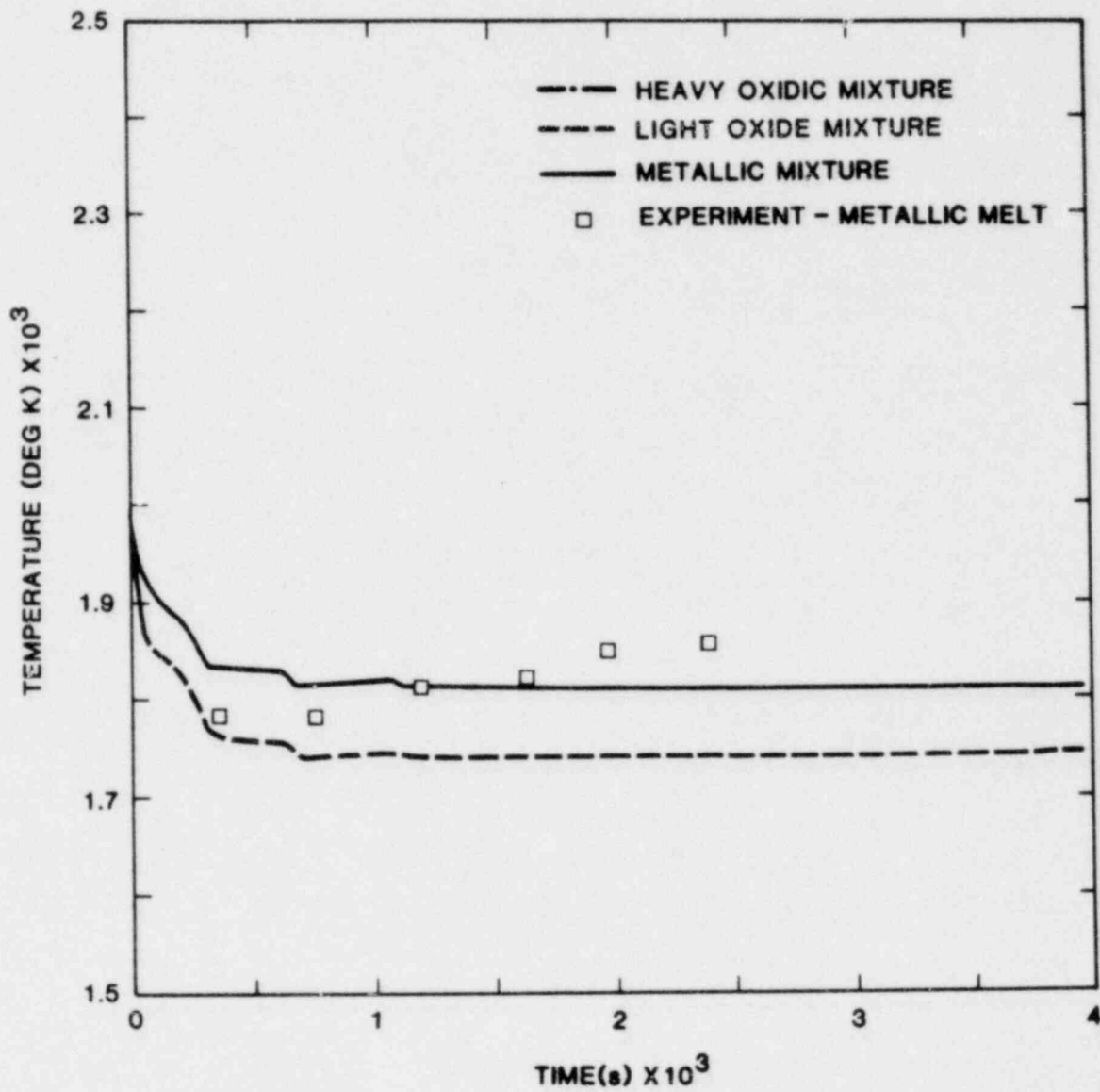


Figure 1.4 Melt Layer Temperatures as a function of Time.

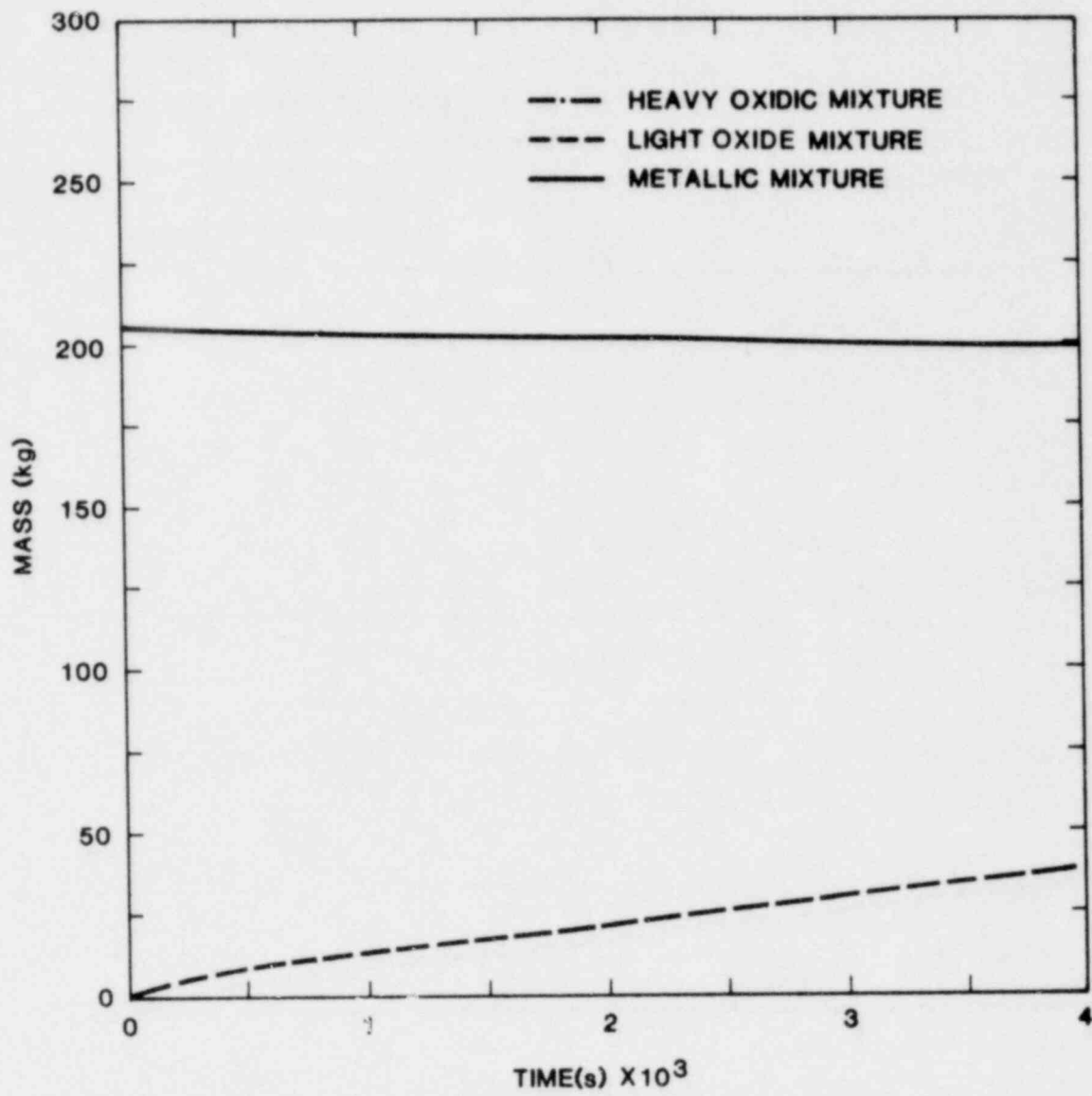


Figure 1.5 Melt Layer Mass as a function of Time.

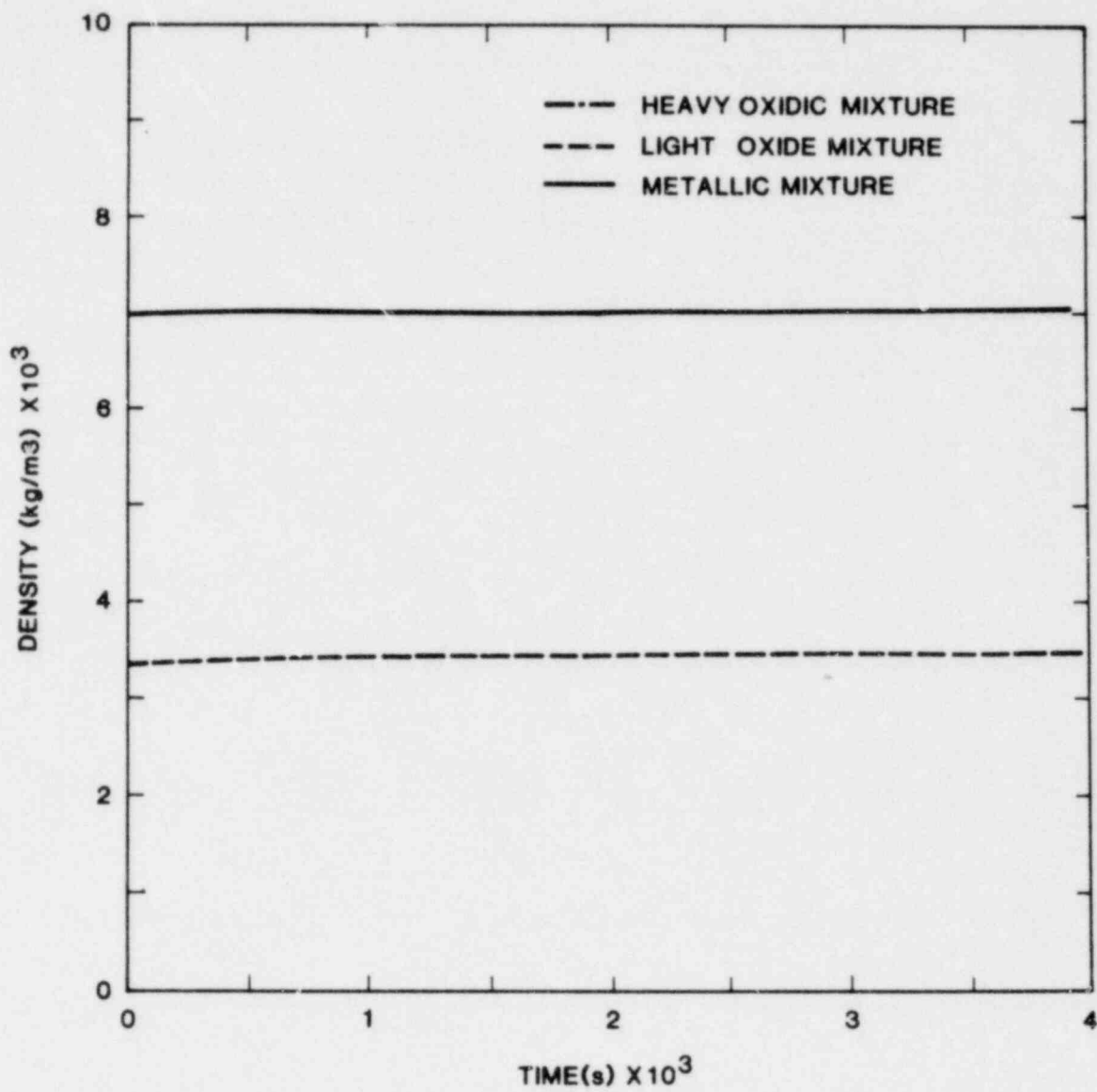


Figure 1.6 Melt Layer Density as a function of Time.

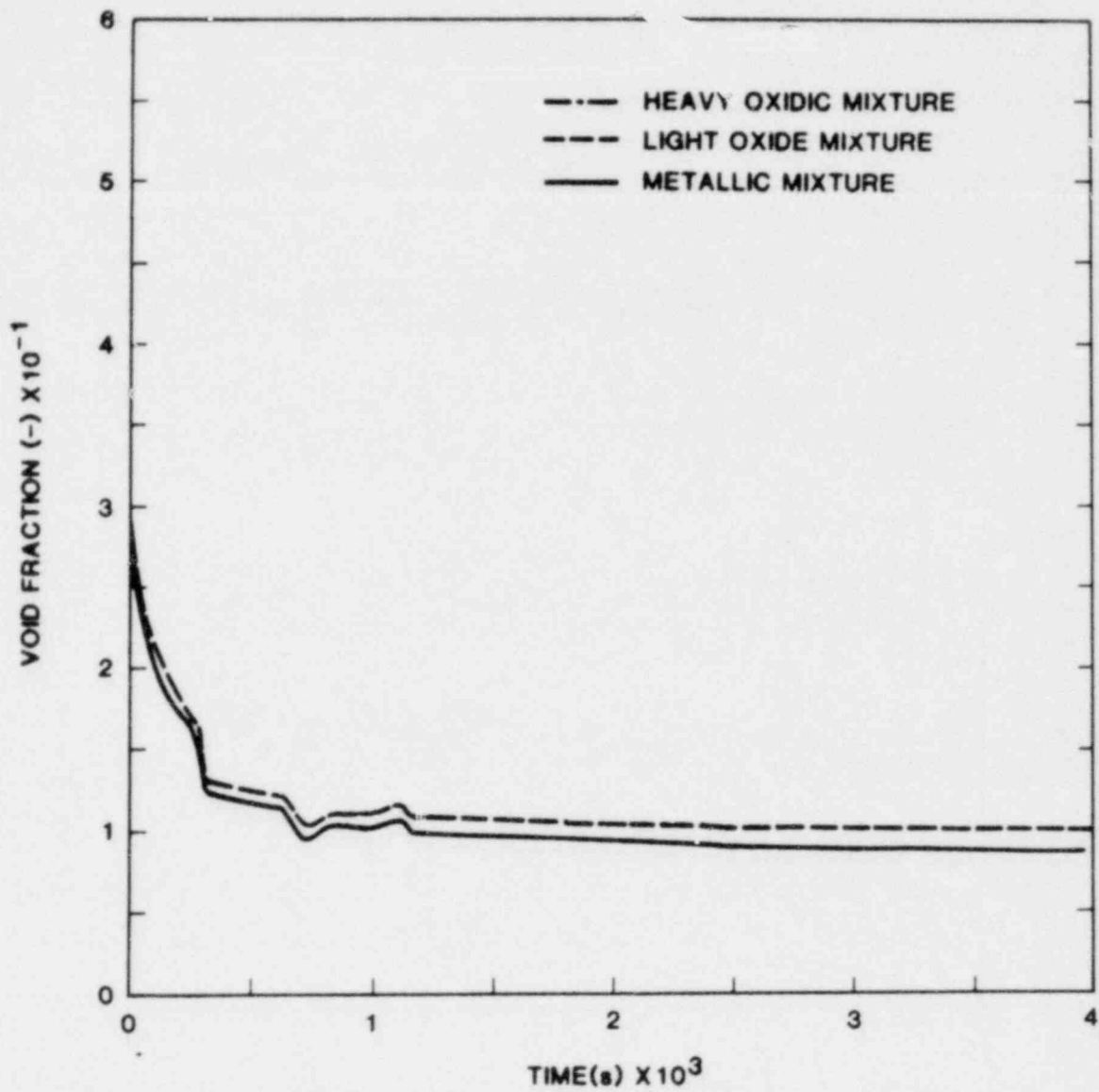


Figure 1.7 Melt Layer Void Fraction as a function of Time.

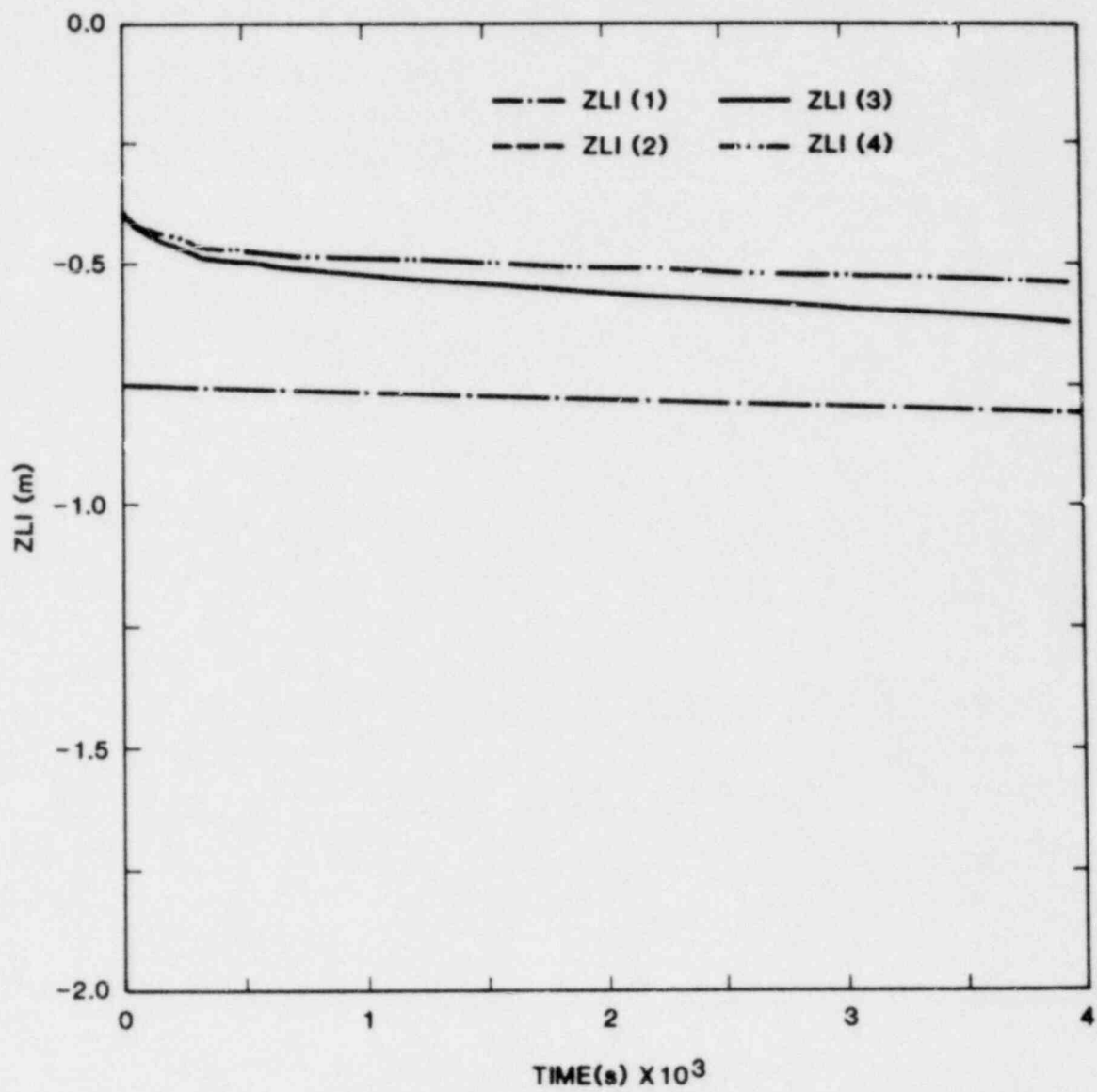


Figure 1.8 Interfacial Layer Depth as a function of Time.

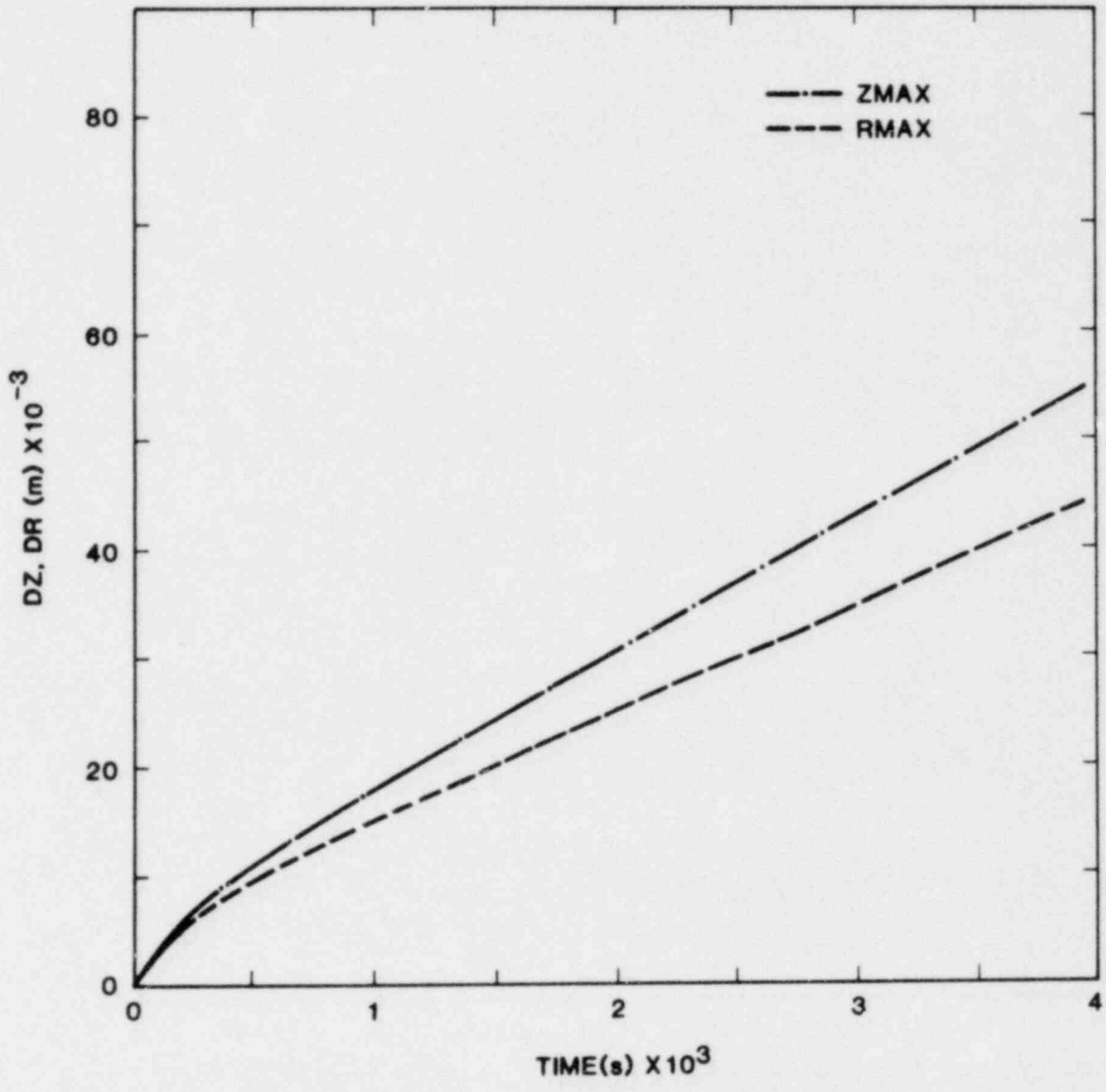


Figure 1.9 Maximum Axial and Radial Penetration as a function of Time.

reason for the initial over-prediction in melt temperature may be the use of too high an initial temperature in the calculation. Some cooling of the melt undoubtedly occurred during the 20 s pour period when 1. the melt was exposed as it cascaded from the furnace crucible into the test crucible, and 2. it then experienced a very energetic interaction with the concrete, enhanced by vigorous agitation produced by the combined effects of the pour and the initially high gas evolution from the concrete. Since CORCON assumes instantaneous deposition of the melt into the crucible, a lower "initial" melt temperature, representative of conditions at the end of the transient pour phase (which is not modelled in the code), would seem more realistic. This would result in lower melt temperatures throughout the test.

The qualitatively different shape of the predicted temperature variation may be due to the concrete ablation temperature used in the calculation (1750 K). This value was chosen somewhat arbitrarily to lie between the concrete solidus and liquidus temperatures. These two bounding temperatures, however, are not well known. If the concrete ablation temperature were actually higher, the melt would remain hotter for two reasons: 1. it would transfer less heat to the concrete, which would reduce the amount of concrete ablated, and 2. less heat would be lost to heating up concrete ablation products, which would enter the melt at a reduced rate and at a higher temperature. A reduction in the heat lost from the melt also suggests that its temperature would increase (for the same power input) as time progressed past the initial cooldown stage. Both of these effects are being investigated.

### 1.3 References

1. F. G. Blottner, Hydrodynamics and Heat Transfer Characteristics of Liquid Pools with Bubble Agitation, SAND79-1132 (NUREG/CR-0944), Sandia National Laboratories, Albuquerque, NM (November 1979).
2. Light Water Reactor Safety Research Program Quarterly Report April - June 1979, SAND79-2057 (NUREG/CR-1112), Sandia National Laboratories, Albuquerque, NM (February 1980).
3. Kunitz, Journal General Physiology, Vol. 9, p. 715 (1926).
4. G. R. Speich, p. 424 in Metals Handbook, Vol. 8, "Metallography Structures & Phase Diagrams by American Society for Metals," Metals Park, Ohio, 1973.
5. C. J. Smithells, Metals Reference Book, Vol. II (1967).
6. D. E. Bennett, SANDIA-ORIGEN User's Manual, SAND79-0299 (NUREG/CR-0987), Sandia National Laboratories, Albuquerque, NM (October 1979).
7. Reactor Safety Study, WASH-1400 (NUREG-75/014), Appendix VII, U. S. Nuclear Regulatory Commission (October 1975).
8. Core-Meltdown Experimental Review, SAND74-0382 (NUREG-0205), Sandia National Laboratories, Albuquerque, NM (March 1977).
9. D. A. Powers, "Empirical Description of the Rate of Aerosol Generation," Light Water Reactor Safety Research Program Quarterly Report January - March 1980, SAND80-1304/1of4 (NUREG/CR-1509/1of4), Sandia National Laboratories, Albuquerque, NM (July 1980).



## 2. Steam Explosion Phenomena

(M. L. Corradini, D. E. Mitchell, L. S. Nelson)

The two main purposes of the steam explosion phenomena program are: (1) To identify experimentally the magnitudes and time characteristics of pressure pulses and other initial conditions which are necessary to trigger and propagate explosive interactions between water and molten Light Water Reactor (LWR) materials; and (2) to assess the probability and consequences of steam explosions during postulated meltdown accidents in LWRs. The major efforts in this program encompass four areas:

- (i) Small scale experiments using simulant molten materials (Corium A, E, Iron-oxide, 1-10 g) with water. These experiments are directed toward understanding a) the applied triggering pressures needed to induce vapor explosions, b) the conversion of heat to work under a variety of initial conditions, and c) the characteristics of the fuel debris from such events.
- (ii) A large-scale, closed-geometry, fully instrumented test series using induction- and thermite-generated melts (Iron-oxide, Iron-alumina, Corium-A + R, 2-25 kg) dropped into water. These experiments investigate, at large scale and with prototypic melts, the thermal-to-mechanical energy conversion ratio and the propagation of the explosion as functions of fuel and coolant temperatures, mass ratios and compositions. These tests may also address the slower steam production which results when molten fuel is submerged in the water without the occurrence of a steam explosion.
- (iii) Modelling and analysis of steam explosions. This theoretical work will interpret the observed experimental results in light of past theories and models of steam explosions (vapor explosions) and will develop and test new theories and models, where necessary. The ultimate objective is to be able to relate the experimental results to the possible behavior of steam explosions during meltdown accidents. The analysis also addresses the effects of the meltdown sequence on the explosion.
- (iv) Structural consequences of the steam explosion. This work is directed toward (1) evaluating how a steam explosion might lead to containment failure via missile generation or other mechanisms, (2) identifying the realistic mechanisms that could dissipate the explosion energy and reduce the probability of containment failure, and (3) understanding how the explosion might affect the overall accident progression.

### 2.1 Summary

A brief summary of the research accomplishments during the fourth quarter of fiscal 1980 is presented in the following sections.

### 2.1.1 Small Scale Experiments

This quarter progress was made in three areas. A chamber was built for performing single-drop steam explosion experiments under controlled conditions of ambient pressure and composition. It was successfully used this quarter for experiments involving iron-oxide ( $1.1 < O/Fe < 1.3$ ) in argon at atmospheric pressures (0.083 MPa). A new window is being designed to ensure that experiments can be performed at high ambient pressures (1 MPa); a previous design proved to be inadequate under testing.

Debris from a previous test series was examined by an automatic optical scanning technique. Mass average diameters range from 50-200  $\mu\text{m}$ . Smaller particle diameters seem to be associated with stronger trigger pulses and more efficient explosions.

Several scoping experiments were performed to assess the effect of melt viscosity on steam explosions; this is relevant to accident scenarios where core-concrete interactions have occurred and silicates would increase melt viscosity. Single droplets of mullite (38 w/o  $\text{SiO}_2$ -62 w/o  $\text{Al}_2\text{O}_3$ ) did not explode under conditions identical to those which produced efficient explosions with iron-oxide. Based on these initial experiments and a survey of available literature, it appears that melts with viscosities greater than 50 cP may not produce violent explosions.

### 2.1.2 Fully Instrumented Test Series

The FITS experimental program accomplished four tasks this quarter:

- (i) three in-chamber experiments were conducted, FITS-3A, 4A and 5A (the final two at ambient pressure = 1.0 MPa)
- (ii) one EXO-FITS experiment, MD-19, was performed
- (iii) fuel debris size data were obtained for the three in-chamber tests
- (iv) pressure data were also obtained for these tests

The FITS 3A test resulted in a violent spontaneous explosion after the melt was fully submerged in the water. The debris and pressure data were similar to FITS 2A, although this recent explosion may have been more efficient; work estimates have not been completed. FITS 4A and 5A were conducted with initial conditions similar to previous tests except that the ambient pressure was 1 MPa. In test FITS 4A, the delivery system malfunctioned and no explosion resulted. This malfunction was repaired and EXO-FITS test MD-19 was successfully conducted to check the delivery system. In test FITS 5A, an SEL-detonator trigger was installed so that if a spontaneous explosion did not occur, the detonator would be fired 0.45 sec after melt entry into the water. In FITS 5A at 1.01 MPa, the spontaneous explosion was suppressed until the detonator was fired, and a violent explosion was then triggered. Qualitatively, it appeared to be as efficient as FITS 3A.

### 2.1.3 Modelling and Analysis of Steam Explosions

This quarter, a topical report was written that describes the recent modelling and analysis of steam explosion experiments.

### 2.1.4 Containment Failure Analysis

This quarter, a topical report was written that describes recent analysis concerning the consequences of a steam explosion during a postulated meltdown accident.

## 2.2 Small Scale Experiments

### 2.2.1 Controlled Atmosphere Chamber

The chamber for laser-melted single-drop experimentation under controlled conditions of composition and pressure has been built and installed. A sketch of the basic tank was shown in Figure 2.9 of the previous quarterly report [1].

The tank was pressure tested with blind flanges over each aperture. The tank satisfactorily held a gas pressure of 1.8 MPa (current maximum working pressure will be 1.0 MPa). However, when the various aperture closures and windows were installed and testing was repeated, a rocksalt laser window failed at  $\approx$  0.3 MPa. This window will be replaced by a zinc selenide window in a modified mounting.

The chamber has been set up for atmospheric pressure experiments while the laser window modifications are being made. This has involved modifying the original single-drop setup by the construction of a new mounting bench with jacks for positioning the tank, rebuilding the laser shielding and rearranging the CO<sub>2</sub> laser and photographic optics. A photograph of the new chamber is shown in Figure 2.1.

### 2.2.2 Iron-Oxide Drop Experiments Performed in Argon

The difficulty in initiating explosions in iron-oxide of low O/Fe in the arc melting experiments is being explored by melting single drops of iron-oxide in gaseous argon at local atmospheric pressure, using the controlled atmosphere chamber. As yet, no O/Fe ratio lower than 1.1 has been achieved; this composition explodes normally.

### 2.2.3 Debris Particle Sizes

Some debris size information for the explosions of single-drops of molten iron-oxide was presented in the previous quarterly report (Figures 2-7 (experiment 11-72-2) and 2-8 (experiment 11-75-1) in Reference 1). These data were produced by a manual technique as described in that report. During this quarter, a new automatic optical scanning procedure (Quantimet) became available for producing debris size data.

In order to test the manual technique against that of the Quantimet (to be used in all future debris analyses), we ran a completely new single-drop experiment, 11-79-3, designed to reproduce 11-75-1 as closely as possible. In this experiment, a 142 mm diameter Nuclepore 0.2  $\mu$ m pore size polycarbonate filter membrane was used to separate debris from water. This membrane material shows essentially no interfering background in the Quantimet. An automatic analysis of the particles produced in this experiment was performed, and converted into mass fractions as with the manual analyses in experiment 11-75-1.

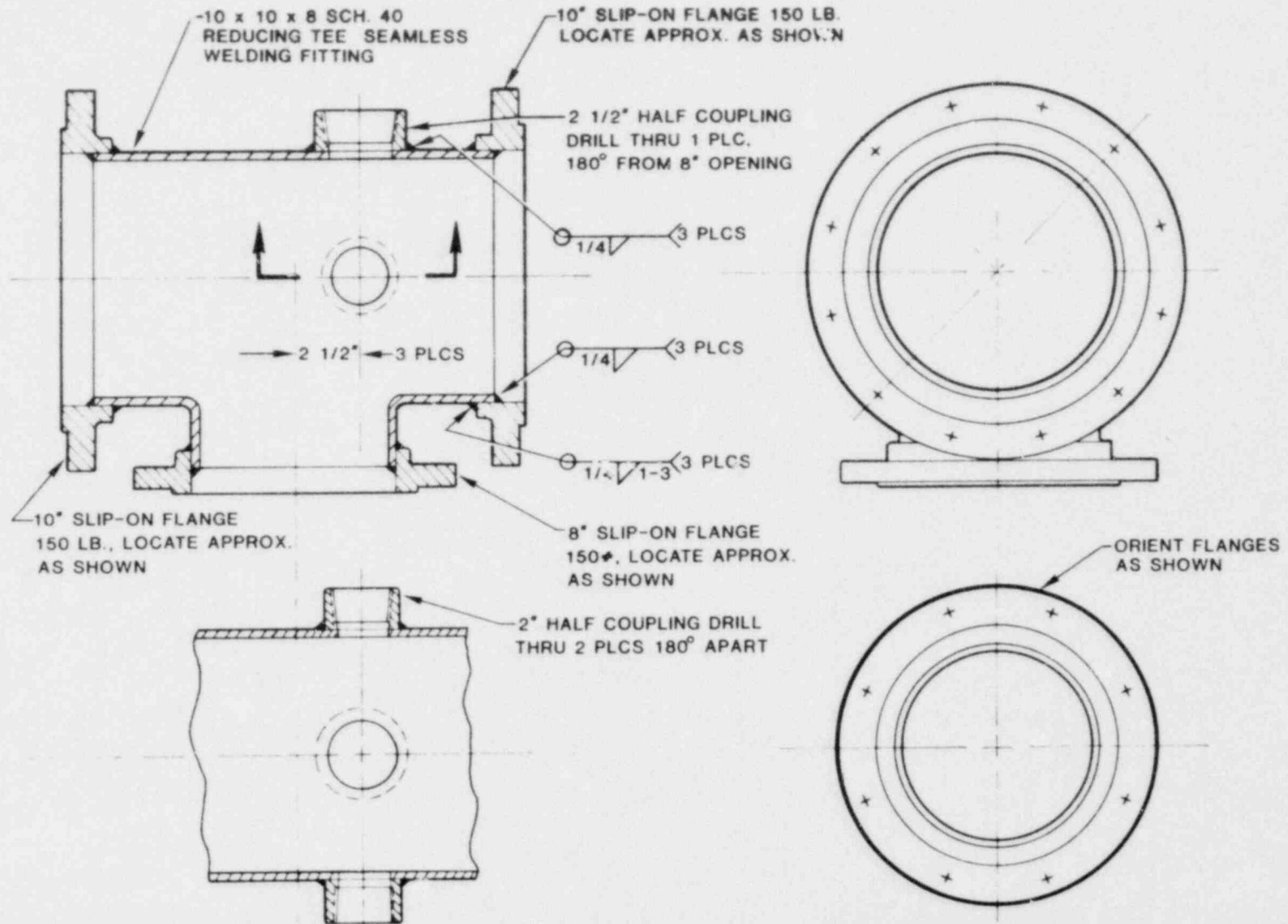


Figure 2.1 Experimental Apparatus for High Ambient Pressures.

The result is shown in Figure 2.2. The consistency between Figures 2.3 and 2.8 in Reference 1 lends credence to the manual size analysis of the particles, even though this was performed in two separate segments.

Quantimet particle size analyses were performed on the debris produced in a series of single-drop iron-oxide explosions in which the peak applied trigger pressure was varied about 10-fold over the range 0.3 to 3.0 MPa. These are part of the second test series described in Section 2.2.3 in the previous quarterly report, [1]. The particle size distributions were similar to that shown in Figure 2.2, except that the curves were shifted somewhat to the left or right, depending on applied peak pressure. A plot of the mass median diameters (50% intercept) of these debris particles is shown in Figure 2.3, plotted as a function of the peak applied trigger pressure. The peak pressures generated were larger in these experiments as the mass median particle diameters decreased; this is shown in Figure 2.4.

The particle size data shown in Figure 2.2 and in Figure 2.8 of Reference 1, were supplied to the participants of the CSNI-sponsored joint interpretive study of steam explosion data.

#### 2.2.4 Effect of Melt Viscosity on Steam Explosions

To produce a violent steam explosion, the hot liquid rapidly breaks up into small sizes to generate the large surface area necessary for rapid heat transfer and formation of steam. One possible explanation for this breakup is that a fluid instability forms when the boiling film layer collapses causing contact between hot and cold liquids [2]. Since instabilities of this sort are strongly affected by the ratio of the viscosities of the two liquids [3, 4], it would seem that steam explosions might depend on the viscosity of the hot liquid at the time of interaction. Several scoping, single-drop experiments were performed to test this hypothesis.

A composition in the ( $\text{Al}_2\text{O}_3/\text{SiO}_2$ ) system was chosen as the hot liquid for the following reasons: (a) there is a broad data base for viscosity and other properties of this binary oxide system at high temperatures, (b) no special atmosphere is required for the melting because of the single-valence behavior of both metallic cations (c) several compositions in the system are available commercially, and (d) the viscosity of several molten compositions in the system can increase as much as ten-fold above that of the original pure component molten  $\text{Al}_2\text{O}_3$  [5]. The composition, (38 w/o  $\text{SiO}_2/\text{Al}_2\text{O}_3$ ) was studied here (mullite, McDanel Refractories, Inc., Type MV 30). This material has viscosities that span the range 64 to 210 cP as the temperature changes from 2650 to 2173 K.

To perform an experiment, a chip ( $\approx 30$  mg) of the mullite was suspended on an iridium wire and melted in air by heating with the  $\text{CO}_2$  laser at  $\approx 235$  W. The drop was shaken from the wire and allowed to fall 20 mm through air before submerging in outgassed water at  $24^\circ\text{C}$ . Release temperatures were  $\approx 2650$  K, with the melt viscosity being  $\approx 64$  cP [5].

About 40 m sec after the drop entered the water, a bridgewire pressure transient of about 2 MPa was applied to the drop/water interaction zone. The high speed films showed much undulation of the melt as the boiling film was disturbed but neither fine fragmentation nor an explosion developed. (An iron-oxide drop which underwent a similar undulation would have exploded). In addition to the parent spherule, the debris included some clumps of tiny glassy spherules 0.1 to 0.8 mm

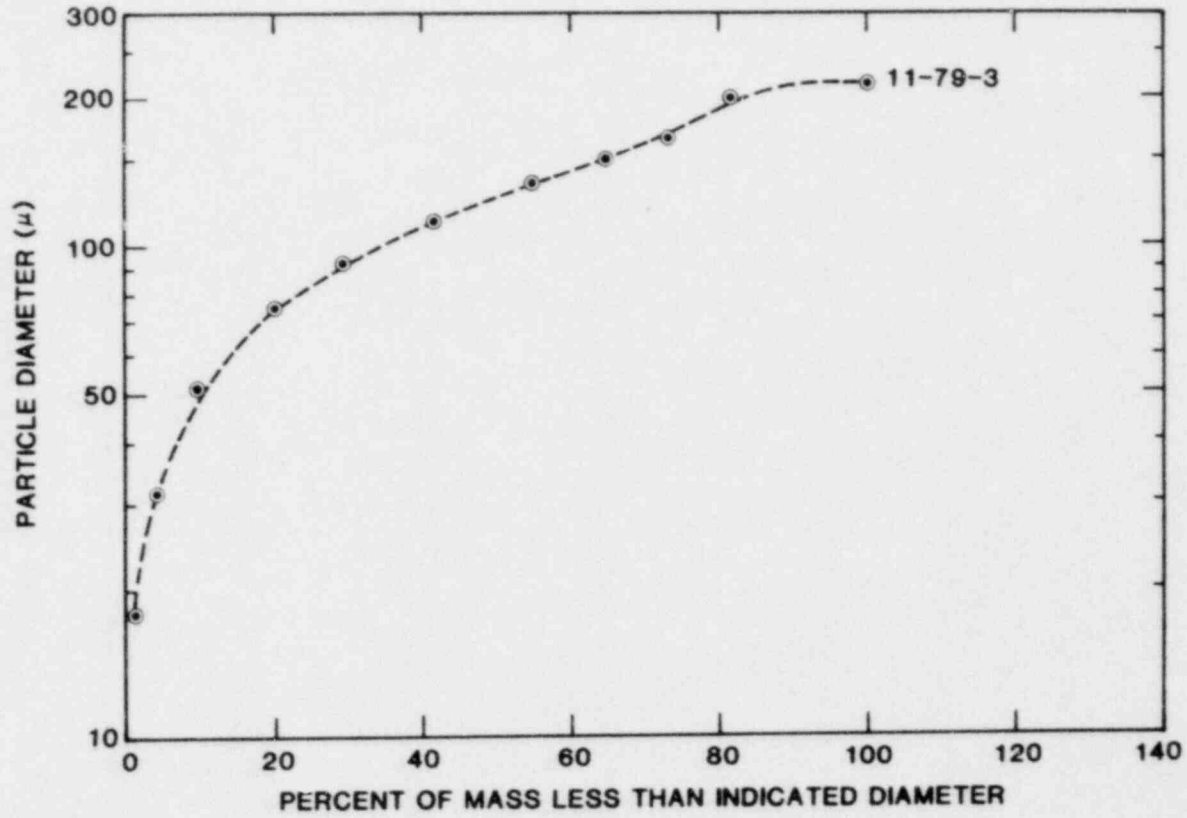


Figure 2.2 Cumulative Mass Average Debris Distribution for Test N-79-3 .

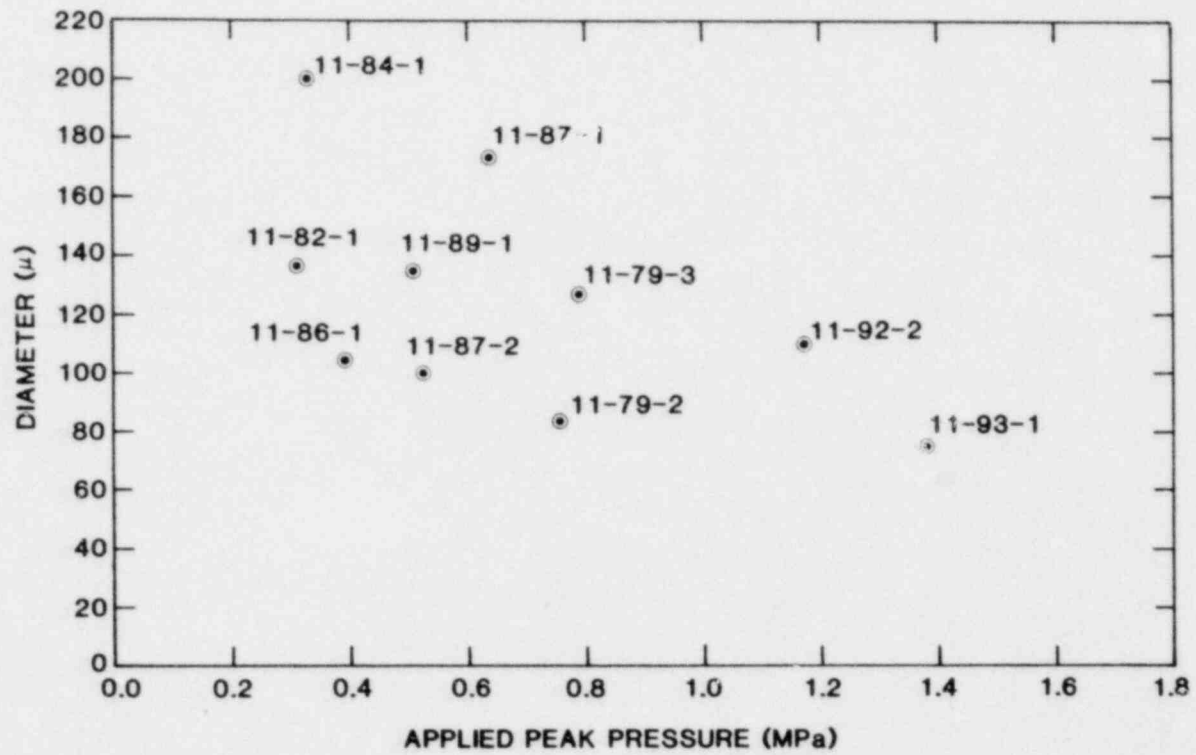


Figure 2.3 Debris Mass Average Diameter as a function of Applied Peak Pressure.

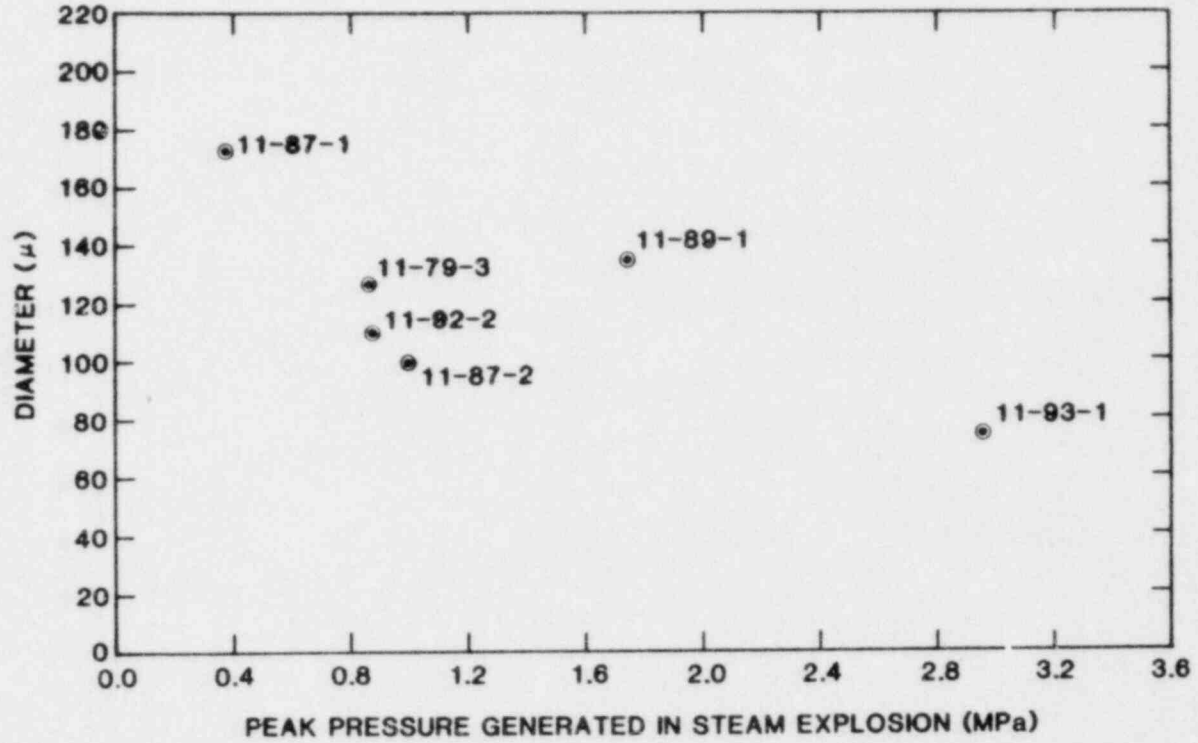


Figure 2.4 Debris Mass Average Diameter as a function of Explosion Peak Pressure.



across, intermixed with glassy fibers about 0.01 mm thick; some of the spherules had glassy fiber-like tails. One such agglomeration is shown in the scanning electron micrograph in Figure 2.5.

A preliminary interpretation of these experiments is that the unstable film collapse mode was initiated by the pressure transient, but that the melt was too viscous to break up thoroughly; instead, it preferred to spin glassy fibers as a few spherules were torn from the parent drop's surface during the contact.

The effect of melt viscosity on steam explosions was explored further by tabulating the viscosities of melts known to have participated in steam explosions. The results of this tabulation are shown in Tables 2.1 (Sandia data) and 2.2 (literature search).

The conclusion which is emerging from the experiments performed both at Sandia and elsewhere is that steam explosions have occurred with a wide range of melt compositions and contact conditions, but always with melts which are relatively fluid. From Tables 2.1 and 2.2, it seems that the most viscous of the melts to have exploded is aluminum oxide, with a viscosity of 27 cP, while the molten mullite with a viscosity of 64 cP could not be induced to explode. It seems, then, that a viscosity value of perhaps 50 cP might separate those melts which participate in steam explosions from those which may not.

It should be emphasized, however, that the viscosity correlations discussed here are at present based on only a few scoping experiments and a literature search which could be incomplete. However, if the correlations are valid, they suggest a reduction in the likelihood of a steam explosion in a fuel melt situation where the melt viscosity is high. Such situations might arise after core-concrete interactions [6, 7], or in melts which had begun to solidify.

Clearly, there is need for more study of the effects of melt viscosity on steam explosions.

### 2.3 Fully Instrumented Test Series

During this quarter, three in-chamber experiments and one EXO-FITS experiment were done.

Results from the first 2 FITS experiments were used to design FITS 3A. The observations made earlier [1]--that spontaneous triggering depends on melt entry velocity and shape for the melt masses near the threshold melt mass--required that additional work be done on the delivery system in FITS to insure that proper melt entry velocities could be achieved. FITS 3A used a 5.5 Kg melt mass and resulted in a typical propagating reaction. The propagation velocity was 206 m/s. The reaction was spontaneously triggered at 0.1 sec. Data consisted of water phase pressures, chamber pressures, and chamber temperatures. The average particle size of debris was found to be 155  $\mu$ m.

FITS 4A was designed to be a high ambient pressure version of FITS 3A. The FITS chamber pressurization system was installed and checked prior to this experiment. FITS 4A was the first experiment conducted at high ambient pressure and used a 5.5 kg melt mass. Chamber pressure was 0.946 MPa at the time the melt entered the water. The experiment did not result in an explosion, but the reason for this is not clear. Problems with the delivery cylinder (pressure seal failure), caused a late and dispersed melt release. Melt velocity was approximately 7 m/s at the time of water entry and data from melt sensing

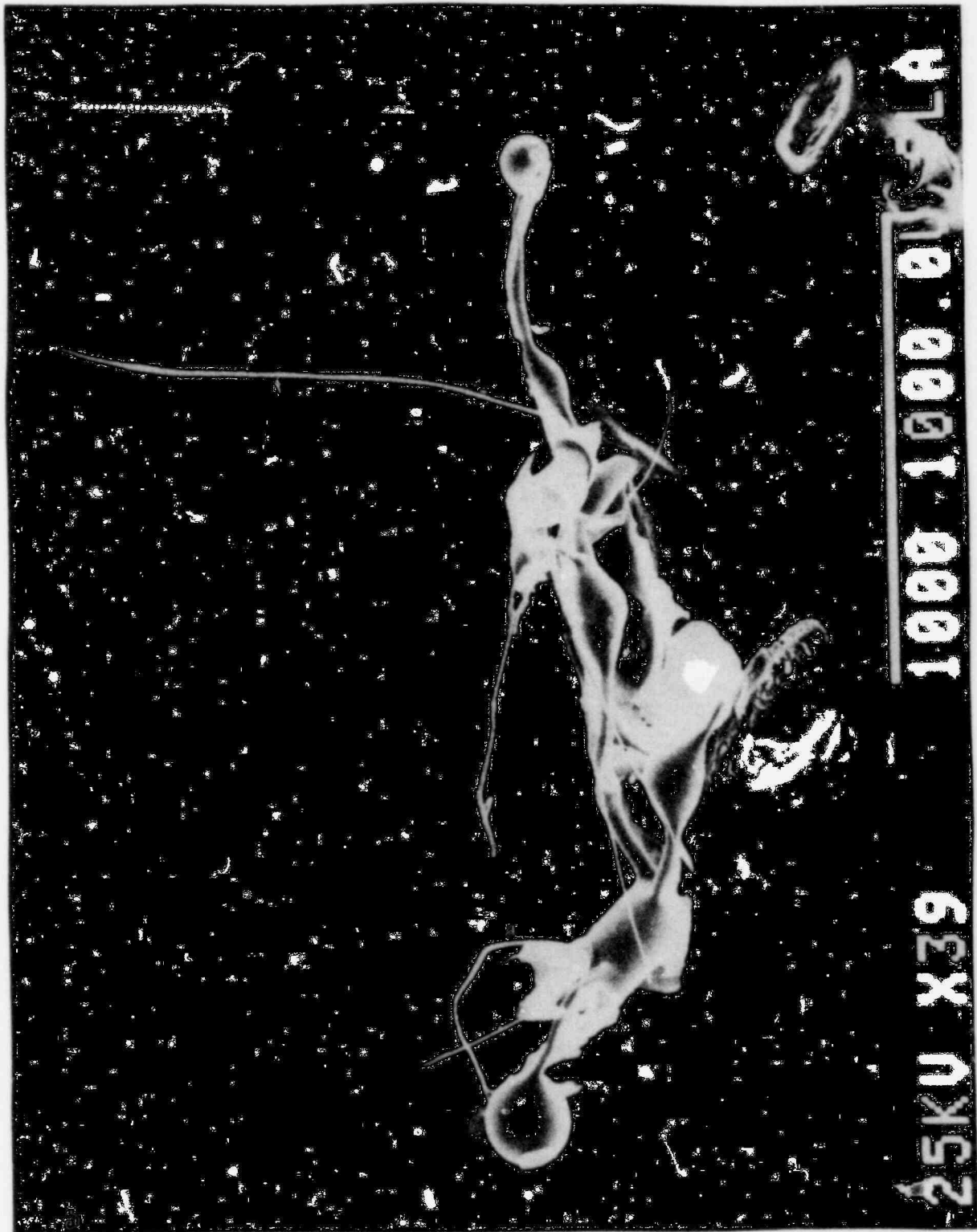


Figure 2.5 Alumina-Silica Debris from a Droplet Experiment with no Explosion.

TABLE 2.1

Viscosities of Melts which Participated in Steam Explosions  
In Sandia's Laboratory Scale Experiments

Melt	Heating Technique	Melt Temperature (°K)	Explosive Tendency	Estimated Liquid Viscosity at Interaction Time (cP)	Source of Viscosity Data	Remarks
Aluminum-Oxide	CO <sub>2</sub> Laser	2300	Moderate	27	Ref. 8	
Cobalt-Oxide	Arc Melter	2000	Vigorous	Not Known*	---	
Corium-A Simulants Oxidic	Arc Melter	2000-2200	Weak	3-6	Ref. 9	Four Spontaneous Fragmentations in 35 Tries
Corium-E Simulants	Arc Melter	2000-2200	Vigorous	2-6	Ref. 9	
Iron-Oxide	Arc Melter CO <sub>2</sub> Laser	2000 2300	Vigorous Vigorous	12 6	Ref. 10	
Uranium-Oxide	Levitation Melting + Drop Combustion	~ 3500	Seemed Vigorous; Poorly Controlled Experiment	~ 6	Ref. 11	One Fragmentation in 4 Tries
Zircorium-Oxide	CO <sub>2</sub> Laser Ignition + Drop Combustion	~ 3500	Moderate	Not Known*	---	

\*i.e., could not be located in Chemical Abstracts

TABLE 2.2

Viscosities of Melts Reported to Have Exploded  
in Steam Explosion Interactions

<u>Melt</u>	<u>Source of Explosion Information</u>	<u>Estimated Viscosity At Interaction Time (cP)</u>	<u>Source of Viscosity Data</u>
Metals, including Al, Ag, Au, Bi, Co, Cu, Fe, In, K, Li, Mg, Na, Ni, Pb, Sn, V, Zr	Ref. 18	< 10	Ref. 12
Molten Salts Including NaCl, AgCl, KCl	Ref. 18	< 10	Ref. 13
(60 w/o B <sub>2</sub> O <sub>3</sub> / PbO)*	Ref. 19	< 20	Ref. 14, 15
Open-Hearth Ironmaking Slag (low SiO <sub>2</sub> )	Ref. 20*	= 7 (calculated)	Ref. 16
Coppermaking Slag (CuS)	Ref. 21*	3.7	Ref. 17

\*Arakeri, et al., call their work a "study of the molten glass/water thermal interaction." The use of the words "molten glass" may be misleading, however, because this B<sub>2</sub>O<sub>3</sub>/PbO composition has a melt viscosity very uncharacteristic of molten glasses as normally thought of. (The authors state that "at a temperature of 1173K, the molten glass was almost as fluid as water at room temperature" (= cP).

instrumentation indicated a very dispersed melt column. No data other than diagnostics were obtained. Debris particle size was similar to other non-exploding mixtures observed in EXO-FITS experiments. The average particle size was greater than 3 mm.

Problems with the delivery system in this and other in-chamber experiments necessitated a redesign and modification of the system to better control the delivery parameters. That work was done and an EXO-FITS experiment (MD-19) was used to check the delivery system. The modified delivery system is identical to the previous system except the point of melt release is in a different location in the chamber and the delivery cylinder travel distance has been reduced. The modified delivery system was used for the third experiment in this quarter (FITS 5A). This experiment was nearly identical to FITS 4A and was successful. A 5.5 kg melt was delivered at 5.4 m/s. The initial chamber pressure was 1.01 MPa. In addition to studying the effect of ambient pressure on explosivity, an SEI-detonator located in the water chamber was made available to supply an external trigger, if needed. The trigger firing time was set so that if an explosion was not spontaneously triggered by the expected time after melt entry, the detonator would be fired to trigger the interaction. No spontaneous explosion was observed as late as 0.44 sec after melt entry. At 0.44 sec, the detonator was fired and an explosion was observed. Water phase pressures with peaks on the order of 100 bar were recorded. These peaks are similar to those seen in ambient experiments. The chamber did not vent after the interaction, and a chamber static pressure increase of 0.4 bar above ambient was recorded. These pressures persisted for times much longer than 10 sec; not all the data has been reduced. Debris recovered from the experiment is similar to FITS 3A; The debris is mostly spherical. Data reduction and analysis is in process and will be reported in the near future.

### 2.3.1 FITS Experiments

The FITS 3A experiment was conducted on June 26, 1980. Table 2.3 describes the initial conditions for this experiment.

TABLE 2.3

#### FITS 3A Initial Conditions

Melt: 5.5 kg Fe-Al<sub>2</sub>O<sub>3</sub>  
Coolant: 228 kg; 23°C; 0.62 m depth  
Chamber: 0.61 m x 0.61 m x 0.76 m  
Pressure: 0.083 MPa  
Melt Entry Velocity: 5.0 m/s

The experiment resulted in a propagating explosion similar to those observed in the EXO-FITS experiments. Water chamber fragments generated during the explosion penetrated the burst diaphragm causing premature venting. Data from water phase pressure transducers, chamber pressure and temperature sensors were obtained and are shown in Figures 2.6 and 2.7. Figure 2.6 is typical of water phase pressures. Peaks on the order of 100 bars are observed with durations on the order of 2 ms.

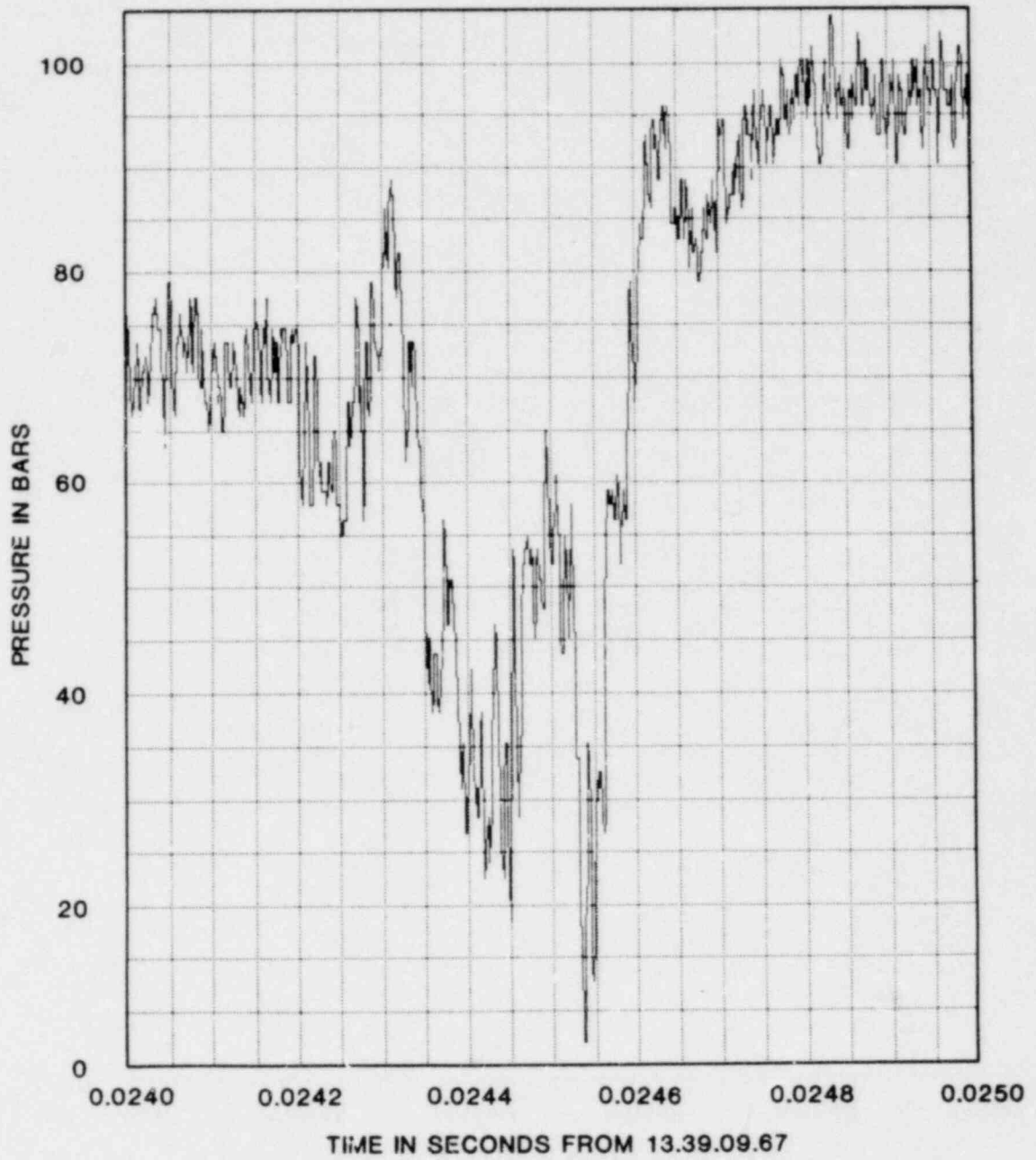


Figure 2.6 Water Phase Pressure History near the wall for FITS Test -3A.

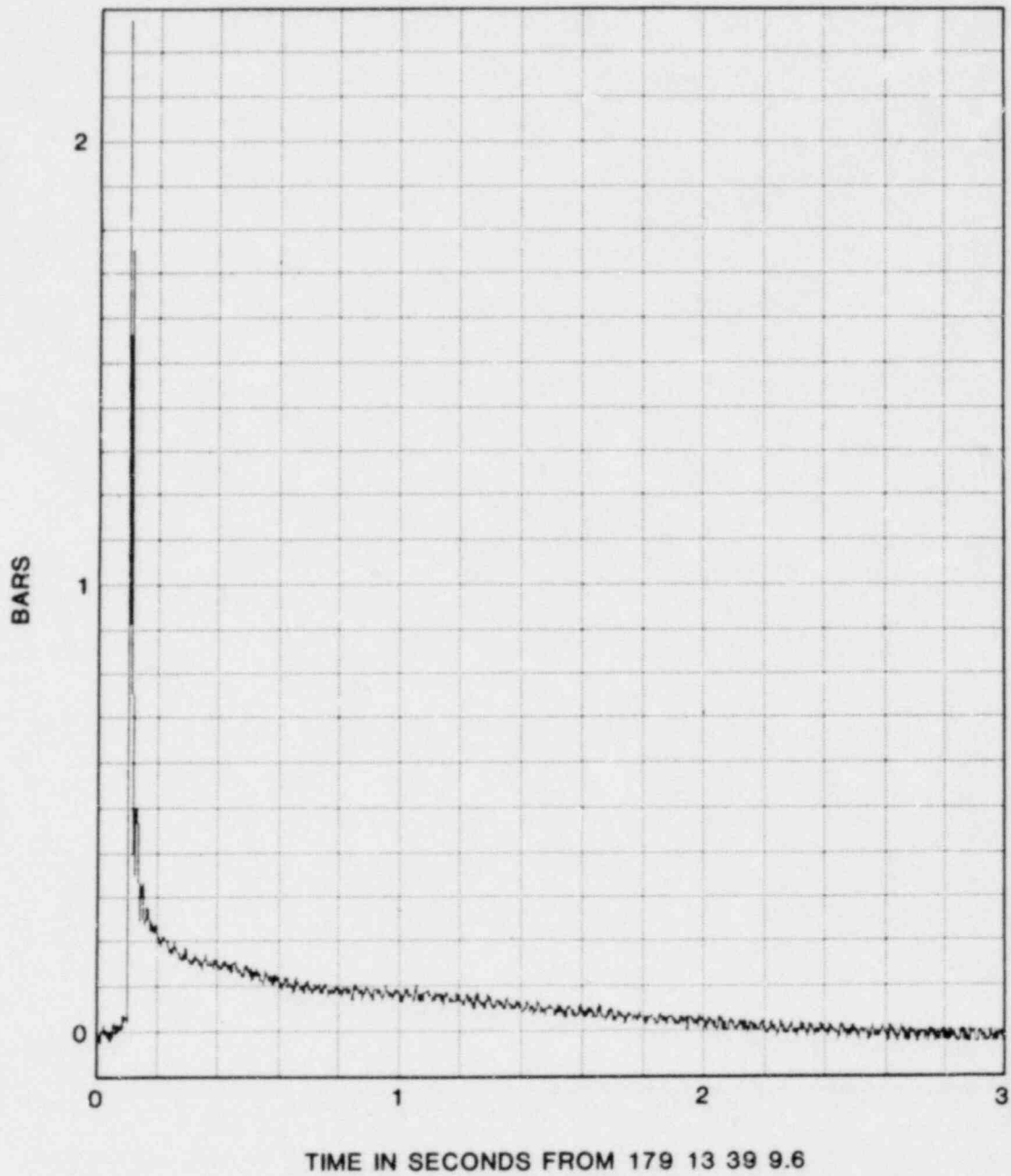


Figure 2.7 Chamber Air Pressure History for FITS-3A.

These data are typical of water phase pressures observed from other experiments in this work.

Figure 2.7 depicts data from one chamber pressure transducer. The first spike is due to debris/water/steam impact on the chamber transducer. This peak pressure of 3.7 bars decays to 0.22 bars after 50 ms. The 0.22 bar pressure persists for approximately 500 ms, and then decays back to ambient at approximately 2.5 sec due to chamber venting. The chamber ambient temperature increase was 50°C. The rise time of this temperature was 51 ms. The temperature decays to 25°C after approximately 100 ms and remains constant until the recorder was turned off 5 sec after the event.

Debris distribution is shown in Figure 2.8. The average particle size was 155  $\mu\text{m}$  and approximately 15% of the material is less than 38  $\mu\text{m}$  in diameter (the smallest sieve used for the analysis).

A propagation velocity of 206 m/s was observed. The explosion was triggered spontaneously at the base of the melt 0.1 sec after melt entry. Mixture density defined as mass of fuel divided by the total mixing volume was estimated to be 0.36 g/cm<sup>3</sup>.

The FITS 4A experiment was conducted on July 23, 1980. This experiment was intended to study the effect of ambient pressure on explosivity. The chamber pressurization system was installed and checked. The initial conditions are described in Table 2.4 below.

TABLE 2.4

FITS 4A Initial Conditions

Melt: 5.5 kg Fe-Al<sub>2</sub>O<sub>3</sub>  
Coolant: 226 kg; 24°C; 0.6 m depth  
Chamber: 0.61 m x 0.61 m x 0.76 m  
Pressure: 0.946 MPa  
Melt Entry Velocity: 7 m/s Approximately

No explosion resulted from the melt-water reaction. Analysis of the experiment indicated that a seal in the delivery cylinder failed which caused the delivery sequence to be slower than normal. Due to this late delivery, the crucible failed approximately 16 sec after delivery releasing the melt high in the chamber above the stripping mechanism. The melt impacted the stripping mechanism and was dispersed as evidenced by data from the melt velocity sensor. The combination of high entry velocity, the dispersed nature of the melt, more rapid melt cooling, and the high chamber ambient pressure suppressed or prevented a spontaneous explosion. No data, except diagnostic data, was obtained.

The debris particle size is shown in Figure 2.9. This debris is typical of that found in EXO-FITS experiments when no explosion is generated.

FITS 5A was conducted on September 10, 1980. This experiment was done to study the effect of high ambient pressure on explosivity and



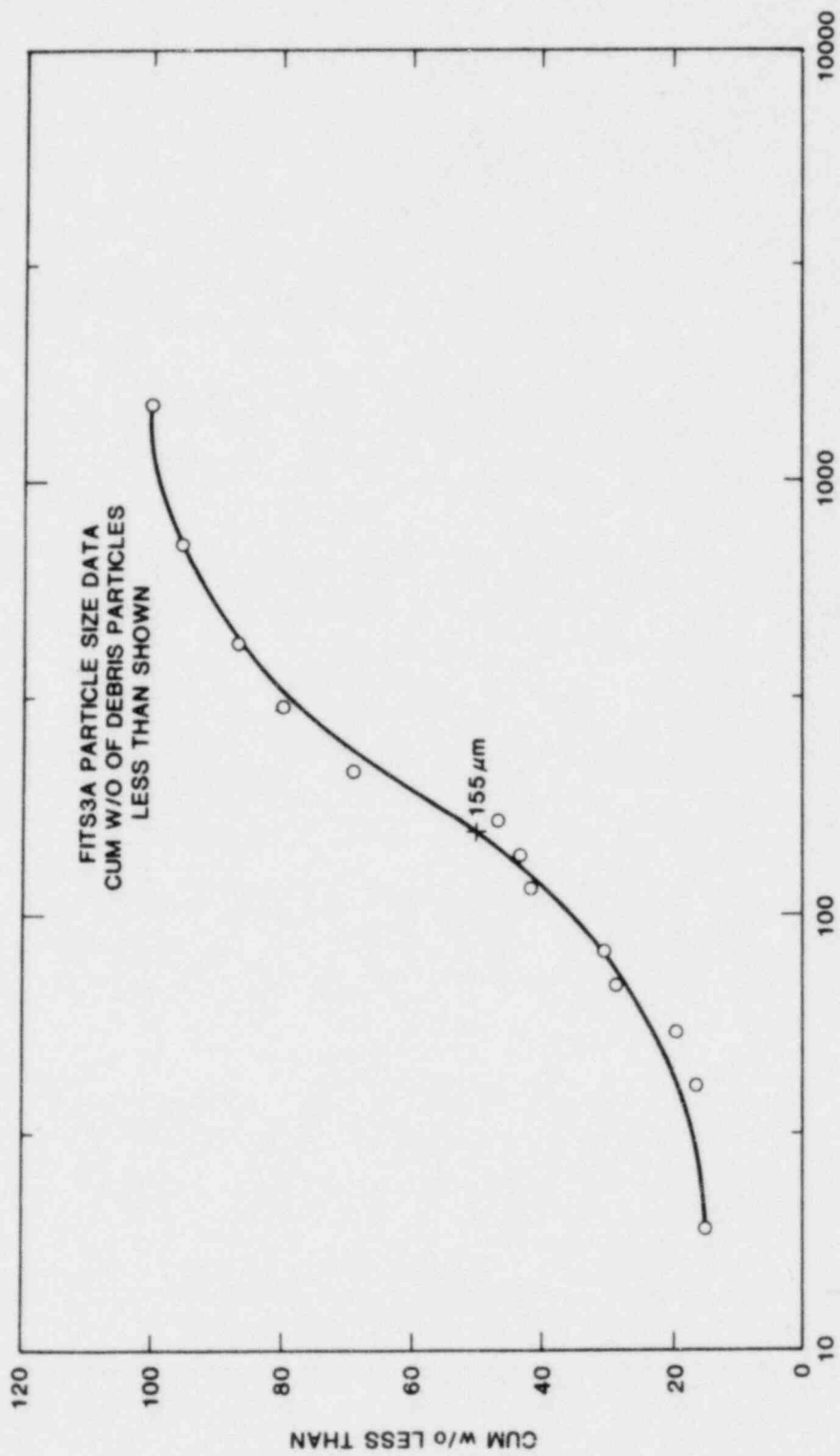


Figure 2.8 AVERAGE SIEVE OPENING  $\mu\text{m}$

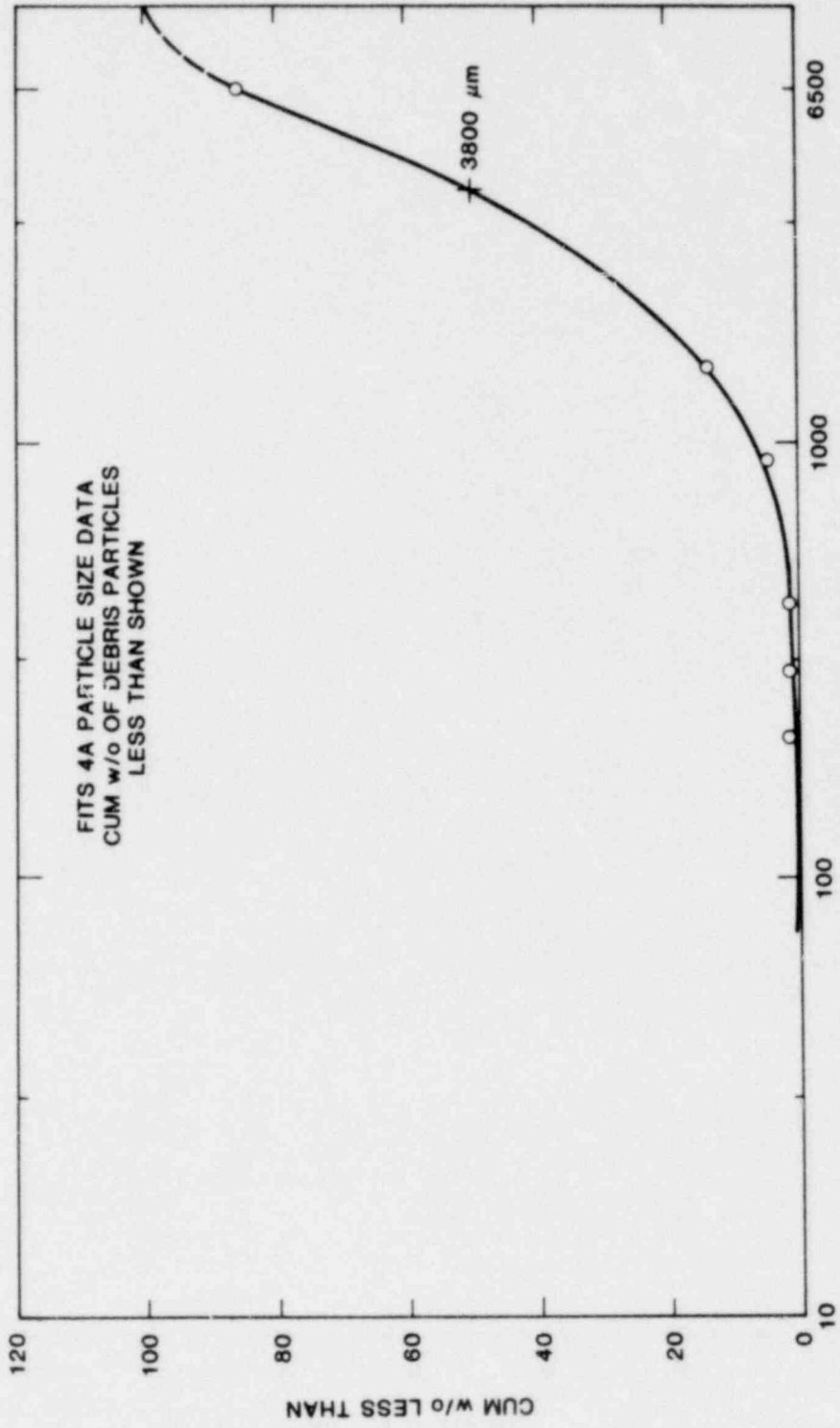


Figure 2.9 AVERAGE SIEVE OPENING μm

to determine if an external trigger source could initiate an explosion. The initial conditions for this experiment are shown in Table 2.5.

TABLE 2.5

FITS 5A Initial Conditions

Melt: 5.5 kg Fe-Al<sub>2</sub>O<sub>3</sub>  
Coolant: 226 kg; 24°C; 0.61 m depth  
Chamber: 0.61 m x 0.61 m x 0.76 m  
Pressure: 1.01 MPa  
Melt Entry Velocity: 5.4 m/s  
External Trigger: SE-1 EBW detonator; 0.635 g  
of PETN explosive

The experimental configuration of the water chamber is shown in Figure 2.10. The detonator was located 12.7 mm below the base of the water chamber and is also shown in Figure 2.10. The time for the detonator firing was determined from earlier experiments where it was found that time to explosion was between 0.1 and 0.2 sec after melt entry. No spontaneous explosion was observed up to 0.44 sec after melt entry. The melt settled to the bottom of the chamber and began to cool. Trigger time was set at 0.44 sec after melt entry to allow sufficient time for a spontaneous trigger to develop. Although no spontaneous explosion occurred, an explosion was nevertheless triggered by the external source. This interaction did not appear to exhibit a clear propagation phase as in other experiments because most of the melt had settled on the bottom, but it appeared to be as energetic based on debris and residue remaining after the event. Data, which are still being reduced, showed that water phase pressures on the order of 100 bars were generated by the triggered reaction. Debris particle size shown in Figure 2.11 is nearly identical to that for FITS 3A, an ambient spontaneously triggered explosion.

This fact implies that, at high pressures if an energetic trigger source can be generated, the potential for a steam explosion exists. The trigger amplitude and impulse have yet to be determined for this experiment. Auxilliary experiments and calculations are planned to be done to determine this level. This information will be reported in a subsequent report.

### 2.3.2 Conclusions

FITS 5A represents the last experiment in this series. The A Series was done primarily to study and check the experimental and measurement techniques needed for future, more refined explosion yield experiments.

The objectives of the program, to study conversion ratio and scaling effects have not yet been accomplished. However, a better understanding of what measurements need to be made and what instrumentation is required (i.e., transducers and water chamber design) have been gained.

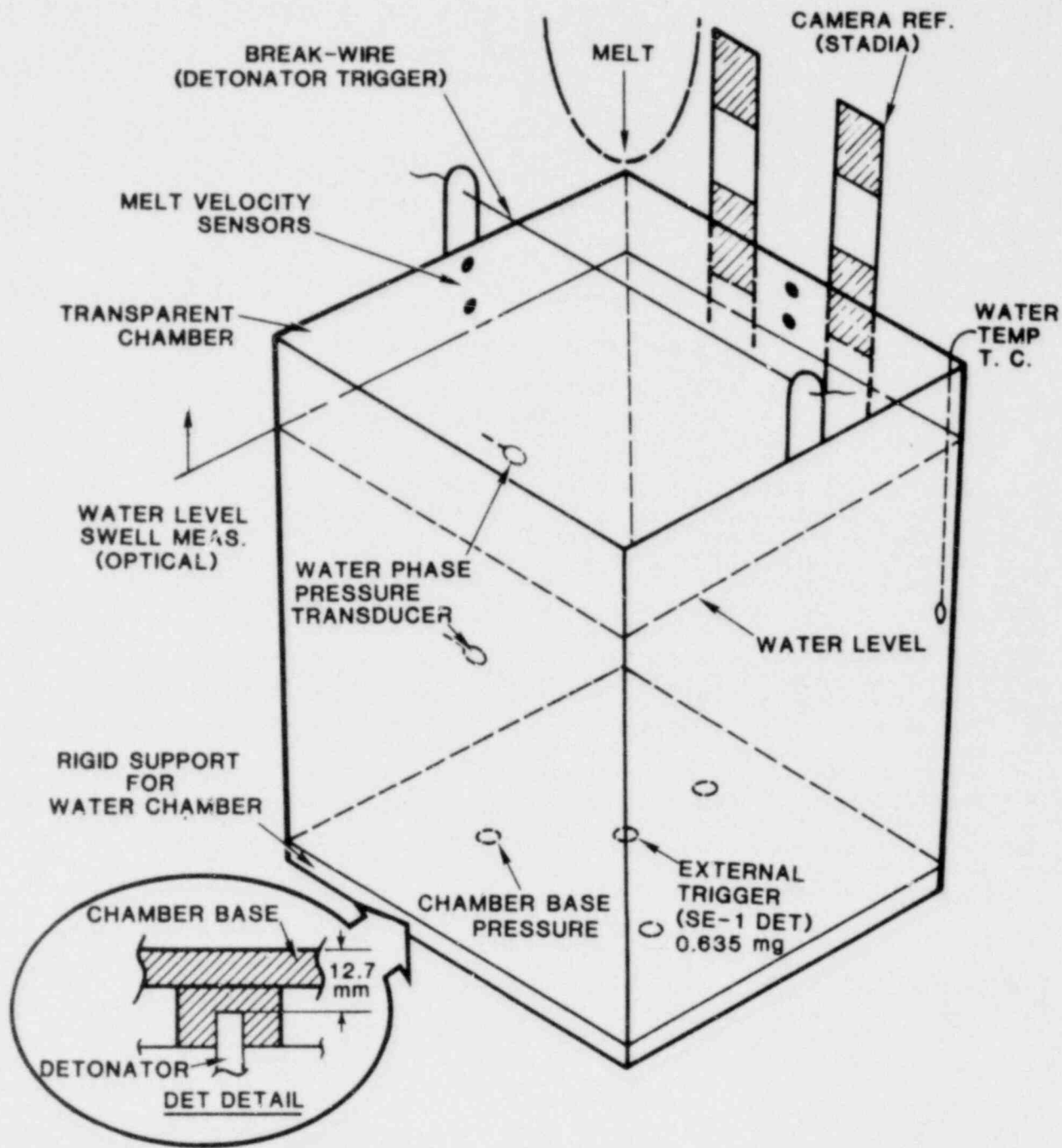


Figure 2.10 Experimental Water Chamber (with detonator) used for FITS-5A.

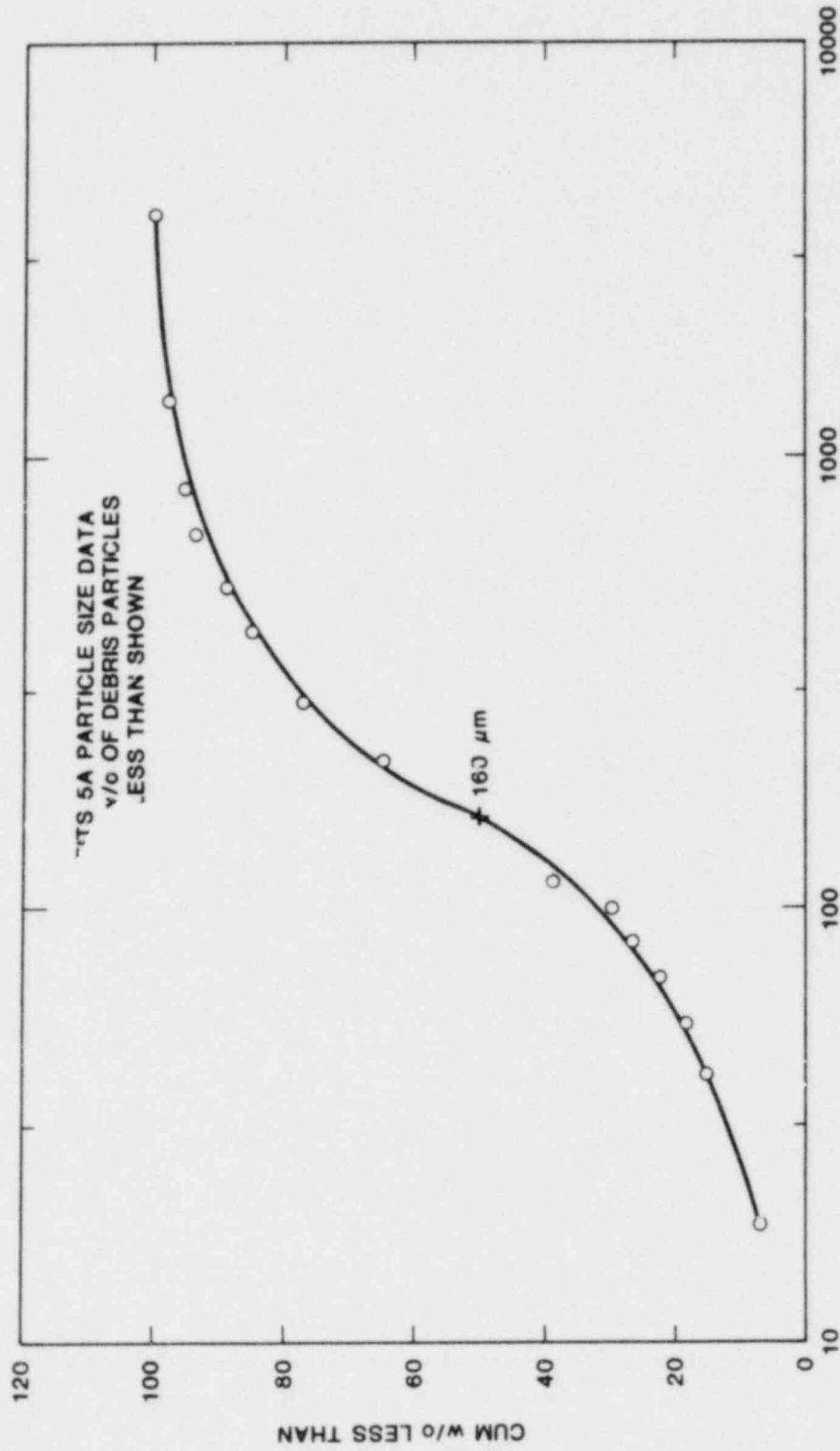


Figure 2.11 AVERAGE SIEVE OPENING μm

A topical report describing both the facility design and the five experiments as well as the EXO-FITS experiments is in process.

#### 2.4 Modelling and Analysis of Steam Explosions

This quarter, a topical report was written that describes the recent modelling and analysis of steam explosion experiments.

#### 2.5 Containment Failure Analysis

This quarter, a topical report was written that describes recent analysis concerning the consequences of a steam explosion during a postulated meltdown accident.

#### 2.6 References

1. LWR Safety Research Program, Quarterly Report, SAND80-1304 No. 2, NUREG/CR-1509/2 of 4, Sandia National Laboratories (August, 1980)
2. Corradini, M. L., 1980, Phenomenological Modelling of the Small-Scale Vapor Explosion Experiments, Sandia National Laboratories, Albuquerque, N.M., SAND79-2003.
3. Taylor, G. I., 1934, "The Formation of Emulsions in Definable Fields of Flow", Proc. Roy. Soc. (London) A146, 501-523.
4. Hinze, J. O., 1955, "Fundamentals of the Hydrodynamic Mechanism of Splitting in Dispersion Processes", A.I.Ch.E.J., 1, 289-295.
5. Elyutin, V. P., Kostikov, V. I., Mitin, B. S., and Nagibin, Yu A., 1969, "Viscosity of Alumina", Russian J. Phys. Chem. 43, 316-319.
6. Powers, D. A., and Frazier, A. W., 1977, VISHRO: A Computer Subroutine for Estimating the Viscosity and Density of Complex Silicate Melts, Sandia National Laboratories, Albuquerque, N.M., SAND76-0649.
7. Leibowitz, L., Williams, C., and Chasanov, M. G., 1974, "The Viscosity of UO<sub>2</sub> - Basalt Melts", Nucl. Technol. 24, 234-237.
8. Blanquist, R. A., Fink, J. K., and Leibowitz, L., 1978, "Viscosity of Molten Alumina", Ceram. Bull. 57, 522.
9. Nazare, S., Ondracek, G., and Schulz, B., 1977, "Properties of Light Water Reactor Core Melts", Nuclear Technol. 32, 239-246.
10. Schenck, H., Frohberg, M. G., and Rohde, W., 1961, "Viscosity of Pure Liquid Iron Oxide in the Temperature Range Between 1380 and 1490°C", Arch. Eisenhüttenw. 82(8), 521.
11. Tsai, H. C. and Olander, D. R., 1972, "The Viscosity of Molten Uranium Dioxide", J. Nucl. Mater. 44, 83-86.
12. Beyer, R. T., and Ring, E. M., 1972, "The Viscosity of Liquid Metals", Chap. 10 in Liquid Metals, Chemistry and Physics, Ed. Beer, S. Z., Marcel Dekker, New York.

References continued

13. Janz, G. J., Tomkins, R. P. T., Allen, C. B., Downey, J. R. Jr., Gardner, G. L., Krebs, U., and Singer, S. K., 1975, "Molten Salts: Volume 4, Part 2, Chlorides and Mixtures. Electrical Conductance, Density, Viscosity and Surface Tension Data", J. Phys. Chem. Ref. Data 4, 871-1178.
14. Oliver, C. B., 1965, "The Viscosity of Some Molten Lead Compounds", J. Electrochem. Soc. 112, 629-31.
15. Zarzycki, J., and Naudin, F., 1967, "A Study of the Kinetics of the Metastable Phase Separation in the PbO-B<sub>2</sub>O<sub>3</sub> System by Small Angle Scattering of X-Rays", Phys. Chem. of Glasses 8, 11-18.
16. Capps, W., 1977, "Some Properties of Coal Slags of Importance to MHD", 16th Symp. Engineering Aspects of MHD, Pittsburgh, PA; see also ANL77-21, pp. 190-195.
17. Dobrovinskii, I. E., Esin, O. A., Barmin, L. N., 1971, "Density and Viscosity of Iron, Nickel, Cobalt and Copper Sulfides", Sb. Tr. Vses. Meshvus. Nauch. Konf. Teor. Protsess. Tsvet. Met., 99-103; Chem. Abstr. 77, 79641f (1972).
18. Buxton, L. D., Nelson, L. S., Core Meltdown Experimental Review, SAND74-0382, Sandia National Laboratories, Albuquerque, N.M. (August 1975).
19. Arakeri, V. H., Catton, I., and Kastenbergl, W. E., 1978, "An Experimental Study of the Molten Glass/Water Thermal Interaction Under Free and Forced Conditions", Nucl. Sci. Eng. 66, 153-166.
20. Tetzner, H., 1959, "Slag Explosions in Open-Hearth Steelworks", Neue Hutte 4, 352-9.
21. Azuma, K., Goto, S., and Kametani, H., 1957, "The Explosions of Matte by Water. I. Nature of the Explosion", Nippon Kogyo Kaishi 73, 295-300.

### 3. Separate Effects Tests for TRAP Code Development

(J. C. Cummings, R. M. Elrick, R. A. Sallach)

The objective of this program is to provide experimental data to aid in the development of the TRAP<sup>(1)</sup> code. The program is concerned in particular with laboratory-scale experiments to investigate:

- vapor pressures of fission-product species at elevated temperatures, and
- chemical compound formation and reaction rates for multiple fission-product species in high-temperature steam environments.

Transpiration and microbalance techniques are employed to measure vapor pressures, to study vapor-vapor and vapor-wall reactions, and to measure surface absorption and desorption rates of the fission-product species. Multiple fission-product species will be studied in the high-temperature steam environment of the Fission Product Reaction Facility (FPRF). Laser Raman spectroscopy will be used as a species diagnostic for the FPRF tests and the Raman system is being calibrated using an interim cell to provide the fission-product environment.

#### 3.1 Chemical Experiments

The chemical data required by the TRAP code can be categorized as either vapor pressure (equilibrium) data or as kinetic (dynamic) data. Vapor pressure data include the identification of individual vapor species containing one or more fission-product elements and the determination of the concentration of the vapor species as a function of equilibrium temperature. Kinetic data describe the rate of approach to an equilibrium condition, and such data allow us to predict the extent or progress of chemical reactions and physical processes.

We are using a transpiration technique to determine fission-product vapor pressures. In transpiration experiments, a measured quantity of carrier gas is passed over a heated, condensed phase containing the fission-product species of interest. This passage is at a rate sufficiently slow that a local equilibrium concentration (partial pressure) is established in the gas stream. The vaporized species is collected as a condensate and its mass determined. Knowing the condensate mass and the quantity of carrier gas, we can calculate the vapor pressure. The composition of the carrier gas can be varied in order to investigate chemical interactions (apparent increases in the vapor pressure) with the fission-product species.

In order to check on the precision and accuracy of the transpiration technique, we chose the compound CsI as our first fission-product species, since its vapor pressure had been previously determined<sup>(2)</sup>. By interpolation of the existing data, it can be calculated that CsI has a vapor pressure of 266 Pa (2.0 torr) at 1043 K (779°C). The average value from our measurements was 240 Pa (1.8 torr) with a root-mean-square deviation of  $\pm 30$  Pa (0.2 torr). We also determined that CsI vapor does not interact significantly (at 1040 K) with either H<sub>2</sub> or H<sub>2</sub>O.

We conducted transpiration experiments using CsOH over the temperature range 760 - 1015 K (490 - 740°C). Discarding several anomalous data points, we can "fit" the remaining fifteen data points with the equation:



$$\text{Log } P = 9.92 - 6700/T ,$$

where  $P$  is the vapor pressure of  $\text{CsOH}$  in Pa and  $T$  is the temperature in K. Our transpiration experiments indicate that  $\text{CsOH}$  is much more volatile ( $\sim 20$  times higher vapor pressure) than  $\text{CsI}$  (See Fig. 3.1). This was not expected. It had been anticipated that  $\text{CsOH}$  and  $\text{CsI}$  would have comparable vapor pressures since analogous pairs of compounds,  $\text{NaOH} - \text{NaI}$  and  $\text{KOH} - \text{KI}$ , do exhibit a similarity of vapor pressures. We also determined that  $\text{H}_2\text{O}$  added to the carrier gas had no significant interaction with  $\text{CsOH}$ .

We obtain kinetic data by the use of a microbalance. Specimens of prototypic reactor-wall material are suspended from the balance and a gas containing the vapor species flows past the specimen. Mass changes are monitored continuously. We measured the desorption rates of tellurium from solid-solutions of tellurium in nickel over the temperature range 1070 - 1253 K (800 - 980°C). Our data are well represented by the equation:

$$\text{Log } k = 4.61 - 9500/T ,$$

where  $k$  is the tellurium desorption rate in  $\text{mg Te/cm}^2/\text{minute}$  and  $T$  is the temperature in K. We observed no increase or decrease in this rate when  $\text{H}_2\text{O}$  vapor was added to the carrier gas. Future microbalance experiments will measure the rates of absorption of  $\text{CsOH}$  and tellurium on stainless steel.

### 3.2 Interim Raman System

An interim cell was designed and fabricated for use with the Raman system before the Fission Product Reaction Facility (FPRF) is fully built and tested. The main purpose of this interim cell is to provide an environment for determining the Raman spectra of fission-product species that have not been previously studied and for calibrating the Raman signal with known species concentrations. The interim cell was not designed to achieve the extremely high temperature levels, the variation of residence times, or the multiple fission-product injection capability that will be possible with the FPRF. It will, however, provide us with a very flexible portion of the experimental program that will be able to answer detailed questions about fission-product chemistry in a timely manner.

A schematic diagram of the interim Raman cell is shown in Fig. 3.2. The furnace elements of the interim cell are in two abutting but separately-controlled segments. The lower segment surrounds the "evaporation" crucible (which contains the fission-product sample being studied), and by control of the crucible's temperature the partial pressure of the fission-product compound is determined. The upper segment surrounds the chimney through which the carrier gas and fission-product vapor species are transported to the laser beam. This furnace segment is always at a higher temperature than the lower segment in order to prevent any condensation of the fission-product compounds. The carrier gas enters the bottom of the lower furnace segment, flows around and through the furnace heater windings, continues flowing down into the evaporation crucible, and then flows up into the chimney.

A schematic diagram of the experimental setup is shown in Fig. 3.3. The interim cell is located in the center of this figure and the

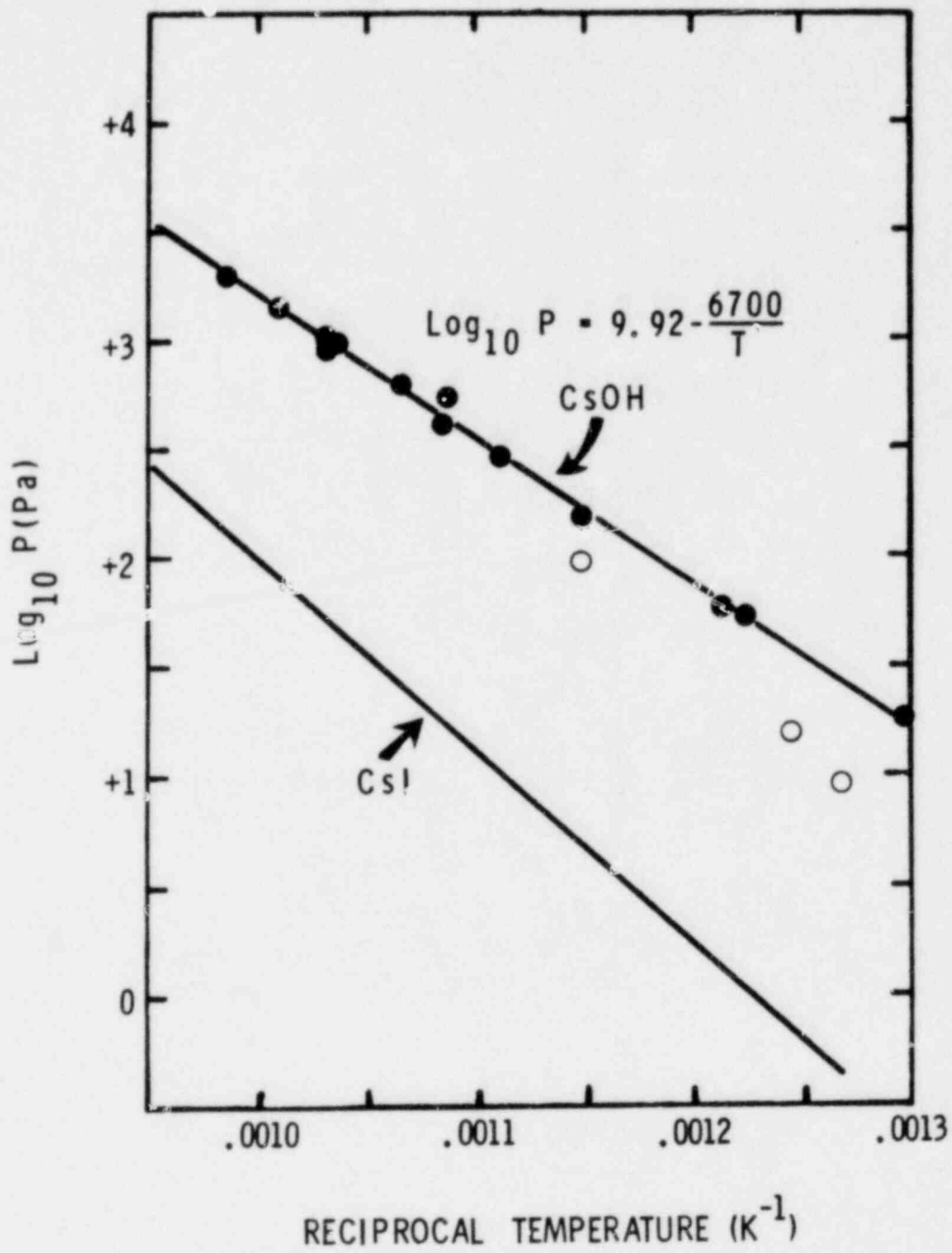


Figure 3.1 Vapor Pressure of CsI and CsOH.

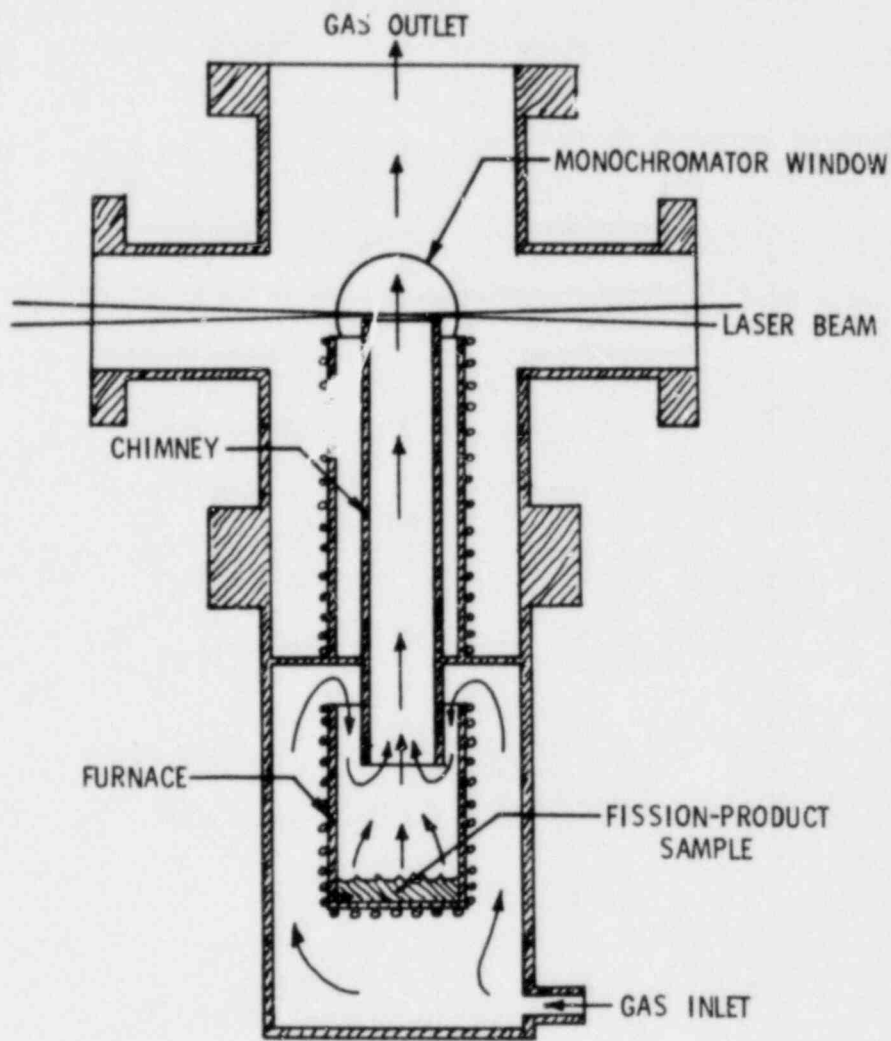


Figure 3.2 Schematic Diagram of the Interim Cell

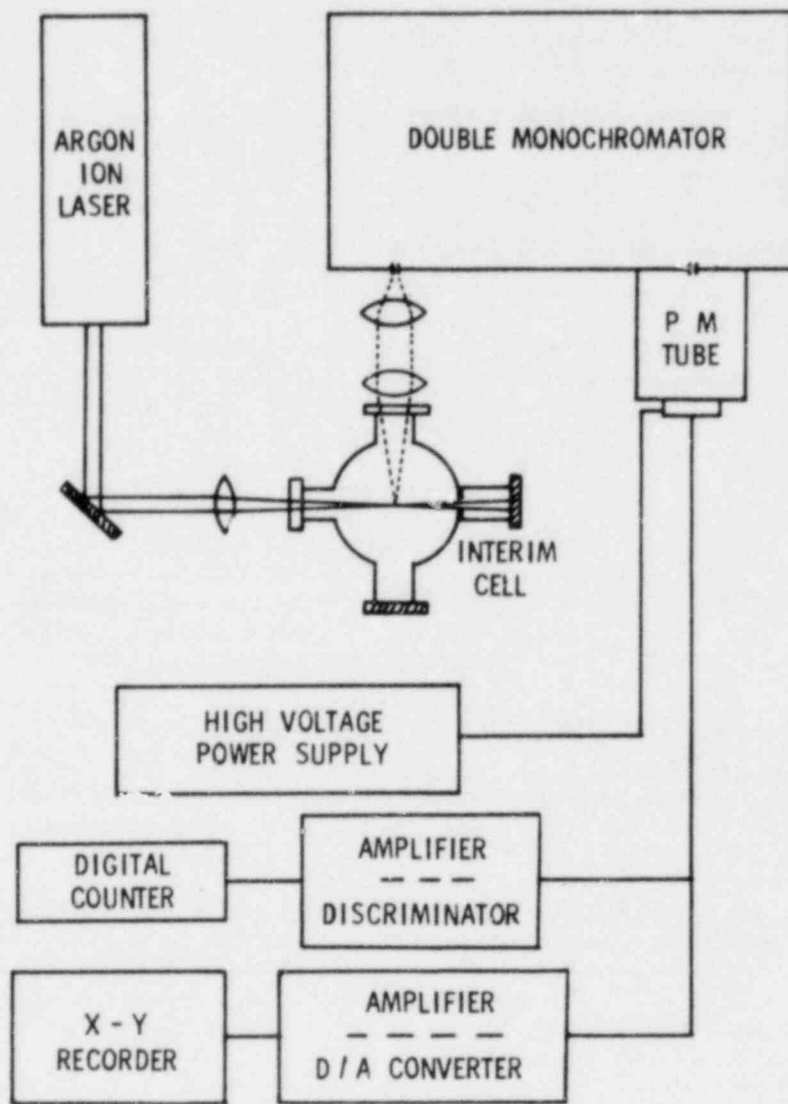


Figure 3.3 Schematic Diagram of the Experimental Raman Setup

remaining items shown are parts of the Raman system. A Spectra Physics argon-ion laser (1.5 watt at 488.0 nm) is used as the high intensity source for Raman excitation. The argon-ion laser beam is focused inside the interim cell just above the chimney (see Fig. 3.2). A portion of the light that is scattered at 90° to the laser beam is collected by two lenses and focused on the entrance slit of the Spex double monochromator. The light detector is a cooled and RF-shielded photon-counting PM tube (RCA C31034). The PM tube output can be displayed on either a counter or an x-y recorder.

It is possible to measure the gas temperature by recording the rotational Raman Spectrum<sup>(3)</sup>. Figure 3.4 shows two H<sub>2</sub> Stokes rotational spectra recorded in the interim cell. Figure 3.4A was recorded at room temperature and 3.4B at elevated temperature. If the logarithm of the normalized Raman intensities,  $\log [I_S(J)/\nu^4(J) G(J)]$ , is plotted as a function of the rotational term value,  $F_0(J)$ , the slope of the resulting line is related to the rotational temperature. This procedure was carried out for the data shown in Fig. 3.4 and the results are displayed in Fig. 3.5. As indicated, the room temperature spectrum yielded a temperature of 302 K and the elevated temperature spectrum corresponded to a temperature of ~ 690 K. The gas temperature for experiments in the interim cell and the FPRF will be determined using this Raman spectroscopic technique and standard thermocouples.

The main purpose of the interim cell is to provide known concentrations of various fission-product species in order to calibrate the Raman system. We will be able to measure absolute Raman cross sections by comparison with N<sub>2</sub>, which is generally used as a standard<sup>(4)</sup>. Depolarization ratios will also be measured using a polarizer oriented parallel and perpendicular to the laser polarization<sup>(4)</sup>.

### 3.3 Fission-Product Reaction Facility (FPRF)

The purpose of the Fission-Product Reaction Facility is to study the chemistry resulting from the reaction of single or multiple fission-product vapors (non-radioactive species) and steam at high temperatures. This laboratory-scale facility provides residence times as long as several hours for chemical and physical changes to occur among the reactants. Initially, the reactants include fission-product vapors, steam, the containing material of the system, and gases such as hydrogen and oxygen. These separate effects tests support the development of the TRAP-MELT code<sup>(1)</sup> which describes the transport and deposition of radionuclides in primary systems of light water reactors following hypothetical meltdown accidents.

The facility will provide superheated steam, from about 500°C to greater than 1000°C, into which single or multiple fission-product vapors can be injected in concentrations less than 10<sup>-3</sup> gm/cm<sup>3</sup>. Walls of the system will be maintained at the steam temperature. Residence times for chemical and physical changes to occur can be as long as several hours. The type and amount of species produced by reaction among the fission vapors, steam, and the reaction-vessel material will be measured in situ using Raman spectroscopy. The product species will then be selectively condensed to identify their final physical characteristics. Non-condensable product gases will also be identified if possible.

Facility design is based on the premise that thermodynamic and chemical conditions of the experiment can be controlled and measured if a "steady state" can be achieved while reactions are proceeding. This can be accomplished, as required in these studies, in a slow

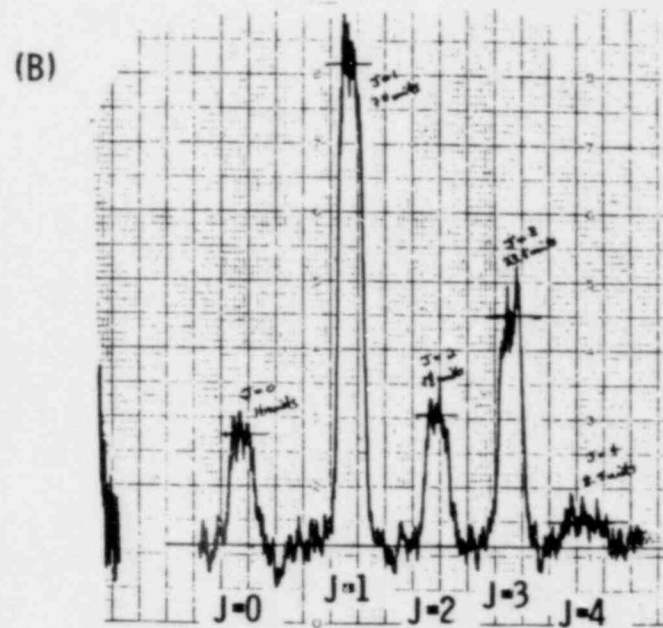
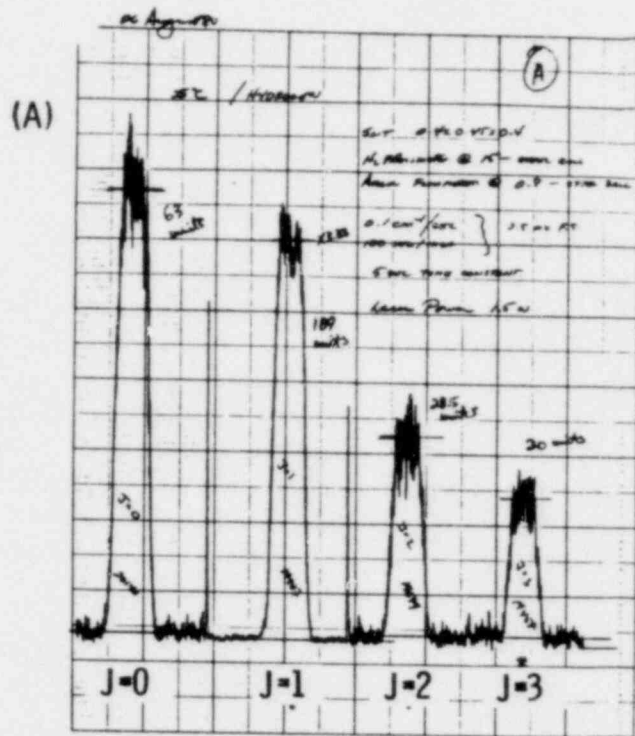


Figure 3.4 Pure rotational Stokes Raman spectra of hydrogen recorded in the interim cell.

A) room temperature

B) elevated temperature

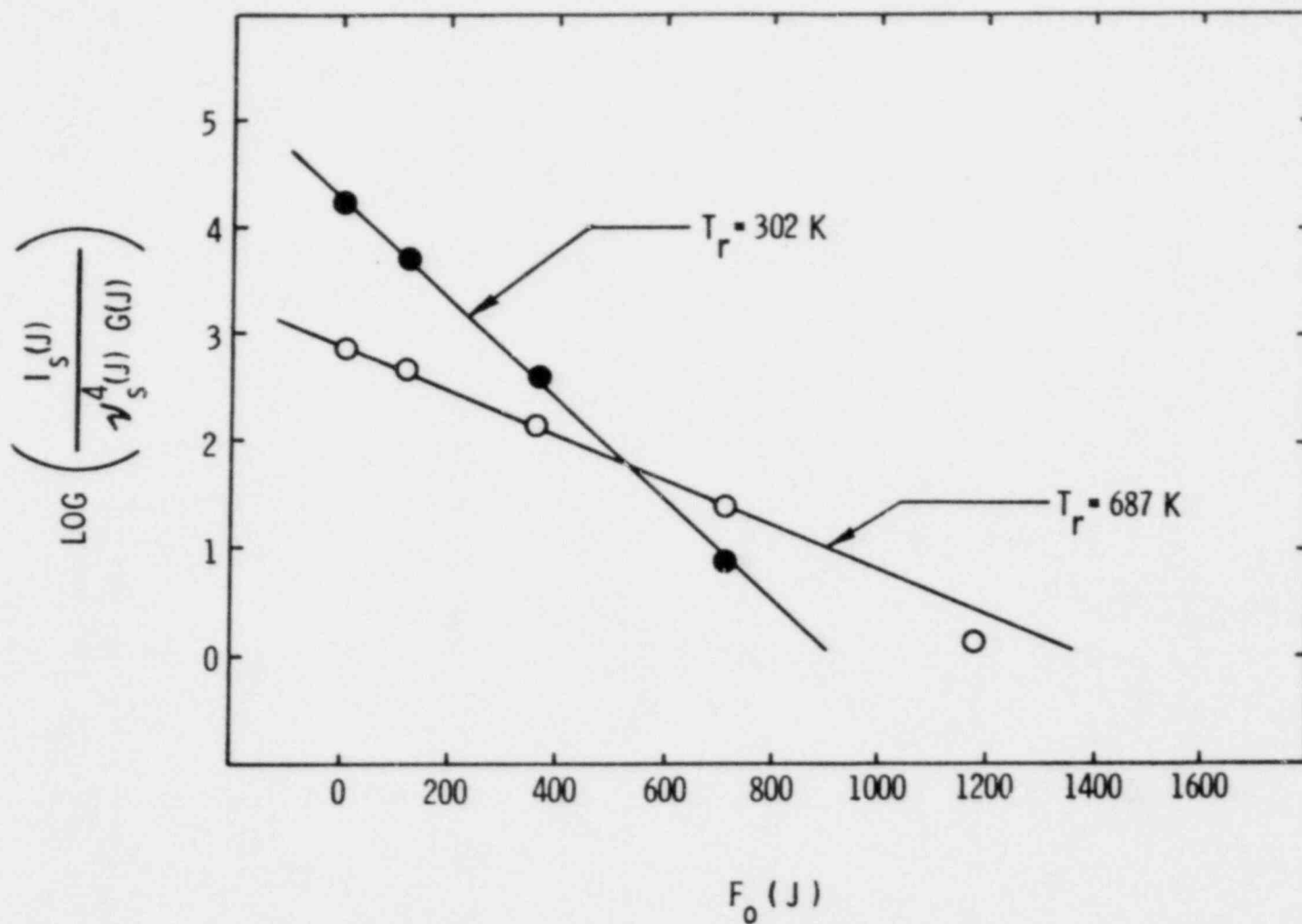


Figure 3.5 Plot of the rotational term value,  $F_0(J)$ , versus the logarithm of normalized intensity (line slopes are related to the rotational temperatures). Data are from Figure 3.4.

flowing (or quasi-static) system. Here reactions proceed with time, but once chemical equilibrium with the walls of the systems is established, conditions at any given position in the system should not change with time. This can be accomplished only if steady-state conditions can be established on both the steam system and on the rate of generation of fission-product vapors.

The FPRF (Fig. 3.6) is constructed throughout of 304 stainless steel. The maximum temperature attainable with this system will depend on the steam pressure and material strength (which will degrade due primarily to corrosion of the stainless at high temperature and with time). Steam pressure will be maintained close to ambient pressure. Modular design of the system aids in inspecting and cleaning internal surfaces of the components, in replacing and rearranging components, and in accurately inserting and removing sampling coupons located throughout the system.

The upstream portion of the facility consists of a water reservoir, boiler, super heater, flow controlling orifice, and fission-product vapor generators. Downstream of the generators, flow is directed by valves into one of two flow legs. One leg will be used for adjusting and stabilizing the flow and the fission-product conditions. It consists of a simple condenser, pressure gage, gas analyzer, filter, and valve. The other leg includes: the reaction chamber which provides long residence times for the reacting species; the Raman cell for measuring the amount and type of reaction products at temperature; and a parallel-plate condenser for selectively condensing the products for later examination of their physical and chemical characteristics. Also duplicated in this leg are a pressure gage, port for gas analysis, filter, and valve.

Not shown in Fig. 3.6 are radiation shields which stand off about 5 cm from the system and surround all the components that carry superheated steam. Calrods between the shields and the system keep the steam and walls at a constant temperature up to the condensers. The baffles are wrapped with about 15 cm of high-temperature insulation.

The FPRF has been completely designed in its conceptual form and all the detailed shop drawings have been completed for the components. All components have been fabricated except the Raman cell which is in the process of being manufactured. All commercial parts have been received. The facility has been 50% assembled on its portable table and 20% of the proof testing has been completed.

### 3.4 References

1. H. Jordan, J. A. Gieseke, and P. Baybutt, "TRAP-MELT User's Manual," Battelle Columbus Laboratories (February 1979).
2. Handbook of Chemistry and Physics, Chemical Rubber Co., (1964 and later editions); C. T. Ewing and K. H. Stern, J. Phys. Chem. 78, 1998-2005 (1979).
3. R. A. Hill, A. J. Mulac, and D. R. Smith, Appl. Spectrosc. 30, 183 (1976).
4. J. C. Cummings, R. E. Palmer, and D. P. Aeschliman, Opt. Comm. 27, 455 (1978).



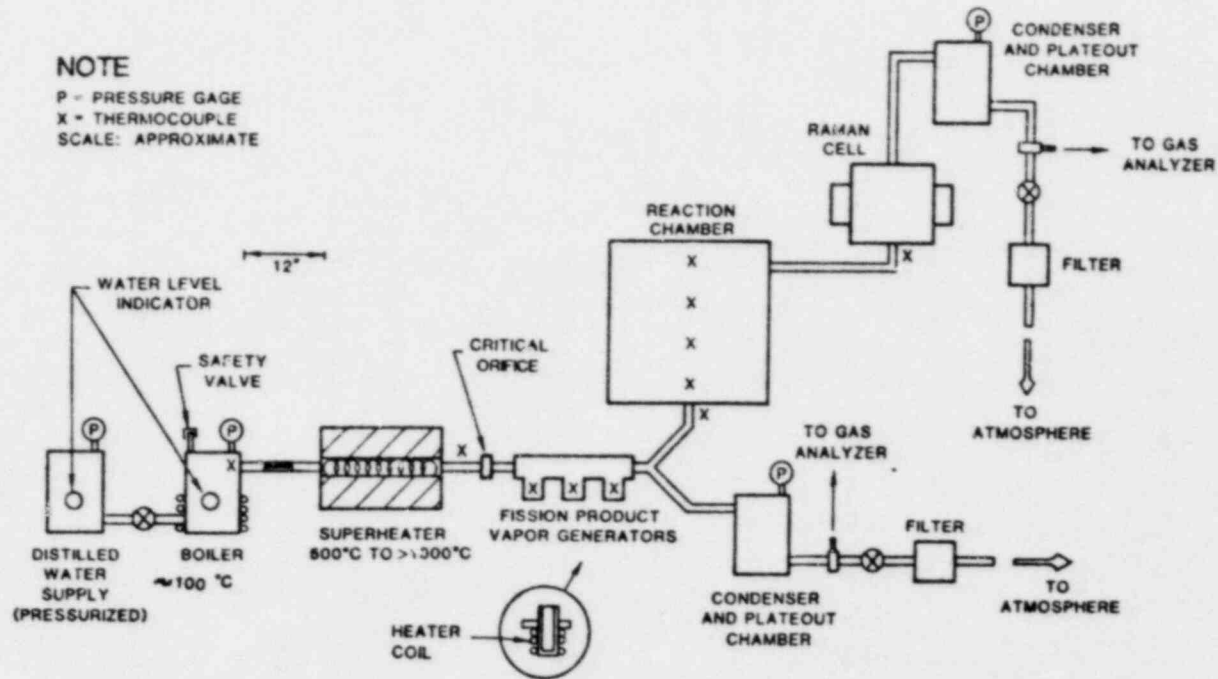


Figure 3.6 Schematic diagram of the Fission Product Reaction Facility (FPRF).

#### 4. Containment Emergency Sump Performance (G. G. Weigand, M. Berman, R. R. Prairie)

##### 4.1 Summary

A loss-of-coolant accident (LOCA) in a pressurized water reactor (PWR) will normally activate the reactor's emergency core cooling system (ECCS). The ECCS supplies coolant to the reactor core to dissipate the decay heat, and under certain conditions, to the containment spray system (CSS) to reduce containment pressure and scrub radioactive material from the containment environment. A failure of the ECCS can be serious; the disruption of core coolant flow could lead to core damage.

The containment emergency sump performance (CESP) program will investigate the reliability of ECCS sumps. The CESP program provides technical direction to the DOE-sponsored experimental sump program at Alden Research Laboratory (ARL), and it has two main purposes:

- to provide a containment-sump data base to NRC, and
- to provide ECCS sump design information to the nuclear industry.

The test facility is complete and operational; the problems that were found during the facility check-out and initial testing have been or are being corrected. Additionally, a second void fraction meter is being installed so readings on both outlet pipes can be recorded. However, the test program is behind schedule for two reasons. First, ARL has found that it takes longer to reconfigure and test than originally estimated; secondly, ARL was required to interrupt the test program to correct difficulties with the grade line measurement and with the void fraction meters response. Only eleven of the scheduled nineteen configurations will be tested by 30 September 1980.

Meetings at NRC and DOE on 18 & 19 September 1980 resulted in a time table for accepting and implementing ARL's proposal for the entire test program.

A data analysis and data presentation plan for each configuration was developed to supplement the factorial analysis plan outlined in Reference 1 (April-June 1980 quarterly). Preliminary results from the first configuration tests are shown; these results, although inconclusive in trends, still tend to deviate from some of the generally accepted "rules of thumb" which are widely used throughout the industry. Additionally, several interesting phenomena, which have not been reported before, have been observed during the testing; one such phenomenon was a horseshoe-shaped vapor core vortex which stretched between the two outlet pipes and formed beneath the surface.

##### 4.2 Test Facility

The CESP test facility has been completed and the instrumentation has been verified as operational. ARL has supplied the following facility description:

The test facility (Figure 4.1) consists of a main tank with sump, suction pipes with variable diameters and positions, a pump pit tank, and associated piping for the simulation of

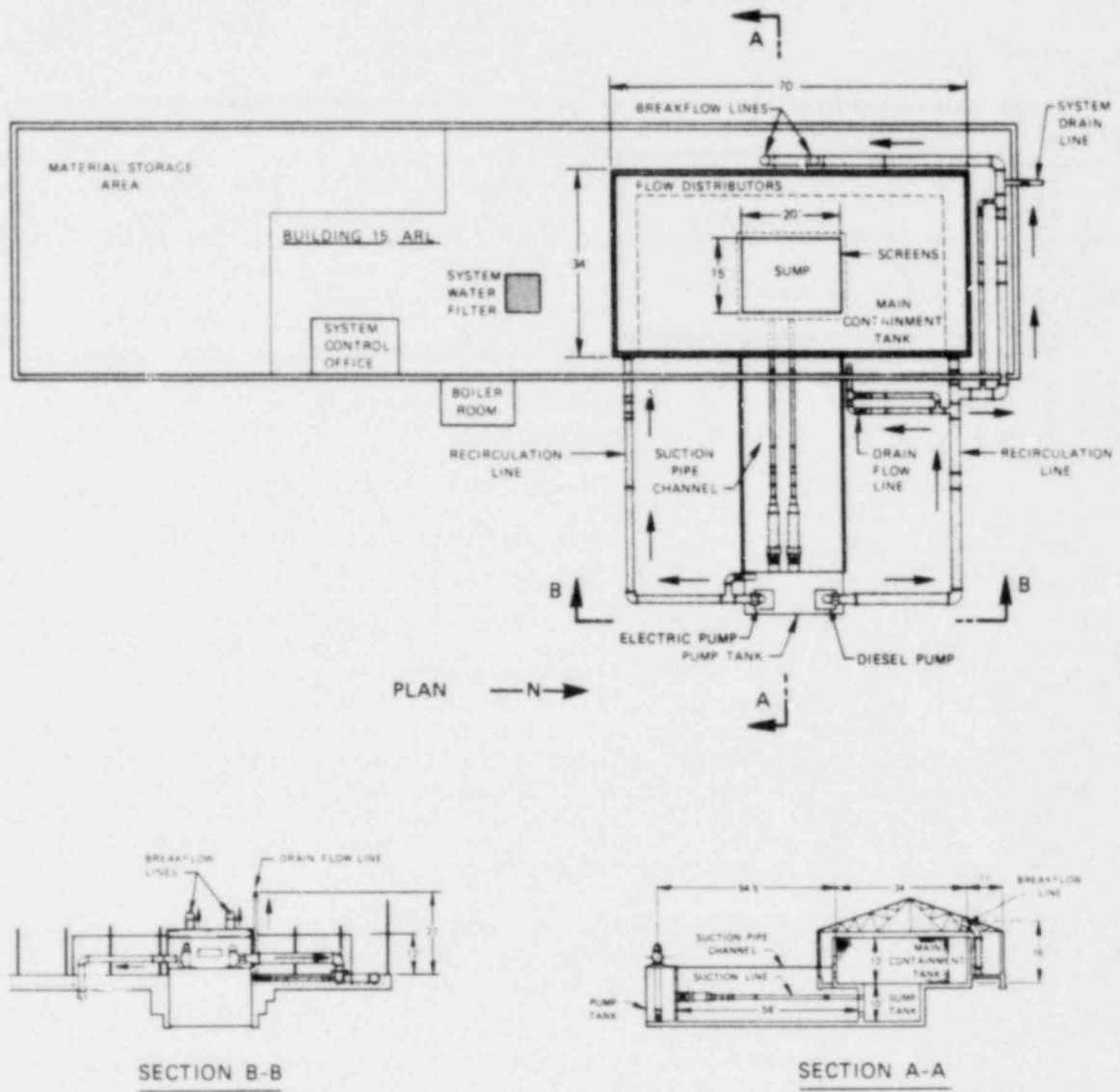


Figure 4.1 Plan and Sections of the Facility.

break and drain flows. The maximum capacity of the main tank is 250,000 gallons of water with the ability to position false walls within the tank to achieve a wide range of sump configurations. A continuous filtration system provides water quality down to 10 microns and a heating system is capable of increasing the temperature of the water to 140°F. Two suction pipes connect the main tank to the pump pit tank and are variable in four sizes from 8 inch to 24 inch diameter. A total of 15 pipe holes arranged in 3 rows, with 5 holes each row, provide for numerous piping positions. Flow out of the main tank is maintained by a siphon and is controlled by electrically operated valves on each of the suction pipes. The pump pit tank contains two pumps, a 40 HP electrically driven pump and a 300 HP diesel driven pump; both pumps being of vertical shaft design. Operation of both pumps produces 45 cfs of flow with up to 60% available for break flow and 10% available for drain flow.

Containment sump performance is determined by the observation of vortex formation in the main tank and the measurement of swirl, pressure gradient, and entrained air in the suction pipes. The use of electrically operated valves and a sophisticated data acquisition system, with computer interface, allows the test flow parameters to be set and test data to be taken (with the exception of vortex observations) from a single central office.

During the checkout testing, the settling and recording time for the pressure grade line was found to be longer than the originally planned thirty-minute scan, and the void meter response and calibration range were unacceptable. The critical nature of the above two discoveries required that the testing cease until the difficulties were resolved. The scan time for the pressure measurements has now been changed to 60 seconds, and, after consultation with the void-fraction meter's manufacturer, the meter and its reference point were relocated. However, periodic zeroing of the void fraction meter is still required.

#### 4.3 Test-Program Planning Status

Recent meetings (18 & 19 September 1980) resulted in agreement upon the program requirements that are necessary to resolve the sump question in TAP-43. ARL will restructure their program to accommodate these new directives. The present timetable for review of ARL's program is as follows:

1. ARL will deliver to Sandia and NRC a final draft of the entire proposed test program by 14 October 1980.
2. Sandia and NRC will review ARL's program and respond by 31 October 1980.
3. ARL will implement the total test program into their test schedule 1 October 1980.

(These above actions will not result in a testing delay since the first twenty-five tests were established in January 1980 and have not been changed.)

#### 4.4 Data Analysis

The analysis plan for the development of a fractional factorial response surface was detailed in Reference 1; from this analysis, we will provide the overall generic behavior of the undisturbed sump. However, configuration-by-configuration analysis is still required so comparisons can be made between the undisturbed sump study and the perturbation studies (blockage, breakflow, vortex suppression, nonuniform approach flow, etc.) and between the undisturbed sump study and the secondary variable studies (see Reference 1 for details). The description of the preliminary configuration-by-configuration data analysis plan is as follows. (Note: The data analysis of the perturbation studies will be performed in a manner similar to the following description except that there will be fewer data points. Additionally, there may be some slippage in the quantity of data for each configuration as a result of program redirection and reassessment.)

The analysis of the configuration data will consist of developing summary graphs and tables for the configuration tests. Data will be recorded for four responses (dependent variables): pressure grade lines (PLG), vortimeter revolutions (VR) vortex strength observation (VSO), and void fraction (VF). For a configuration (fixed geometry) data will be recorded at four submergence levels (s) and ten flow rates (Q). Two of the flow levels will be thirty minute data records (steady-state tests), and the remaining eight flow levels will be five minute data records (survey tests). Thus, there will be eight steady-state s-Q combinations and thirty-two survey s-Q combinations.

A series of graphs and tables will be developed

- For each of the eight steady-state s-Q combinations plots of PLG, VR, VSO, and VF versus time will be provided.
- For each of the four submergence levels plots of the mean values of PLG, VR, VSO, and VF will be provided. A measure of uncertainty will be shown for each of these plots.
- For each of the responses PLG, VR, VSO, and VF contour plots of mean response versus s-Q will be provided. Additionally, for VSO a series of contour plots will be provided which correspond to the probability of  $VSO = k$  where  $k = 1, \dots, 6$ .
- For each of the configuration's s-Q combinations, tables will be provided of the mean (X), the standard deviations (s), and the median for each of the responses PLG, VR, VSO, and VF.

Implementation of this present plan has begun; presently, we are in the process of writing software for sorting and reducing ARL's data files.

#### 4.5 Preliminary Data

Although the data analysis procedures are not completely operational, preliminary analysis is being performed as the configuration tests are taken. These early results are limited and are not numerous enough for recognizing any special trends. Figures 4.2 and 4.3 show typical time records for a 16' x 10' x 3' sump configuration; the outlet

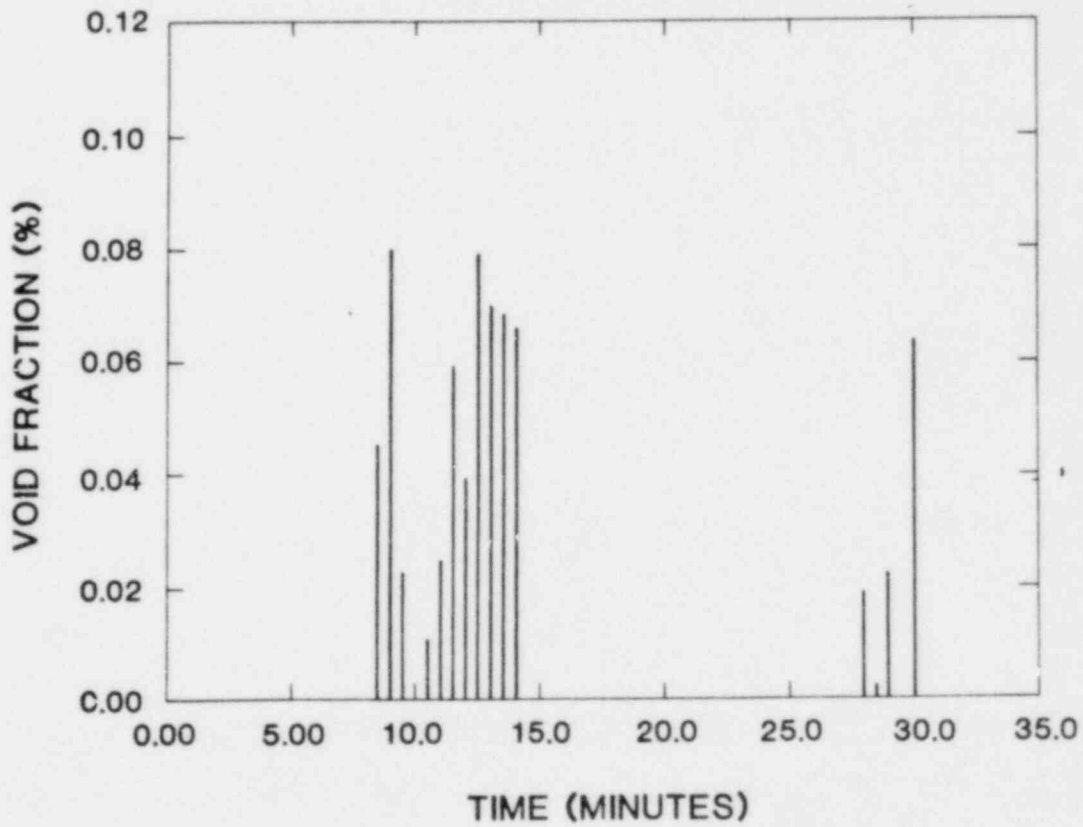
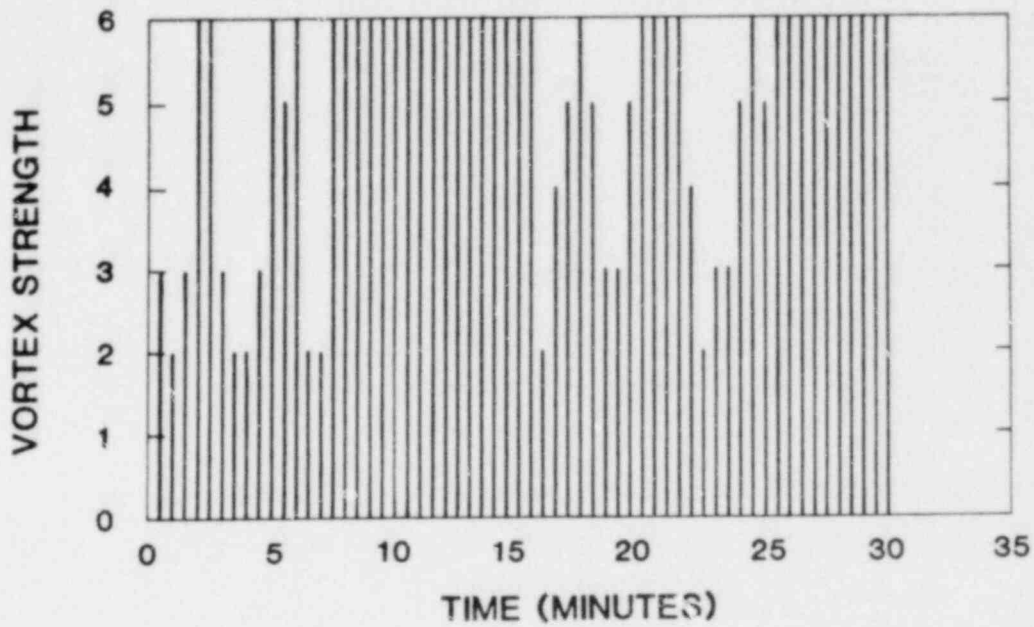


Figure 4.2 Vortex Strength and Void Fraction for a Steady State Test (30 Minute).  
 16' x 10' x 3' Sump, Outlet Pipe Spacing of 4'.

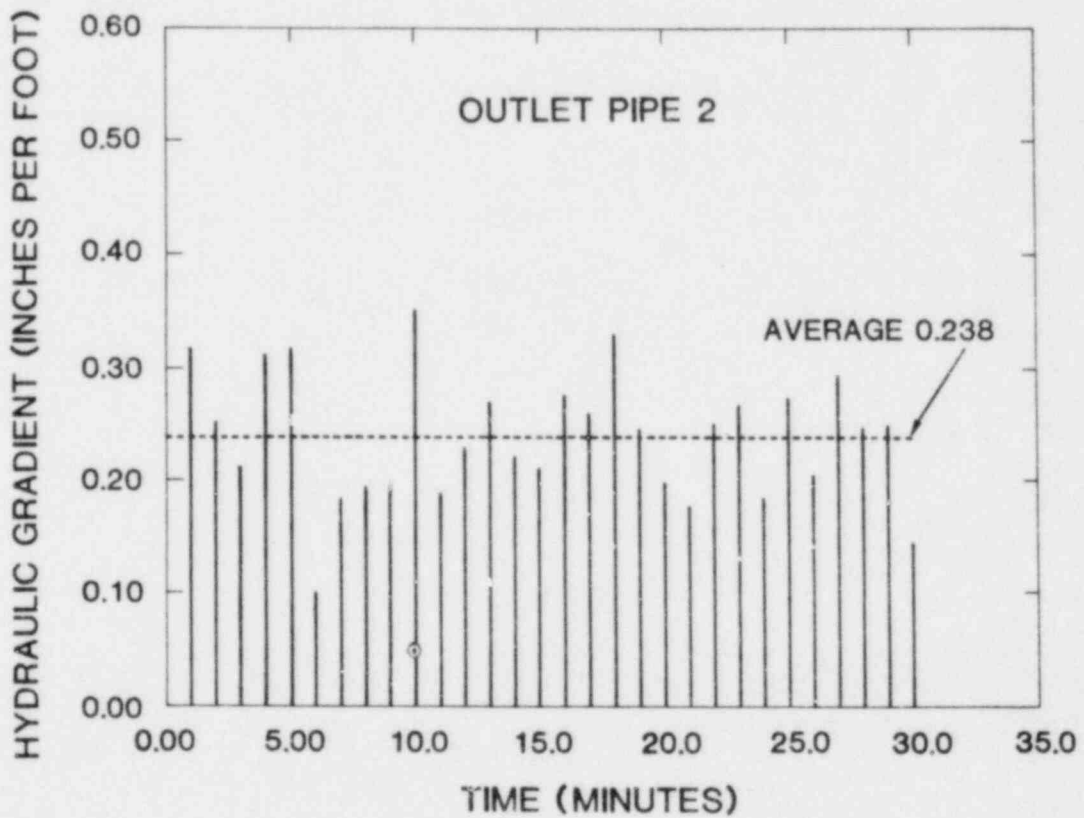
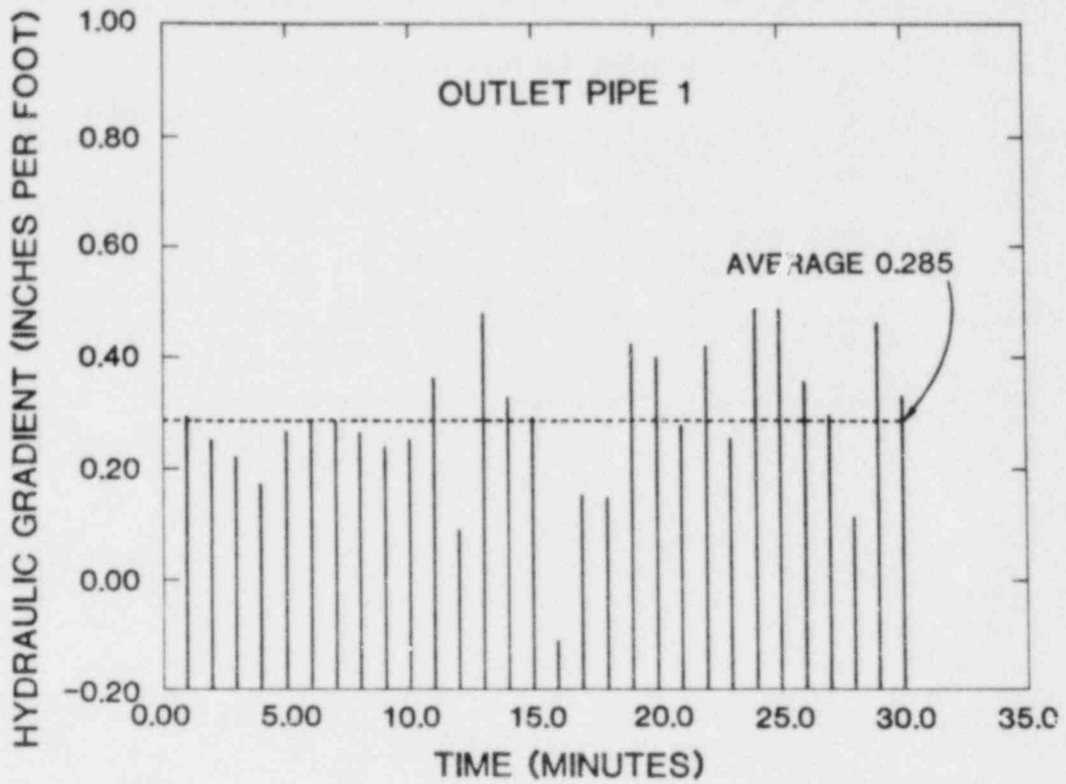


Figure 4.3 Hydraulic Gradient for the Two Outlet Pipes for a Steady State Test (30 Minutes). 16' x 10' x 3' Sump, Outlet Pipe Spacing of 4'.

pipe spacing is 4', the submergence is 6', and the flow rate is 5500 gpm. Figures 4.4 and 4.5 also show typical time records for a 16' x 10' x 3' sump; same conditions as above except that the outlet pipe spacing has been increased to 12'. Although conclusions drawn at this time are speculative, Figures 4.2 and 4.5 show several things. First the outlet pipe spacing has a clearly observable effect; the larger pipe spacing results (average vortex activity = 3.20, Figure 4.2) have a lower vortex activity than the 4' pipe spacing results (average vortex activity = 4.95, Figure 4.4). Furthermore, the test operators observed that the vortices which form when the outlet pipes are close together are submerged horseshoe-shaped vapor-core vortices which stretch between the two outlet pipes.

Additionally, it is interesting to note the preliminary correlation between void fraction and vortex activity; the initial results of Figures 4.2 and 4.4 show that the air core type vortices found in power reactor containments may actually draw only a small quantity of air.

Figure 4.6 shows some typical results as a function of submergence and flow rate. Although preliminary, these results are quite interesting. First, we see high vortex activity at the lower flow rates (< 4000 gpm) and secondly, we see that the highest vortex activity does not necessarily occur at the lowest submergence. These results are in direct conflict with two commonly used "rules of thumb".

- higher flow + more vortex activity
- lower submergence + highest vortex activity

Finally, Figures 4.7 and 4.8 are typical pictures of strong air-core vortices. To give some perspective of the size of the air-core vortex, the surface dimension is about 4 to 6 inches, decreasing to about 1/2 inch when entering the 12 inch diameter outlet pipe.



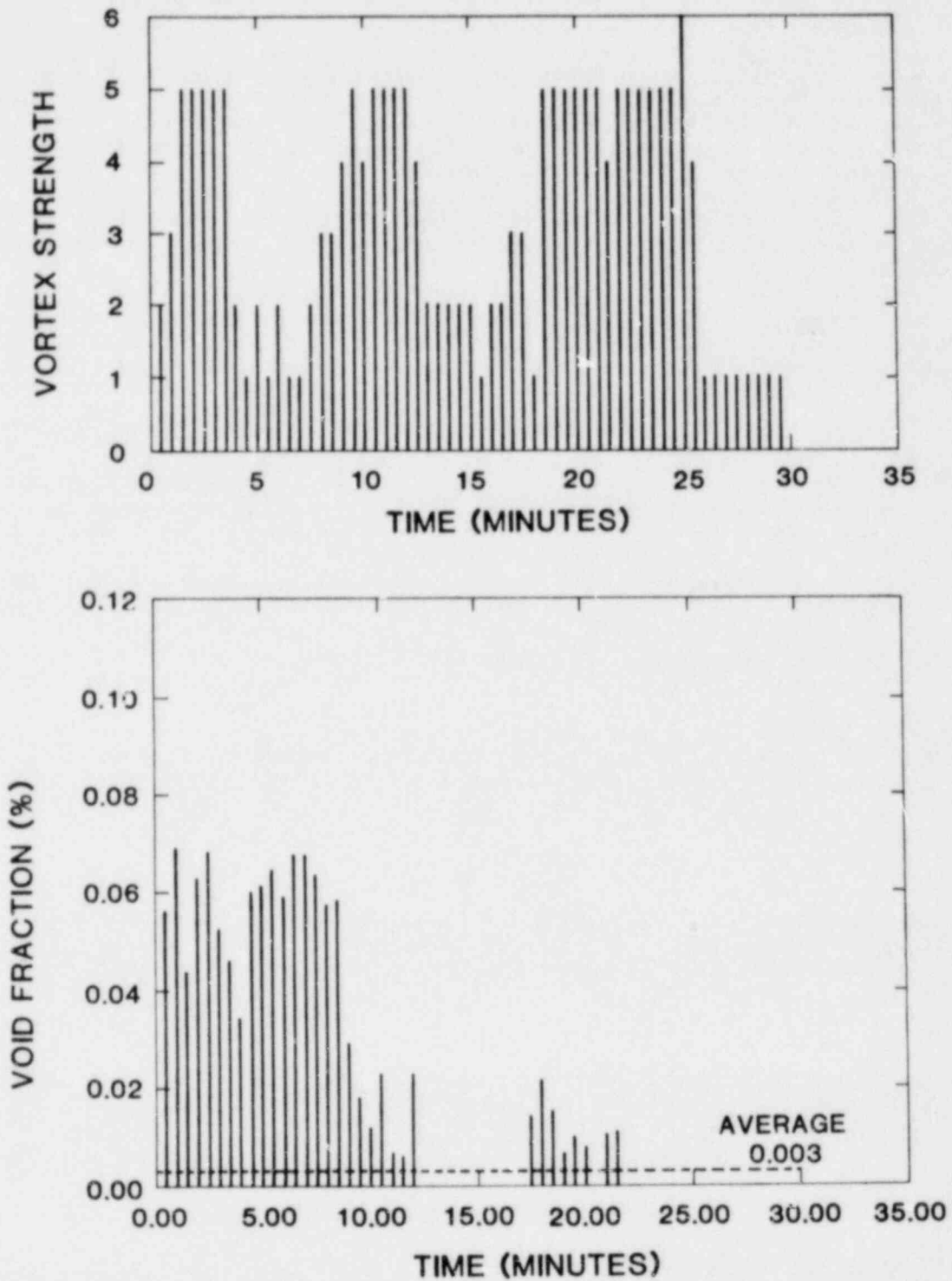


Figure 4.4 Vortex Strength and Void Fraction for a Steady State Test (30 Minutes).  
 16' x 10' x 3' x Sump, Outlet Pipe Spacing of 12'.

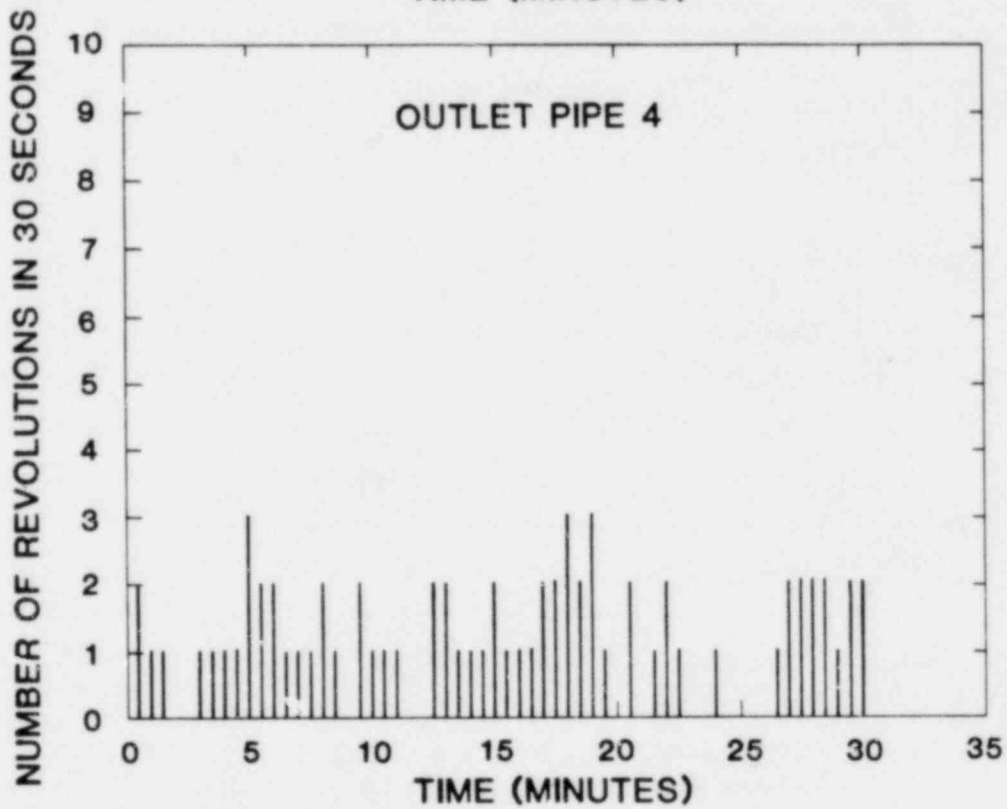
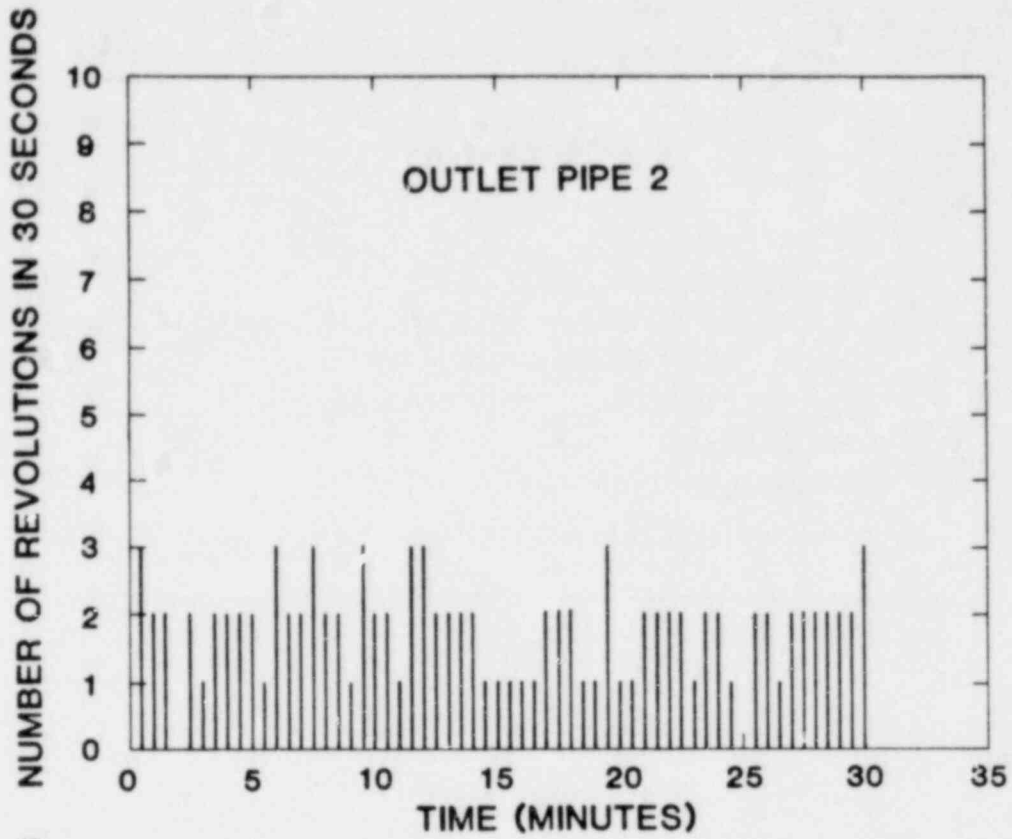


Figure 4.5 Vortimeter Revolutions for the Two Outlet Pipes for a Steady State Test (30 Minutes) . 16' x 10' x 3' Sump, Outlet Pipe Spacing of 12'.

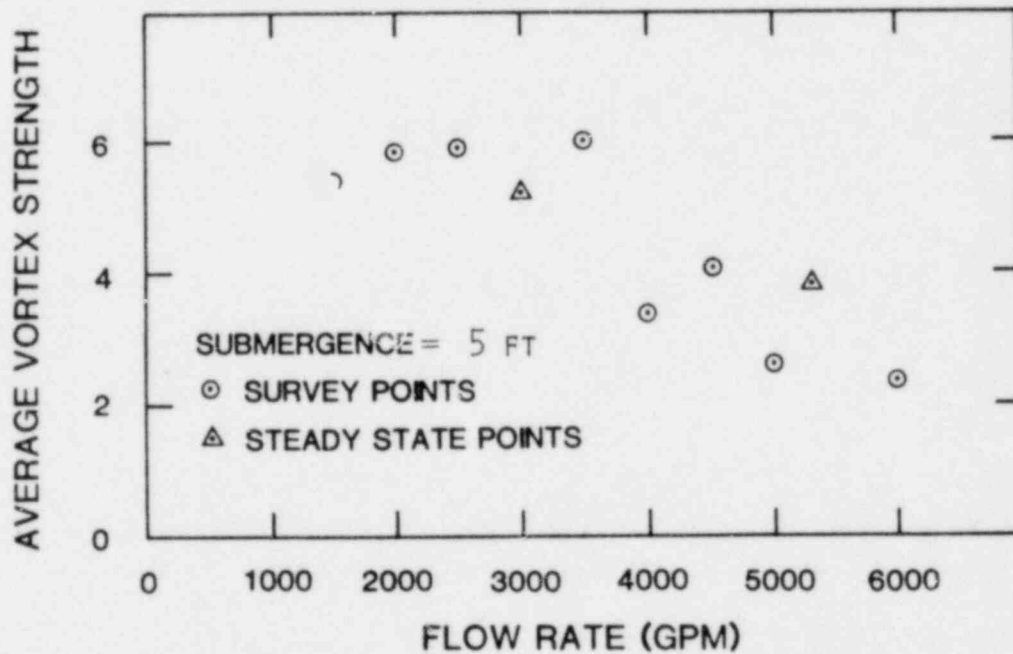
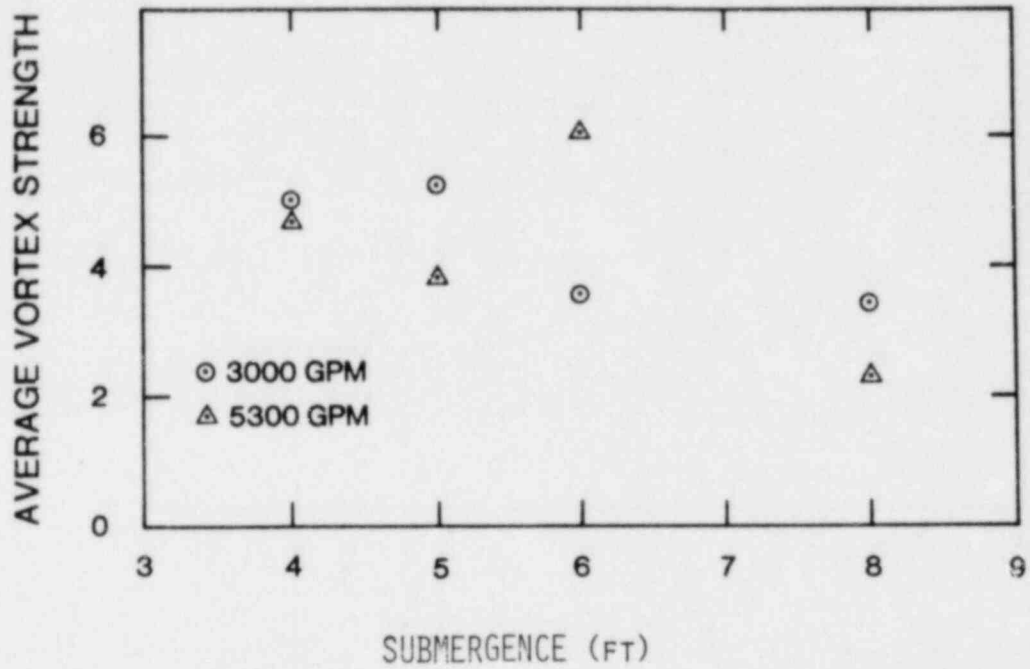


Figure 4.6 Typical Initial Results for Average Vortex Strength as Functions of Flow Rate and Submergence. 16' x 10' x 3' Sump, Outlet Pipe 8",acing of 4'.



Figure 4.7 Typical Air Core Vortex in the containment sump at a low water level. The grid that is reflected into the water from above is 1 ft x 1 ft.



Figure 4.8 Typical Air Core Vortex in the containment sump at a high water level. The grid that is reflected into the water from above is 1 ft x 1 ft.

## 5. Hydrogen Program

(J. C. Cummings, M. P. Sherman, M. Berman,  
M. R. Baer, E. C. Neidel, B. W. Burnham, R. K. Byers)

### 5.1 Summary

During the last quarter, we began to work on the Hydrogen Program. The objectives of this program are to quantify the threat posed by hydrogen released during LWR accidents and to generate information and equipment concepts which will prevent or mitigate that threat. Major end products of the program will be:

- An assessment of the hydrogen threat for several classes of nuclear power plants.
- An assessment of the adequacy of existing hydrogen safety systems and mitigation strategies.
- The identification and conceptual demonstration of improved hydrogen mitigation and detection systems.
- The publication of operator strategies, training booklets, and emergency manuals that deal with the hydrogen problem.
- Computer codes that address the transport and combustion of hydrogen in containment.

The areas of research that will be covered by the Hydrogen Program include: H<sub>2</sub> and O<sub>2</sub> generation and transport; H<sub>2</sub> and O<sub>2</sub> detection; hydrogen combustion; and mitigation and prevention of damage from hydrogen combustion. Our effort will include literature reviews, power plant characterization, and industry contact in addition to major analytical and experimental research. A detailed program plan will be presented to the NRC during the next quarter.

The following sections will discuss our efforts on the Hydrogen Program during the last quarter. Other than the work on the Hydrogen Compendium, the bulk of the effort has taken place only during the last month. Three mitigation schemes are being examined as part of a short-term program to address important licensing questions for the Sequoyah power plant. Combustion analyses have been carried out with new computer codes to calculate peak quasi-static, and steady detonation loads and with an existing code, CSQ, to compute dynamic behavior. Hydrogen detection instrumentation has been surveyed through utility and industry contacts. The experimental program plan was not fully developed during this quarter - therefore, its discussion is postponed to the next quarterly report.

### 5.2 The Hydrogen Compendium

During this quarter, we published a document entitled "The Behavior of Hydrogen During Accidents in Light Water Reactors." This report represents the efforts of a number of individuals in reviewing the literature pertinent to understanding the behavior of hydrogen in a nuclear reactor environment. Four major topics were addressed: hydrogen generation and solubility; hydrogen and oxygen detection systems; hydrogen combustion; and hydrogen recombiners.

A draft version of the report was widely circulated and reviewed. In general, the document was very favorably received. Our intention

is to publish an updated version of the document in the future which will further investigate some controversial areas and add significant new results. An operator's manual, based on the information contained in the compendium, will be written as a separate document, on a time schedule consistent with NRC needs and priorities.

### 5.3 Hydrogen Mitigation Techniques for Sequoyah

We have begun a short-term (2-3 month) effort to investigate the effectiveness and practicality of three hydrogen control measures: (1) deliberate ignition; (2) Halon addition after accident initiation; and (3) water fogging. The objective of the investigation is to provide the NRC with an early assessment (prior to December 1, 1980) of the efficiency and practicality of these three mitigation schemes for degraded (still coolable - not molten) cores. We will attempt to assess whether these mitigation schemes can lessen the effects of accidents that involve damaged cores. We will also try to determine if installation of the mitigation system will degrade or improve safety. The NRC has specific questions regarding each of the three mitigation schemes which we will address in a status report (October 31, 1980) and a final report (November 30, 1980).

The following sections discuss our work on this effort during the last month of the quarter. Thus far, we have initiated literature reviews, contacted industry and laboratory representatives, performed simple hand calculations and carried out some computer code computations. The effort is well under way and progress is being made on all three mitigation schemes.

#### 5.3.1 Deliberate Ignition

The use of deliberate ignition requires an understanding of the combustion of lean hydrogen:air:steam mixtures and the theory of ignition.

Lean hydrogen mixtures, below 9 volume % hydrogen, burn in a unique fashion. For extremely lean mixtures, 4-6%, the flame temperature is below the spontaneous ignition temperature. The upward propagation of the flame takes place in flame globules into which hydrogen rapidly diffuses giving locally richer mixtures, hence locally higher temperatures. The overall combustion is incomplete. Experiments have produced conflicting results on the fraction of hydrogen consumed versus the initial hydrogen concentration. The works of Furno, et al., (1) and others (2) with spark ignition show a very low fraction of hydrogen consumed up to about 8% hydrogen.

The work of Canadian researchers for combustion in a vertical tube shows large fractions of hydrogen consumed down to 5% hydrogen (3). The difference may be due to vessel geometry, ignition method, and igniter location. We are presently trying to explain the conflicting results.

Since there are no data on the combustion of lean hydrogen mixtures in very large chambers the size of reactor containments, prediction will require an understanding and extrapolation of the combustion behavior in intermediate-sized chambers where there are data. If the behavior is governed by the formation of flame globules a few inches in diameter, in presumably a conical type region, and if there are no other scale effects, it may be possible to predict the pressure rise in containments caused by the deliberate ignition of lean mixtures.

We are examining the literature on the ignition of hydrogen mixtures by sparks and by hot surfaces (glow plugs). There are several approximate theories and several sets of experimental data, but these are generally for mixtures not far from stoichiometric. Data on the minimum ignition energy for sparks in hydrogen:air mixtures are well known for more combustible mixtures but not for mixtures near the flammability limits.

### 5.3.2 Water Fogging

The potential mitigating effects of a water fog (small liquid droplets) on hydrogen combustion are illustrated in Figs. 5.1 and 5.2. As the volume fraction of drops increases from 0 - 0.05%, the post-combustion temperature and pressure are drastically reduced (assuming complete evaporation). For a  $2.0 \times 10^6$  ft<sup>3</sup> containment, 0.05 volume % drops would require only 10<sup>3</sup> ft<sup>3</sup> (62,000 lbs.) of water. A major question about water fogging concerns droplet size - small enough to evaporate quickly and settle out slowly but large enough to be produced by available nozzles. These matters are discussed in greater detail in the following sections - water fogs in hydrogen:air deflagrations and detonations.

#### 5.3.2.1 Water Fogs in Deflagrations

Investigation of water fog mitigation, for reducing the pressure rise caused by combustion within containment, was initiated to define vaporization characteristics, spray properties, and settling time. An independent calculation of vessel temperature and pressure (isochoric equilibrium) in H<sub>2</sub>:air:water environments was performed to serve two purposes: first, to check on preliminary calculations presented in our compendium<sup>(4)</sup>; and second, to provide ambient conditions for a vaporization model. Calculations of final temperatures and pressures were compared against available experimental data found in Lewis and Von Elbe<sup>(5)</sup>, and the accuracy of the earlier calculations was confirmed.

We then added a model of monodispersed water droplets to this code to predict the time required for complete vaporization. A preliminary investigation of the model's prediction was performed by comparing to existing experimental data for vaporization of isolated droplets in heated air<sup>(6)</sup>. Vaporization times agreed to within a few percent of the experimental data. We then added to this model the corrections necessary for convectively-enhanced vaporization induced by the gas which is accelerated by a deflagration. These corrections were significant for vaporization of droplets in excess of 250  $\mu$ m in diameter. Vaporization times were predicted for droplet sizes varying from 1 to 10,000  $\mu$ m in diameter and for various stoichiometries of the hydrogen combustion environments. The calculations indicate that droplets less than 300  $\mu$ m in diameter will vaporize within 1 sec after initiation of evaporation.

Preliminary calculations have been performed to determine where (when) vaporization is most likely to occur. For vaporization to occur within the flame zone of a laminar deflagration, necessary residence times are calculated to be of the order of  $10^{-4}$  sec. To achieve this vaporization time, the water droplets would have to be less than 3  $\mu$ m in diameter. Current modifications of the code are being directed toward examining local mixing effects near a vaporizing droplet.

A separate part of this study has been initiated to define typical droplet sizes and distributions from various atomization techniques. Atomization techniques for high-output generation of aerosols utilize



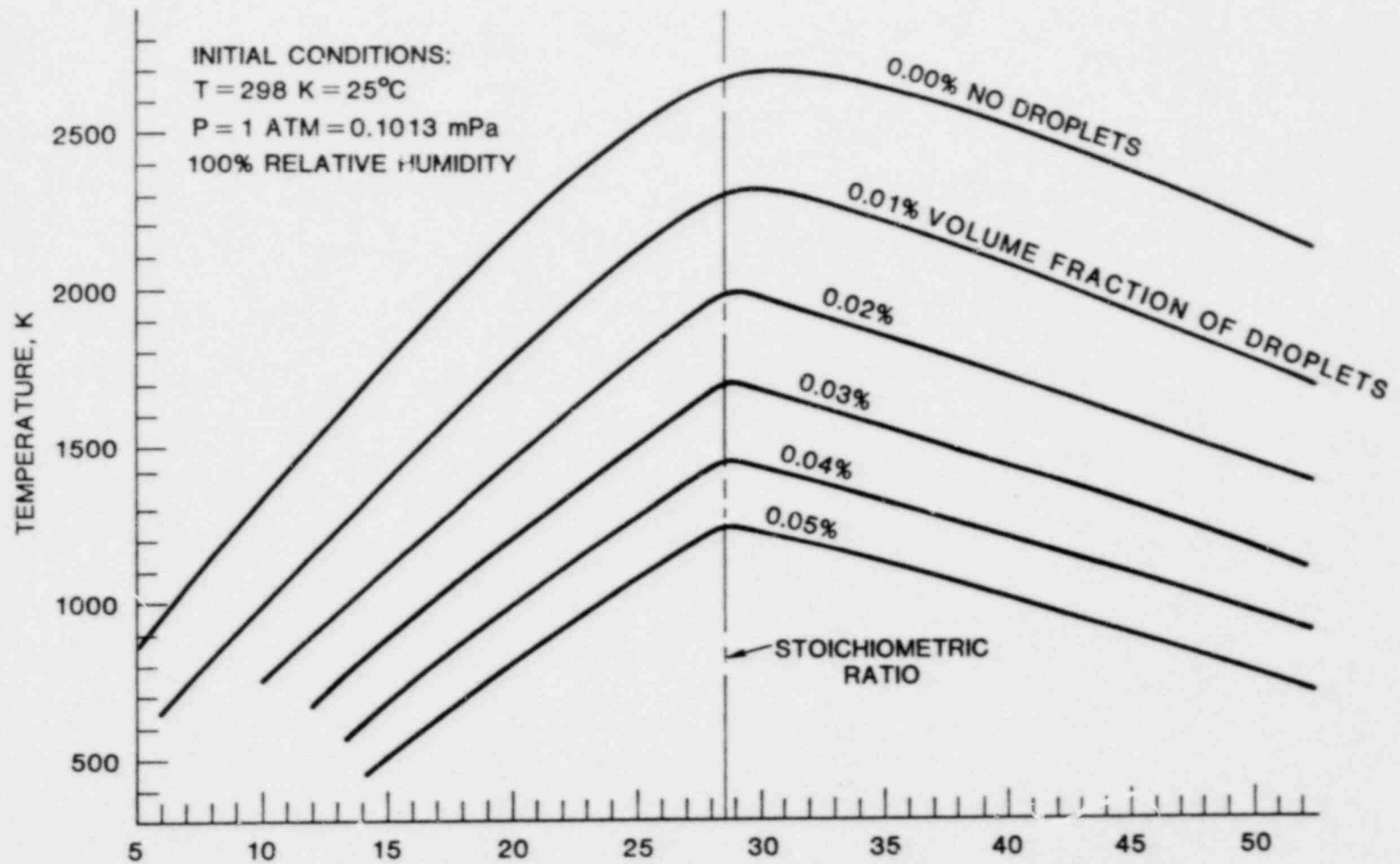


Figure 5.1. Effect of Droplet Vaporization on Adiabatic Isochoric Hydrogen Combustion

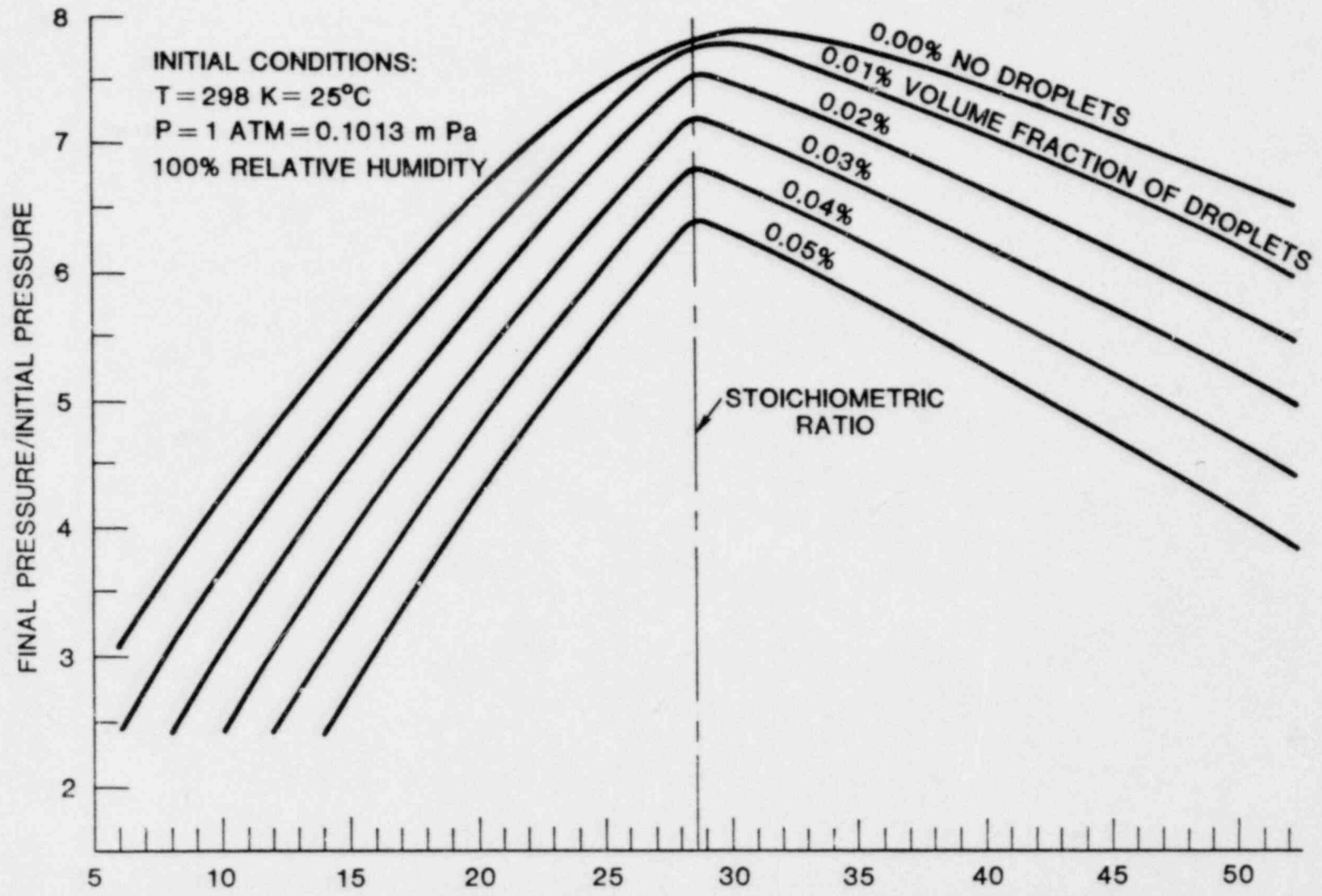


Figure 5.2. Effect of Droplet Vaporization on Adiabatic Isochoric Hydrogen Combustion.

nozzles or rotary generators. Typical distributions of droplet sizes produced by these devices are polydispersed (covering a range of droplet size) with mean droplet diameters from 10 to 5000  $\mu\text{m}$ . For production of small mean droplet size ( $\sim 10 \mu\text{m}$ ), an air-blast/swirl-type nozzle is necessary. For smaller drop sizes, specialized nozzle systems are required. This survey indicated that direct quenching of hydrogen deflagration would not occur if conventional nozzle systems are used since mean droplet sizes have diameters greater than 3  $\mu\text{m}$ . Most of the vaporization will occur in burned regions behind the deflagration front. This suggests the possibility of combining deliberate ignition and water fogging.

Another part of this study has been directed toward predicting particle settling of high-mass-density aerosols. We performed some calculations of the settling losses, neglecting agglomeration effects. For high-mass-density aerosols, this is a nonconservative approximation and particle-particle collision effects must be examined. The physics of coagulation is determined by the effects of Brownian motion, turbulence, gravitational settling, and wall interaction. We determined that for water droplets  $> 1 \mu\text{m}$  in diameter, coagulation within a containment vessel is dominated by gravitational effects. A mono-dispersed distribution of small droplet sizes would tend to reduce these effects. Unfortunately, the theory of well-stirred settling is not as straightforward as the drag calculations and solution of the kinetic integral-differential equations is required. Our current investigation is directed toward producing computer codes which can be used for this calculation.

#### 5.3.2.2 Water Fogs in Detonations

We are beginning to investigate three questions concerning the effect of fogs on detonations:

- 1) What effects do fogs have on shock waves?
- 2) What effects do fogs have on detonation waves?
- 3) What effects do fogs have on the transition from deflagration to detonation?

The effects of fogs on shock waves is important when a detonation starts in a region of detonable mixture of hydrogen:air:steam and passes into a region that may be flammable but is not detonable. There are some excellent references on this subject. In particular, Pierce<sup>(7)</sup> considers the effects of water spray on shock waves. The effect of the spray evaporation is to increase the pressure rise behind the wave initially, but to also increase the rate of pressure decay. It is possible that the fog will so reduce the shock wave intensity at the walls, that its presence will be an important safety aid. We are examining the pertinent references and theory to obtain quantitative results for typical examples in reactor containments. The theories may need extension to handle the dense droplet clouds under consideration.

There are several papers concerned with fuel drop detonations in which the fuel is vaporized by the initial shock wave and then burned to produce a detonation front, and one on the effect of inert dusts on detonations. These references and others will be examined to determine their relevance to the problem of detonation-wave interaction with water sprays. This problem has not been investigated as much as that of shock waves and sprays.

The effects of sprays on transition to detonation appear to be twofold: reduction in the thermal expansion of the burned region

because of lower temperature; and increase in the flame speed by inducing turbulence. The reduction in thermal expansion reduces the generation of shock waves leading to detonation by reducing fluid velocities. The increase in flame speed works oppositely. We will try to investigate the importance of these two opposing effects.

### 5.3.3 Halon Inerting

The use of Halons as chemical inhibitors of combustion has become widespread for industrial applications (8,9). Recently, we have begun an investigation into the possible use of Halon 1301 (monobromotrifluoromethane,  $CF_3Br$ ) to inert a  $H_2$ :air:steam atmosphere inside a nuclear reactor containment building. Our investigation is directed toward obtaining the answers to several questions regarding the use of Halon in nuclear power plants:

- Which Halon would be the best to use?
- How much Halon is required for inerting?
- What problems are associated with the use of Halon in general and for a nuclear reactor environment in particular?
- What procedures are required in order to return an inerted containment atmosphere to normal operating conditions?
- What are the costs associated with a Halon inerting system?

Fortunately, much of the groundwork of our investigation has been previously completed by E. T. McHale at the Atlantic Research Corporation. McHale directed a program entitled "Hydrogen Suppression Study and Testing of Halon 1301," that examined the use of Halon 1301 to inert nuclear reactor containments aboard naval vessels(10,11).

Our initial work will investigate Halon 1301 due to the extensive data that exist regarding its properties and characteristics. The combustion-inhibiting efficiency and favorable human toxicity levels of Halon 1301 have made it the dominant choice in industrial applications requiring "total flooding." A number of Halon 1301 fire extinguisher systems have been successfully employed(12,13) in applications involving volumes that are comparable to those of nuclear reactor containments (oil tanker engine rooms  $\sim 0.75 \times 10^6 \text{ ft}^3$ ).

The experimentally-determined value for the Halon 1301 concentration necessary to inert a dry  $H_2$ :air mixture (at 1 atmosphere and  $25^\circ\text{C}$ ) is 24 - 28 volume % (10,14). NFPA Standard 12A requires 31.4 volume % of Halon 1301 to suppress  $H_2$ :air combustion (this is a 10 - 20% safety margin). Studies(10) of the flammability limits of various  $H_2$ : $O_2$ : $N_2$ : $CF_3Br$  mixtures indicate that the peak concentration of  $CF_3Br$  required for inerting increases from 24 vol.% for air to approximately 75 vol.% when no nitrogen is present. Increased pressure (3 atm.) of the combustible mixtures required slightly higher  $CF_3Br$  concentrations; the presence of steam slightly decreased the  $CF_3Br$  concentrations; and increased temperature ( $49^\circ\text{C}$ ) had negligible effect. Detonation studies with  $H_2$ : $O_2$ : $CF_3Br$  mixtures indicate that  $CF_3Br$  concentrations well below

(~ 4 vol.% Halon) the inerting concentration\* will actually sensitize (lower the minimum ignition energy) the detonable mixture<sup>(15)</sup>.  $\text{CF}_3\text{Br}$  concentrations slightly below the inerting concentration will have no inhibiting effect<sup>(10,16)</sup>.

The proposal to use Halon 1301 to inert a reactor containment atmosphere requires that systems implications be examined. As indicated above, the  $\text{CF}_3\text{Br}$  must be injected in such a way that it mixes thoroughly with the air in order to avoid sensitizing the combustible mixture. The solubility of  $\text{CF}_3\text{Br}$  in water has been examined by McHale as a potential loss mechanism for  $\text{CF}_3\text{Br}$ . The effects appear to be tolerable (~ 5% loss) and a steady state is achieved. Radiolytic decomposition of  $\text{CF}_3\text{Br}$  in solution was also examined by McHale. An equilibrium condition is achieved with a tolerable loss of  $\text{CF}_3\text{Br}$  (~ 5%) but the solution becomes quite acidic (pH 2-3) if it is not buffered. While  $\text{CF}_3\text{Br}$  itself is essentially harmless to containment materials for extended periods of time, its decomposition products (radiolytic, thermal, and chemical) are not<sup>(17)</sup>. Questions regarding the effects of decomposition products and the treatment of inerted, post-accident containment gas are the thorniest for Halon inerting - our future efforts will concentrate on these areas.

Neglecting the cost of a post-accident gas treatment system, a Halon inerting system for nuclear reactor containments would cost 1-4 million dollars. This cost would include installation, Halon 1301, and electronic actuation components. While this cost figure is not firm, it is based upon rough scaling from existing large-volume fire extinguishing systems<sup>(12,13)</sup>.

#### 5.4 Combustion Analyses

During the course of our previous work<sup>(4)</sup>, it became evident that there was a lack of published work presenting results of theoretical thermodynamic calculations for hydrogen:air combustion over a range of initial temperatures and pressures, and with the addition of various inert diluents such as steam, liquid water, and carbon dioxide. For the hydrogen compendium<sup>(4)</sup> we developed a simple computer program, FLAME, to determine the final temperature and pressure expected from the complete, adiabatic, constant volume combustion of hydrogen:air:steam:liquid-water mixtures. The calculations included the effects of variable specific heats of the combustion gases by the use of accurate curve fits of molar internal energy versus temperature, but did not include the effects of dissociation of the combustion products. The neglect of dissociation is satisfactory at the lower temperatures generated by lean or rich hydrogen mixtures, but is not satisfactory at the high temperatures generated by the burning of near-stoichiometric mixtures.

We also developed a computer program which determines the temperature and pressure rise across a detonation wave in hydrogen:air:steam mixtures using the Chapman-Jouguet theory, as well as the temperature and pressure generated when the detonation wave is reflected normal to a rigid surface. The higher temperatures encountered required the inclusion of combustion-product dissociation. Using the same subroutines for computing equilibrium constants, enthalpies, and equilibrium mole fractions, we then constructed a computer code to compute adiabatic, constant-volume combustion including the effects of combustion-product dissociation. This work was extended to include the presence of carbon dioxide in the initial gas mixture, and CO and  $\text{CO}_2$  in the combustion

\*The concentration of Halon 1301 required to inert a mixture of  $\text{H}_2$ :air depends on the concentration of  $\text{H}_2$  and the concentration of  $\text{O}_2$ .

gases. The presence of liquid water in the initial mixture will also be included in the newer codes next quarter. Sections of the codes which computed equilibrium mole fractions and enthalpies were modified for use in the two dimensional Eulerian hydrodynamic code, CSQ<sup>(18)</sup>.

#### 5.4.1 Combustion Code Development

All the codes (except the earlier program FLAME) use linear interpolations of the latest versions of the JANAF (Joint Army-Navy-Air Force) thermochemical tables. Molar enthalpies and the logarithms of the equilibrium constants are given at every 100 K. Errors due to linear interpolation of these table values were found to be negligible.

All codes assume the initial and final gas mixtures obey the perfect gas law for mixtures:

$$pv = \frac{RT}{w} \quad (i)$$

where  $p$  is the absolute pressure,  $v$  is the mixture specific volume,  $R$  is the universal gas constant,  $T$  is the absolute temperature, and  $w$  is the average molecular weight. The accuracy of this assumption was tested by comparing the value of  $v$  for a given temperature, pressure, and composition with that obtained from a more accurate truncated virial equation of state. The differences were found to be negligible. For example, for initial mixtures with 13% steam, a temperature of 50°C (323 K), a pressure of about 1.5 atmospheres, and with variable amounts of hydrogen, the virial equation of state values of  $v$  were different from the perfect-gas-equation values by about 1 part in 10<sup>4</sup>.

The burned gas mixture is assumed to be in thermodynamic equilibrium. The presence of the following species is included: H<sub>2</sub>, N<sub>2</sub>, O<sub>2</sub>, H<sub>2</sub>O, O, OH, H, NO, N and A. For program CARBON, CO<sub>2</sub> and CO are also included. A check of the equilibrium composition using the commercial thermochemical program ACE<sup>(19)</sup> showed that the species neglected, such as HO<sub>2</sub> and NO<sub>2</sub>, were present in negligible amounts. The concentration of nitrogen atoms, N, was also found to be negligible, and it could have been neglected.

Dry air is assumed to be 20.946% oxygen, 78.117% nitrogen and 0.937% argon. In program CARBON, the presence of atmospheric CO<sub>2</sub> is separately considered instead of including it in the nitrogen percentage. The trace noble gas concentration is included in the argon percentage. In earlier versions of these programs dry air was simply assumed to be 21% oxygen and 79% nitrogen. The effects of using the more accurate air composition were found to be very small. Any of the programs can easily be modified to consider "air" as an arbitrary oxygen:nitrogen:argon mixture. This feature is useful for considering combustion of mixtures in which previous combustion or other processes have altered the composition.

The temperature and pressure expected after an adiabatic, constant-volume, complete combustion of a homogeneous hydrogen:air:steam mixture are computed using program DEFLAG. The results of program DEFLAG were found to be identical to that of the older program FLAME at the lower temperatures of lean hydrogen mixtures where dissociation is negligible. Near stoichiometric mixture ratios, the older program was found to considerably overestimate the temperature, by as much as 200 K, and to overestimate the pressure. Program CARBON is essentially identical to program DEFLAG except for the inclusion of carbon dioxide in the initial gas mixture and CO<sub>2</sub> and CO in the burned gases.

### Initial Conditions

Values for the following variables are required as initial conditions for the computation of the unburned gas mixture properties:

- 1) Temperature
- 2) Pressure
- 3) Hydrogen mole fraction
- 4) Steam mole fraction
- 5) Liquid water volume fraction

Program CARBON also requires

- 6) Carbon dioxide mole fraction

If the dry "air" is not standard in composition, then the mole fraction of the mixture must also be specified.

The large number of initial conditions makes it difficult to present results in a comprehensive way. Typically we have presented results as a function of hydrogen mole fraction for a given initial temperature, pressure, and steam (or steam-CO<sub>2</sub>) mole fraction.

### Method of Computation

The conditions for an adiabatic, constant-volume combustion are that the specific internal energy,  $u$ , and the specific volume,  $v$ , before and after the combustion are unchanged. The program therefore first computes the initial specific volume and internal energy:

$$w_1 = \sum w_i x_i \quad (2)$$

$$p_1 v_1 = RT_1 / w_1 \quad (3)$$

$$U_i(T_1) = H_i(T_1) - RT_1 \quad (4)$$

$$w_1 u_1 = \sum x_i U_i(T_1) \quad (5)$$

where the subscript 1 indicates the property is of the initial unburned gas mixture,  $w_i$  is the species molecular weight,  $x_i$  is the initial-mixture mole fraction of species  $i$ ,  $H_i(T_1)$  is the enthalpy per mole of species  $i$  at temperature  $T_1$ ,  $U_i$  is the internal energy per mole, and  $u_1$  the initial internal energy per unit mass.

The final specific volume and internal energy are computed by first supplying an initial guess for the final temperature and pressure. Given a temperature and pressure, subroutine MOLEFR computes the mole fractions by a method discussed in a later section. Given the estimate of the burned-gas mole fractions, the corresponding final value of  $v_2$  and  $u_2$  are determined by the use of equations analogous to Eqs. 2-5. At the estimated temperature, the pressure is varied until the final specific volume agrees with the initial specific volume to within a

close tolerance. For each pressure value considered, the mole fractions must be recomputed. Rapid convergence is achieved by use of linear extrapolation to find the root of the equation.

$$v_2(p_2) - v_1 = 0 \quad (6)$$

The temperature is then varied, each time requiring a new pressure variation, until the following equation is solved to within a close tolerance,

$$u_2(T_2) - u_1 = 0 \quad (7)$$

Again use is made of linear interpolation to find the root of Eq. 7. Note that the solution requires the convergence of three nested iterative loops. The innermost loop is the determination of the mole fractions for a given temperature and pressure. The middle loop is the determination of the pressure for a given temperature. The outermost loop is the determination of the temperature. Error messages are printed if any of the iterations fails to converge.

#### 5.4.2 Detonation Code Development

Program DETON computes the detonation velocity, pressure, and temperature, as well as the temperature and pressure after a normal reflection from a rigid surface. The program assumes the detonation travels at a speed corresponding to the Chapman-Jouguet condition. The insertion of initial conditions and the determination of the unburned gas properties are identical to that of the adiabatic, constant-volume combustion program DEFLAG, except that specific enthalpy,  $h_1$ , rather than specific internal energy,  $u_1$ , is required. Replacing the conditions in Eqs. 6 and 7 are the Hugoniot equation

$$h_2 - h_1 = (p_2 - p_1)(v_1 + v_2)/2 \quad (8)$$

and the condition at the Chapman-Jouguet point that the detonation velocity,  $V_1$ , is a minimum for a given detonable mixture:

$$V_1 = \text{minimum at C. J. point for given initial gas properties} \quad (9)$$

The detonation velocity and the burned-gas velocity are computed using

$$V_1 = v_1 \frac{(p_2 - p_1)^{1/2}}{(v_1 - v_2)} \quad (10)$$

$$V_2 = (v_2/v_1)V_1 \quad (11)$$



The solution proceeds by first guessing the final temperature and pressure. After computing the corresponding equilibrium mole fraction, average molecular weight, and specific volume and enthalpies, the values are entered into Eq. 8. The pressure is then varied, each time recomputing the mole fractions, until Eq. 8 is satisfied. This gives a point on the Hugoniot curve, but not necessarily the Chapman-Jouguet point. The temperature is then varied, each time recomputing the pressure and mole fractions, until the detonation speed is found to be a minimum. The pressure variation is done automatically, as in program DEFLAG, but the temperature variation has not yet been automated.

The solution process for the detonation again involves three nested iterative processes: determination of the mole fractions at given temperature and pressure, determination of pressure at given temperature, and the determination of the temperature. Failure of the inner two loops to converge is signalled by an error message.

A property of the Chapman-Jouguet point is that the flow of the burned gases behind the detonation is sonic (the Mach number is unity). In our formulation, the specific heats do not appear explicitly, and it would be difficult to compute a sonic speed of the burned gas mixture. Consequently, we have used another property of the C-J point; i.e., that at the Chapman-Jouguet point, we also have

$$\frac{(P_2 - P_1)}{(v_2 - v_1)} = dp/dv \quad (12)$$

Using a finite central difference approximation to the derivative at the C-J point, we found in several checks that our values of  $p_2$  and  $v_2$  were in excellent agreement with Eq. 12.

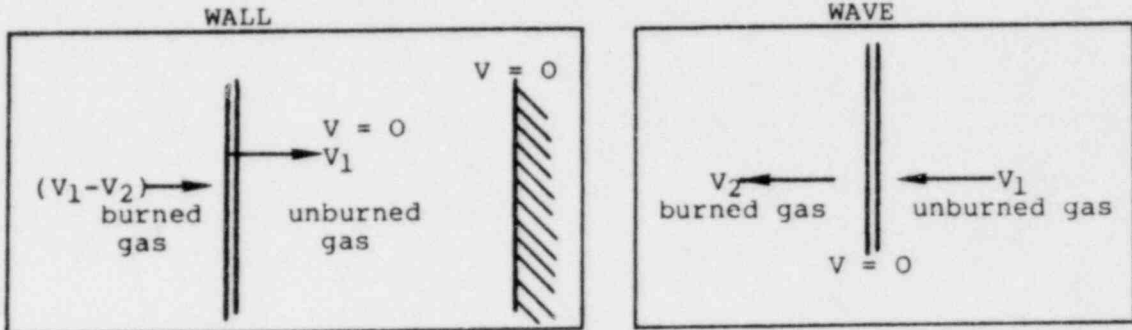
In a frame of reference fixed relative to the unburned gas, the burned gas behind the detonation wave is moving at a speed  $V_1 - V_2$ . When a detonation wave reflects normal to a rigid surface, the reflecting shock wave must bring the velocity of the burned gas to zero. The result is an increase in pressure by a factor  $\geq 2$ . The conditions after the reflection were determined by a process very similar to that for determining the detonation properties. An initial guess of the temperature and pressure after the reflection was varied until the Hugoniot equation, Eq. 8, was satisfied. In place of the Chapman-Jouguet condition, Eq. 9, we have the condition

$$V_1 - V_2 = V_3 - V_4 \quad (13)$$

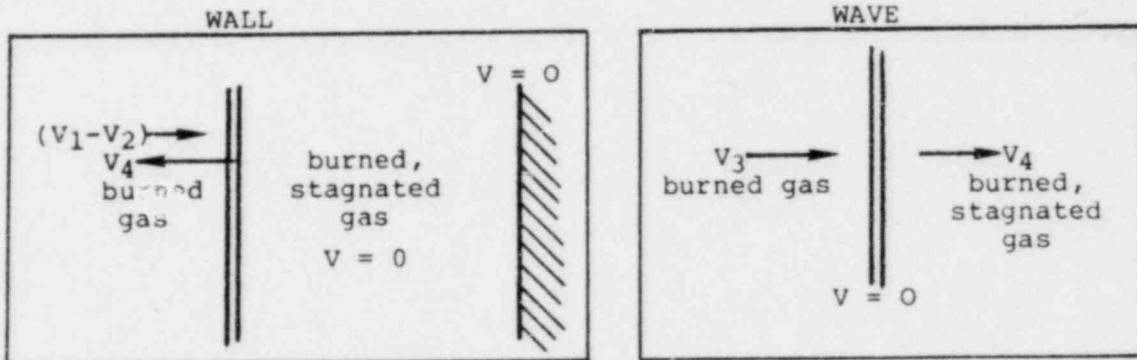
where  $V_3$  is the velocity of the burned gas relative to the reflected shock and  $V_4$  is the velocity of the reflected wave relative to the wall. The various velocities are shown in Fig. 5.3 with reference frames that are stationary relative to the wall and to the wave.

Shown in Figs. 5.4, 5.5, and 5.6 are results obtained from program DETON for the detonation properties at an initial temperature of 298 K, an initial pressure of 1 atmosphere, and 100% relative humidity (0.03128 mole fraction of steam). It is interesting that the peak pressure and temperature occur for mixtures a bit richer than stoichiometric, which is 28.6% hydrogen by volume.

FRAME OF REFERENCE STATIONARY RELATIVE TO



DETONATION WAVE APPROACHES THE WALL



REFLECTED SHOCK WAVE LEAVES THE WALL

Figure 5.3

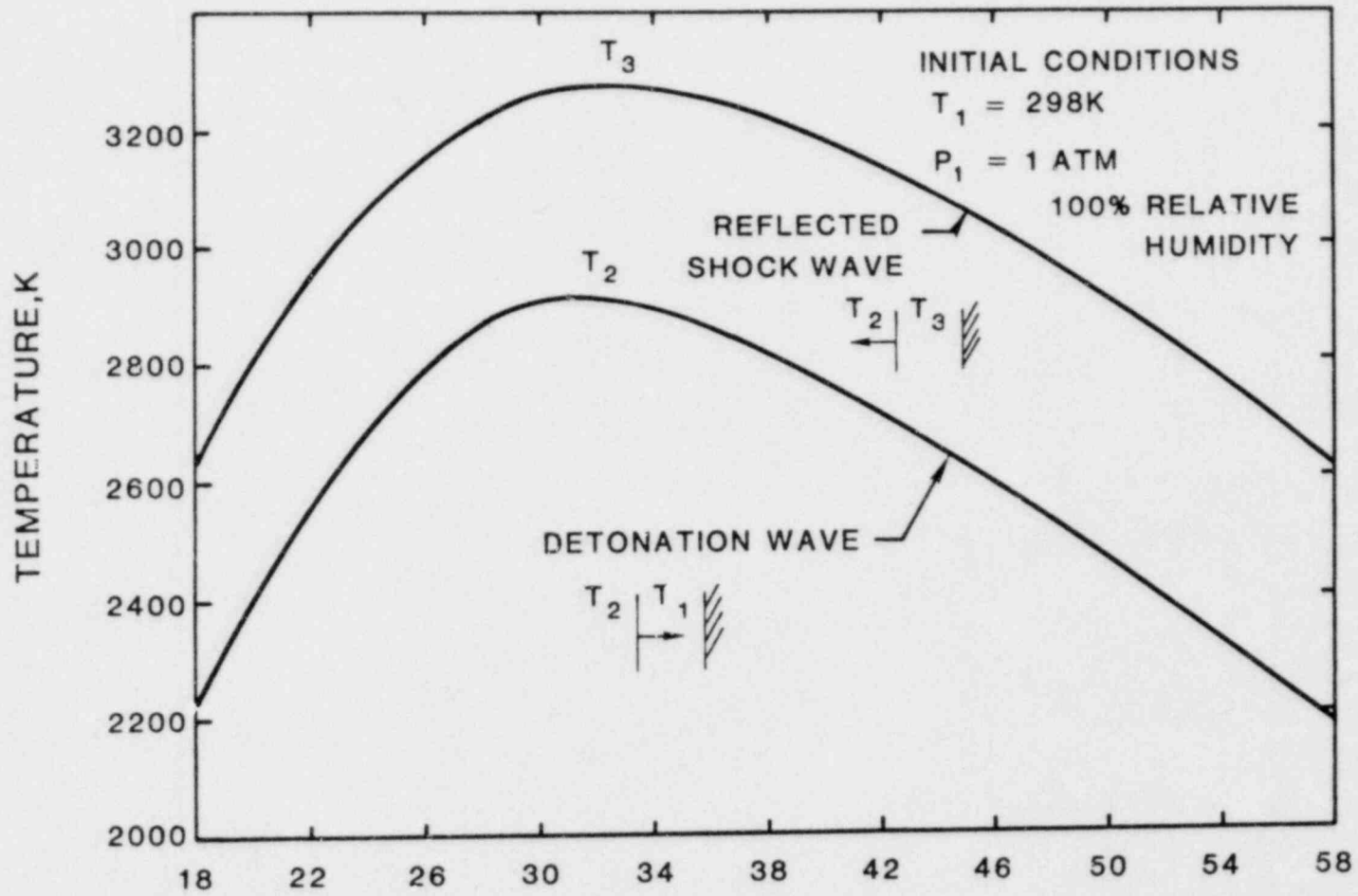


Figure 5.4. Theoretical Detonation Properties.

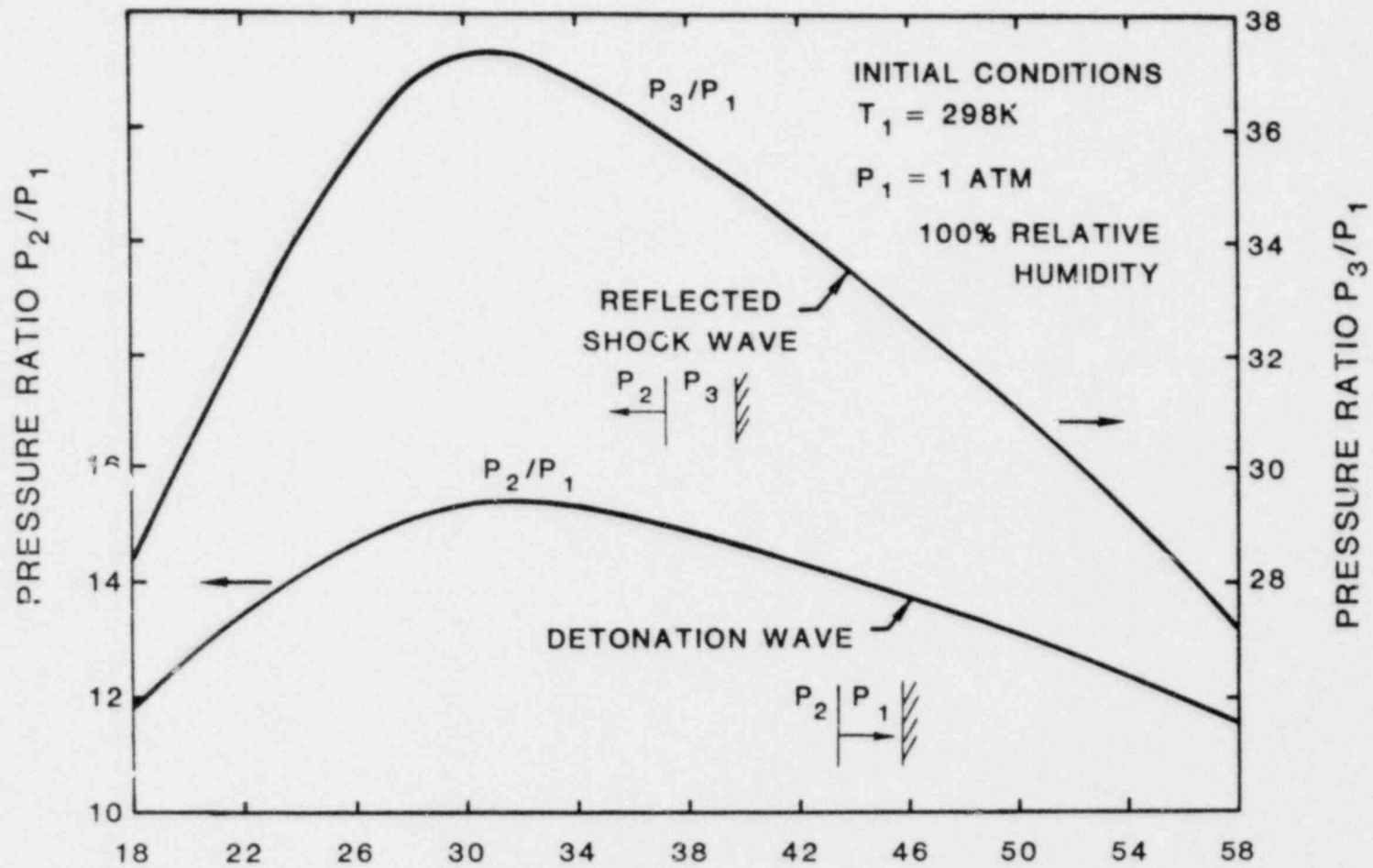


Figure 5.5. Theoretical Detonation Properties.

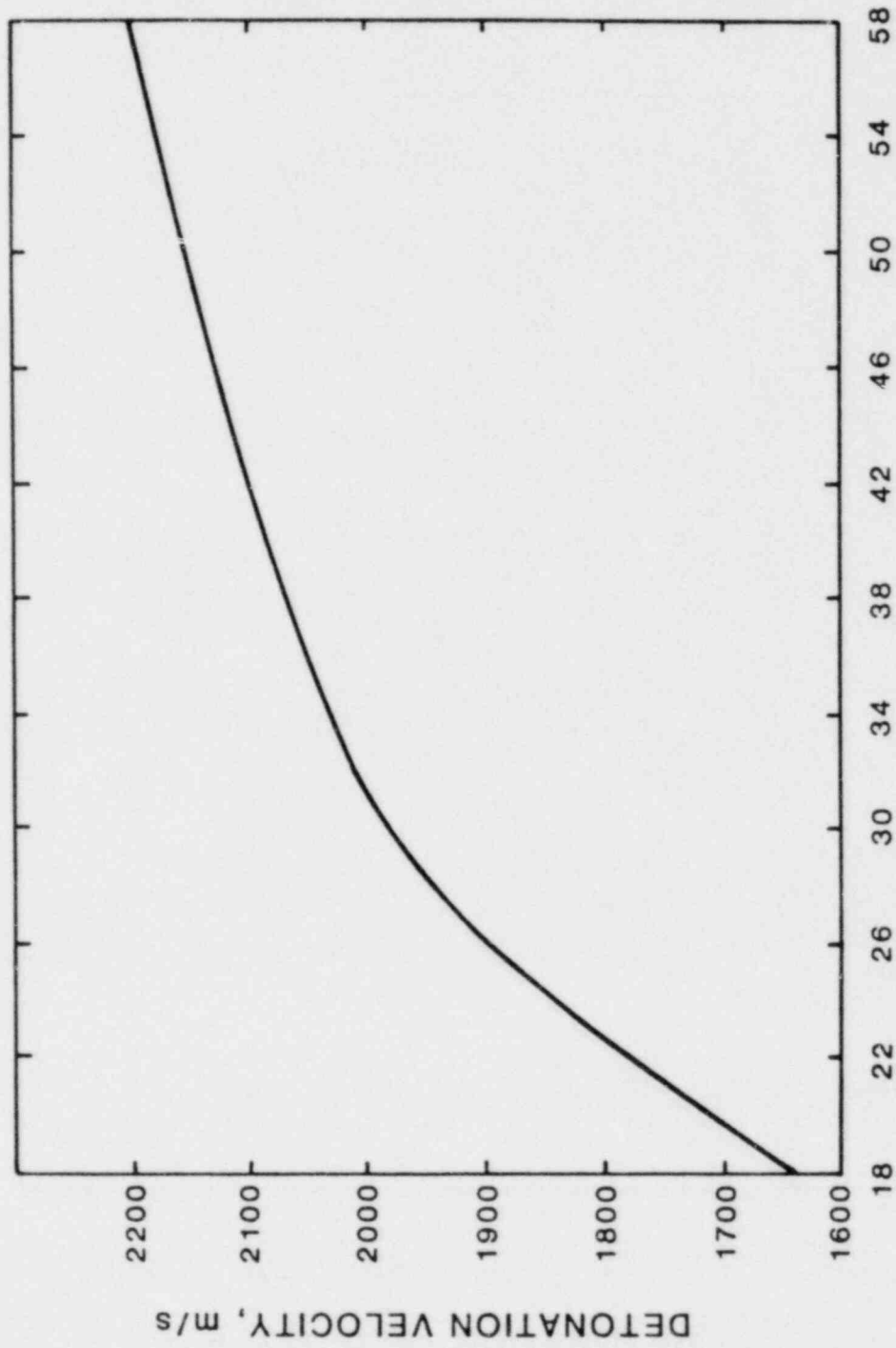


Figure 5.6. Theoretical Detonation Properties.

### Determination of the Combustion Gas Mole Fractions

The main computational difficulty in the computer programs is the determination of the burned-gas mole fractions. Ten simultaneous, non-linear, algebraic equations must be solved (twelve in program CARBON). The equations to be solved are shown below for program CARBON. Without any carbon, Eqs. 18 and 25 are not present. The equations involve the conservation of the hydrogen, nitrogen, oxygen, and carbon atoms and the seven equilibrium relations. The equilibrium constants, initial pressure, and initial (unburned gas) mole fractions are known. The unknowns are the eleven mole fractions of the burned gas species and the number of moles of burned gas per mole of unburned gas, here called  $X_{12}$ .

$$1 - (x_A)/X_{12} = X_{H_2} + X_{N_2} + X_{O_2} + X_{H_2O} + X_O + X_{OH} + X_H + X_{NO} + X_N + X_{CO_2} + X_{CO} \quad (14)$$

$$(2X_{H_2} + 2X_{H_2O} + X_{OH} + X_H)X_{12} = (2x_{H_2} + 2x_{H_2O}) \quad (15)$$

$$(2X_{N_2} + X_{NO} + X_N)X_{12} = (2x_{N_2}) \quad (16)$$

$$(2X_{O_2} + X_{H_2O} + X_O + X_{OH} + X_{NO} + 2X_{CO_2} + X_{CO})X_{12} = (2x_{O_2} + x_{H_2O}) \quad (17)$$

$$(X_{CO_2} + X_{CO})X_{12} = (x_{CO_2}) \quad (18)$$

$$K_1(T) = \frac{X_H^2 P}{X_{H_2}} \quad (19)$$

$$K_2(T) = \frac{X_O^2 P}{X_{O_2}} \quad (20)$$

$$K_3(T) = \frac{X_N^2 P}{X_{N_2}} \quad (21)$$

$$K_4(T) = \frac{X_H (X_{O_2} P)^{1/2}}{X_{H_2O}} \quad (22)$$

$$K_5(T) = \frac{X_{OH}(X_H P)^{1/2}}{X_{H_2O}} \quad (23)$$

$$K_6(T) = \frac{X_{NO}}{(X_{N_2} X_{O_2})^{1/2}} \quad (24)$$

$$K_7(T) = \frac{X_{CO}(X_O P)^{1/2}}{X_{CO_2}} \quad (25)$$

The  $X_i$  are the unknown mole fractions of the burned gas; the  $x_i$  are the known mole fractions of the unburned gas; the  $K_i(T)$  are the equilibrium constants which are known values for this computation at a given temperature.  $P$  is a nondimensionalized pressure equal to the actual pressure divided by one atmosphere.

Because each of the equations can be differentiated easily with respect to each of the unknowns, the Newton-Raphson method has been used to obtain accurate solutions. In the use of this method, the equations are recast in the form  $f_i(X_1, \dots, X_{12}) = 0$ . Let  $F$  be the vector of functions of  $f_i$ ,  $X$  be the vector of unknowns,  $A$  be the square matrix whose  $(i, j)$  element is the derivative of the  $i$ th equation with respect to the  $j$ th unknown, and let the superscript  $n$  refer to the  $n$ th iterative estimate of  $X$ . The Newton-Raphson method can then be expressed compactly in the form

$$-F = A \Delta X$$

$$X^{n+1} = X^n + \Delta X$$

This set of linear equations has been solved using the IMSL subroutine LEQTLF.

The Newton-Raphson method is quadratically convergent. Once the unknowns are reasonably well known, the method converges faster and faster. However, the method requires an initial first estimate of the unknowns. It has been found that if the estimate is not good enough the method either does not converge or does so slowly. The simplest way to get first estimates is to assume that the mole fractions of the main species ( $N_2$ ,  $O_2$ ,  $H_2O$  for lean mixtures and  $N_2$ ,  $H_2$ , and  $H_2O$  for rich mixtures) are given by the values for zero dissociation. The minor species are then computed from Eqs. 19-25 assuming these values of the main species. If we continue the perturbation analysis in terms of small dissociation constants, and place these values of minor species in Eqs. 14-18, we obtain improved values of the major species, which in turn are used to find a second estimate of the minor species. By the use of this method, starting values for the Newton-Raphson method have been found which give convergent results up to about 3400 K over an extremely wide range of pressure. At temperatures below 1100 K, the method is accurate enough in itself to not require the Newton-Raphson method for refinement of the unknown values. At very high temperatures

and low pressures the degree of dissociation is very large and the above procedure for finding starting values for the Newton-Raphson method is not adequate. The use of other expansions, assuming large dissociation, gives adequate starting values for the Newton-Raphson method.

#### 5.4.3 CSQ Detonation Calculations

A second calculation modelling hydrogen detonation in the Zion containment has been performed using CSQ<sup>(18)</sup> with the simple, two-ideal-gas model for the dry hydrogen:air mixture. The mixture in this calculation had a hydrogen mole fraction of 0.20, slightly above the detonability limit. This is richer than could be obtained from complete oxidation of the cladding in the core. However, other hydrogen sources (e.g., molten core-concrete interactions, zinc corrosion) may exist during the course of the accident.

The results of the calculation, carried out to 200 ms, were similar in character to those of the earlier one (Ref. 20), in which the hydrogen mole fraction was about 0.07. The load histories at various points on the wall were again complex, due to shock-wall and shock-shock interactions. For example, the interactions visible as high density regions in Figs. 5.7-5.9 produced a very high pressure spike at the center of the roof (Fig. 5.10). The earlier calculation had a peak pressure of about 60 Mdyne/cm<sup>2</sup> (60 bar). The pressure and the temperature histories show that the burned mixture was still not quiescent at the end of the calculation, but was oscillating near a state achievable by an isochoric burn.

Work has begun on developing a CSQ model for the Sequoyah containment building. We intend to approximate some of the details of internal structures, which was not done in the Zion and Indian Point calculations. We are currently seeking answers to several questions, concerning relative strengths of internal walls and flow paths between compartments.

The equations of state developed by M. Sherman for describing hydrogen:air:steam mixtures<sup>(21)</sup> have been used to construct tabular functions to be used in CSQ calculations. These material models will replace the simpler ones used previously, in which the burned and unburned mixtures were modelled as ideal gases. The earlier models also employed a threshold pressure and constant combustion rate to force detonation of the mixture.

### 5.5 Hydrogen Instrumentation

#### 5.5.1 Introduction

Our initial objective is to perform a survey of existing hydrogen- and oxygen-sensing equipment. Such equipment will be required to sample gaseous and liquid environments in the primary system and in containment. The equipment should quantitatively indicate the presence of hydrogen and oxygen before, during, and after reactor accident conditions. Subsequent objectives include:

- a) A performance and reliability evaluation of detection equipment currently installed in or planned for reactor plants.
- b) A determination and demonstration of optimum detector locations and characteristics.
- c) The development and testing of new plant instrumentation concepts, if necessary.



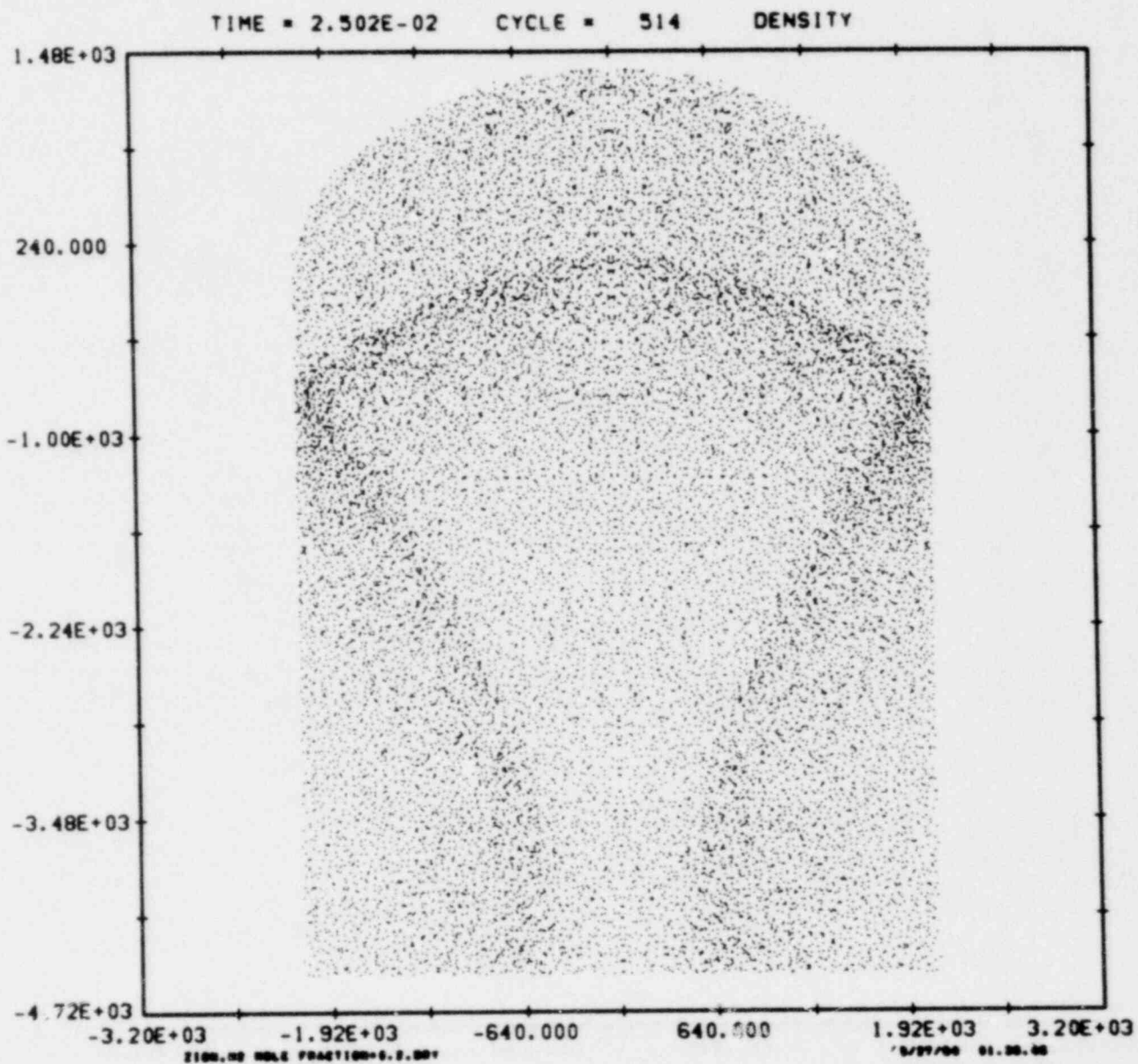


Figure 5.7 Density Field in Zion CSQ Calculation at 25 ms.

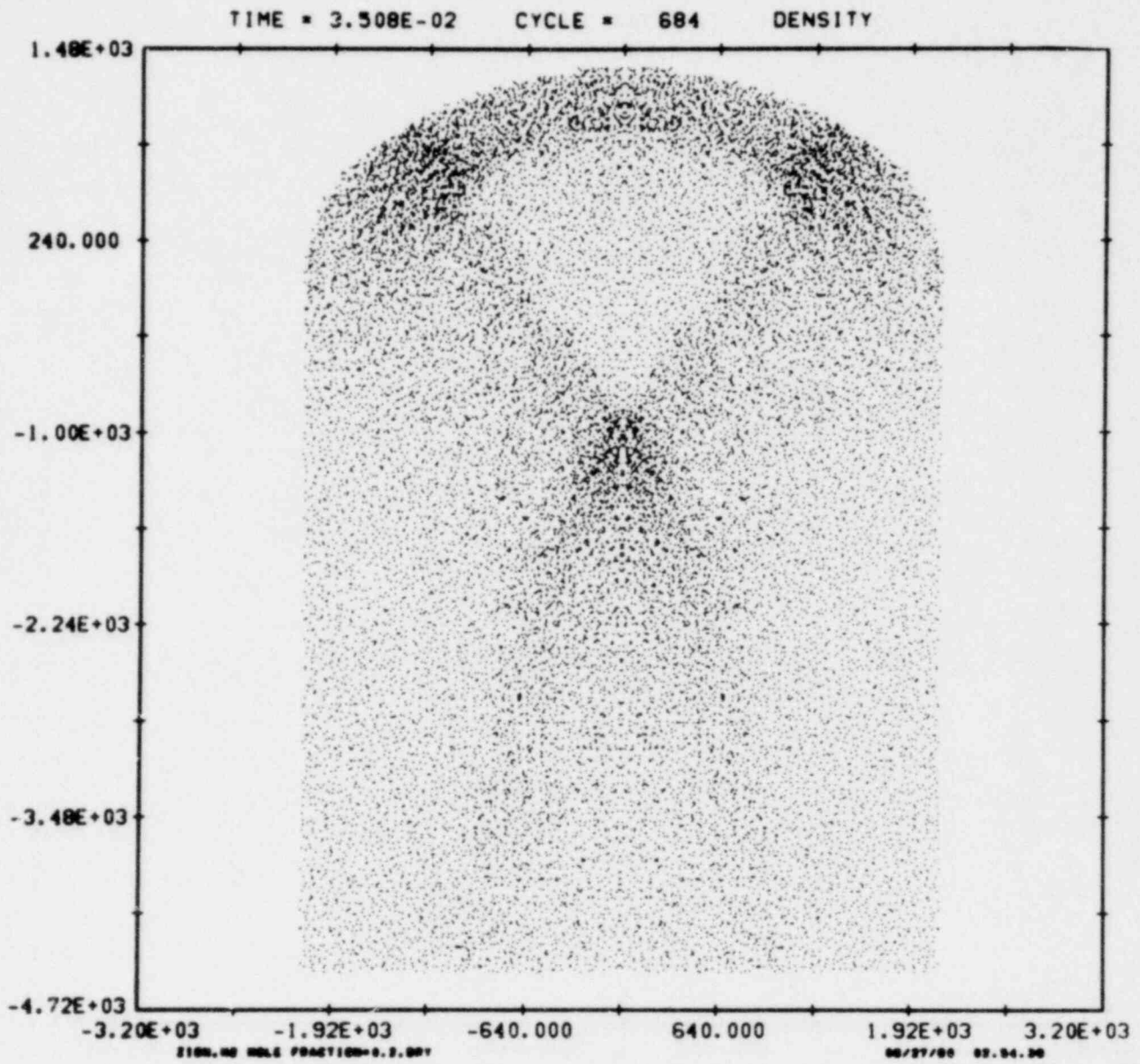


Figure 5.8 Density Field in Zion CSQ Calculation at 35 ms.

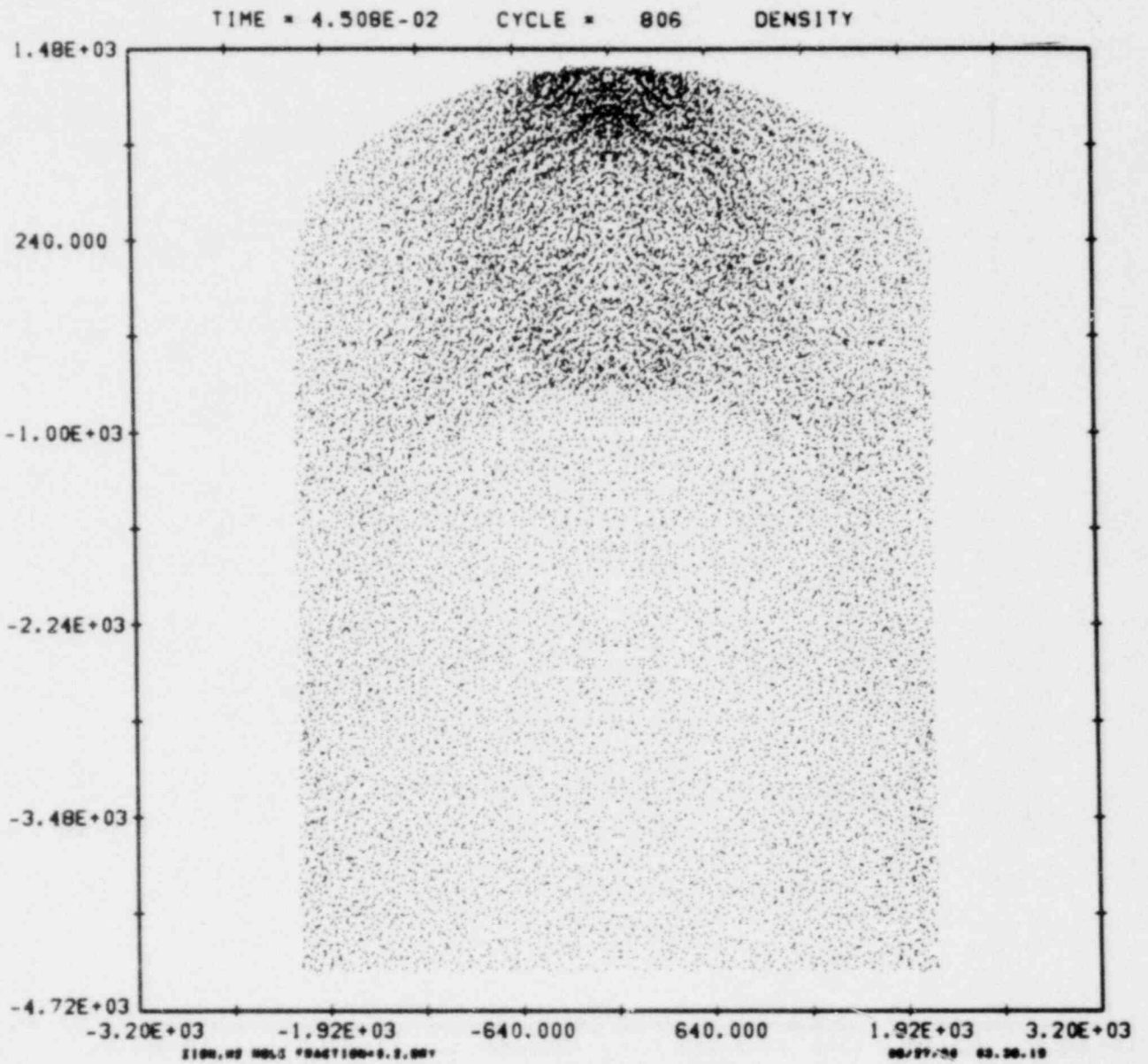


Figure 5.9 Density Field in Zion CSQ Calculation at 45 ms.

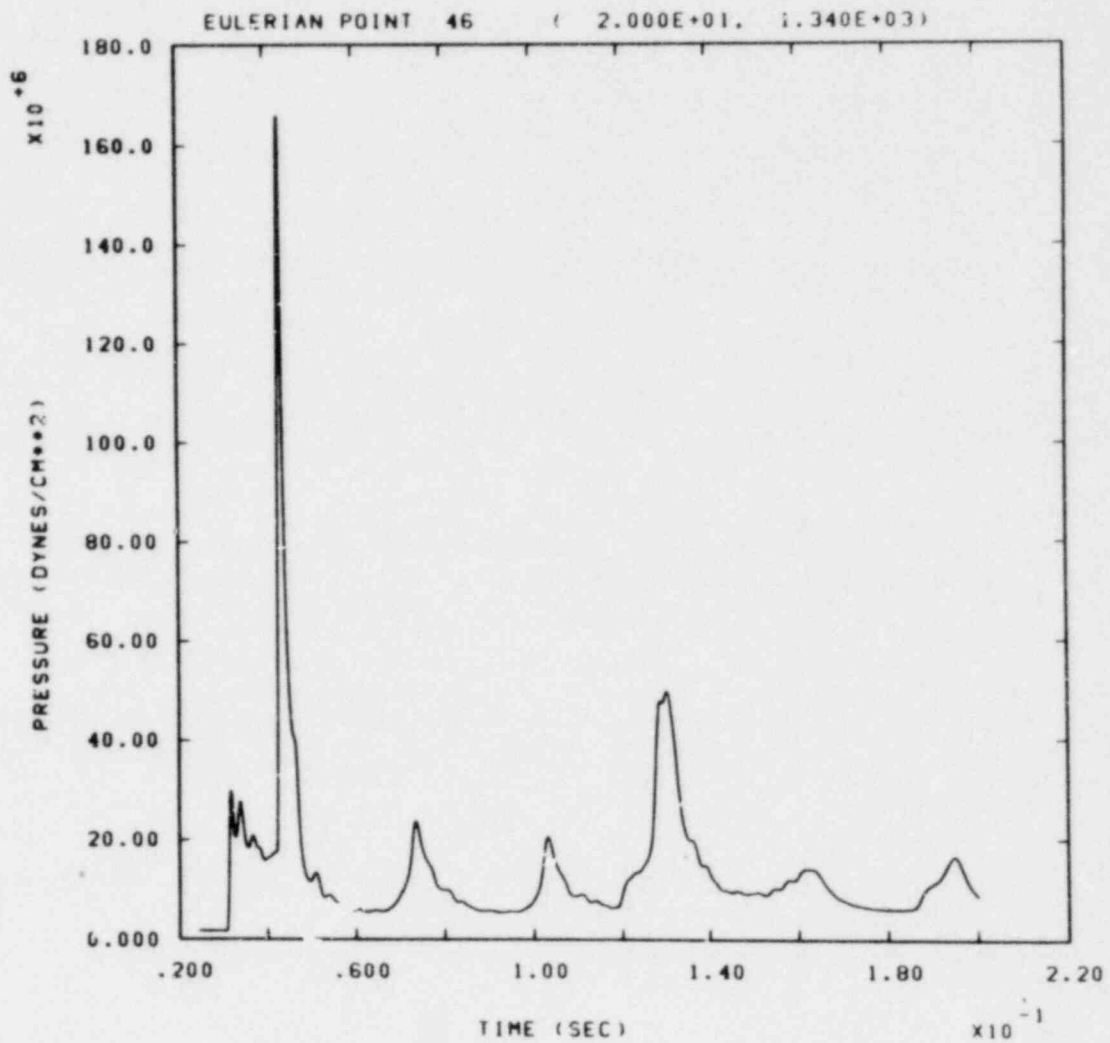


Figure 5.10 Pressure at center of Zion roof.

- d) The adaptation and development of supporting instrumentation for our experimental combustion program.

### 5.5.2 Gas Detection Equipment Suppliers

The following list identifies the fourteen suppliers who have been contacted thus far by telephone. Catalogs and/or descriptive literature have been received from each of them. A visit has been made to the facilities of the six indicated by an asterisk. The type of equipment manufactured is identified and will be further described below.

Bacharach Instrument Co. Mountain View, CA. David Knapp	Catalytic burning Wire resistance change
*Beckman Instruments, Inc. Fullerton, CA. Phillip Deming	Hot filament - Gas conductivity change Gas chromatograph
*Comsip, Inc. Delphi Div. South El Monte, CA Timothy Belke	Hot filament - Gas conductivity change
Control Instruments Corp. Fairfield, N. J. James Schaefer	Hot filament - Gas conductivity change
Enmet Corp. Ann Arbor, Michigan Elwood Boomus	Hot filament - Gas conductivity change Semiconductor type - Resistance change
*Exo Sensors, Inc. Laguna Hills, CA Fred Rudek	Diffusion - Partial pressure
*Gas Tech Inc. Mountain View, CA Robert Pellissier	Catalytic burning - Wire resistance change
General Monitors Costa Mesa, CA Bryan Bates	Catalytic burning - Wire resistance change
*Interscience Laboratory Palo Alto, CA S. M. Toy	Semiconductor type - Resistance change
*International Sensor Technology Santa Ana, CA Thomas McKerlie	Semiconductor type - Resistance change
Mine Safety Appliances, Co. Pittsburgh, PA Gene Rakoczy	Catalytic burning - Wire resistance change
Resource Systems, Inc. Hanover, N. J. Dr. Rubin	Thin film resistor - Resistance change

Scott Aviation  
Lancaster, NY  
Al Perry

Catalytic burning -  
Wire resistance change

Sentry Equipment  
Oconomowoc, WI  
Lloyd Eater

Gas chromatograph

Suppliers to be contacted next quarter include: Sentry Equipment and Teledyne. Users to be contacted include: Duke Power, TVA, and Con Edison.

### 5.5.3 Gas Detection Equipment

#### Catalytic burning - wire resistance change

A matched pair of catalyst-coated platinum wire sensors, isolated from each other, form two legs of a Wheatstone bridge circuit. The bridge is balanced when both sensors are exposed to a reference gas. The catalytic burning of the sample gas produces a change in electrical resistance of the sensor leg of the circuit. The unbalanced circuit quantitatively measures the presence of hydrogen.

#### Hot filament burning - gas conductivity change

Two pairs of heated filaments (commonly tungsten, platinum, or nickel), contained in cavities within a metal heat-conducting cell, act as two legs of a Wheatstone bridge. One contains a reference gas of known thermal conductivity; the other cavity contains the sample gas. A difference in the thermal conductivity of the two gases produces an unbalance in the bridge circuit quantitatively measuring the presence of hydrogen.

#### Gas chromatography

A packed column, or series of columns, is used to separate gases. A sample gas mixture is swept through the column by a carrier gas, typically helium. The column is packed with an absorbent material which retards each gas component for a unique period of time. As each gas component sequentially leaves the column, it is monitored by a detector which furnishes a signal to a recording potentiometer record. A series of peaks, one for each gas present, will be recorded. Hydrogen, the first gas to be discharged from the column, will be the first peak recorded. The quantity will be indicated by the height of the peak.

#### Diffusion - partial pressure

An electrochemical hydrogen sensor receives a continuous fresh gas sample at all times. The hydrogen in the sample diffuses through a solid polymer membrane over the sensing electrode and is immediately adsorbed onto the electrode surface. The rate of diffusion is proportional to the partial pressure of hydrogen. An electrical potential is applied internally between selected pairs of electrodes resulting in an active surface where hydrogen will readily give up electrons. The hydrogen gas becomes ionized and reacts with the counter electrode. The electric current thus generated is a direct measure of the partial pressure of hydrogen in the sample. Conversion of the partial pressure to volume percent is accomplished using a microprocessor.

#### Semiconductor type - resistance change

The sensor is a gas-sensitive semiconductor. The three suppliers of this type of sensor use different types of semiconductors. The types used are: mixed metallic oxides of iron, zinc, and tin; N-type sintered tin oxide; and metal-oxide silica. When hydrogen is adsorbed on the semiconductor surface, a marked decrease in electrical resistance occurs.

#### Thin-film resistor - resistance change

The detector consists of a high-resistance, thin-film resistor. In the presence of gases, gas molecules are adsorbed by the thin-film surface causing a change in the electrical resistance of the thin-film material. The change in resistance is spontaneous and permanent. The resistor will not return to its original resistance when the hydrogen is removed.

#### 5.5.4 Comments on Equipment

The following comments were gathered from conversations during visits and by telephone with both users and manufacturers of gas detection equipment and from manufacturer's catalogs and literature. Some of the comments are more or less private opinions and may not be supported by test results.

#### Hot filament and catalytic burning

The hot filament and the catalytic burning types of detectors are similar enough to be treated together.

Catalytic burning is the original and most widely used commercial hydrogen gas detection system. Comsip's Users List indicates that 79 units have been sold to 39 domestic plants and 14 units to 6 foreign nuclear plants. They also claim to be near satisfactory completion of a test procedure which would qualify their equipment for meeting the requirements of IEEE-323-1974 Standard for Qualifying Class 1E Equipment for Nuclear Power Generating Stations, as implemented by Regulatory Guide 1.89, Qualification of Class 1E Equipment for Nuclear Power Plants. During discussions with people responsible for hydrogen detection at Commonwealth Edison Co. (Chicago), T.V.A (Knoxville), and the Nuclear Safety Analysis Center (EPRI; Palo Alto), we were told that: the hot filament type hydrogen sensors are breakdown prone and require significant maintenance; present equipment is primitive and not very good; and that equipment now on the market is inadequate.

A competitor described the system as being reliable enough in a stable environment, like that of an office or a laboratory, unless it gets wet. The equipment is sensitive to moisture, is difficult to set up because of varying sample conditions, and changes in humidity cause reading errors. Comsip claims that the system is not sensitive to steam, that after removing the liquid water from the incoming sample, the sample is heated to 270°F before it reaches the 500°F filament.

Other criticisms included a likelihood of filament burnout in a high hydrogen concentration and/or an oxygen deficiency, and sensor vulnerability to poisoning by silicones and halogen compounds. The Comsip literature states that additional oxygen can be added ahead of the analyzer when sufficient oxygen is not present. Similarly, for oxygen measurement, additional hydrogen can be added to complete the reaction of all the oxygen present.

## Gas chromatography

A gas chromatograph is an analytical instrument which is more likely to be found in a laboratory than in reactors. However, Commonwealth Edison Co. (CECo) is using a Bendix gas chromatograph in a Sentry System as a backup to their Comsip installation in some, but not all, locations. Equipment cost was given as the reason for the limited use.

Although the chromatograph is accurate and reliable, its response time between successive readings may be very long (minutes). During a LOCA, continuous readings or readings in rapid succession will be required.

## Diffusion

The diffusion system is described as a space-age spinoff developed by General Electric for space capsule monitoring. The system for containment application is under development by a new company whose president is one of the original GE developers. The design apparently was not patented by GE. The developer says the system uniquely fulfills the NRC Regulation Guide 1.97 requirement, "... accident monitoring instrumentation inputs should be from sensors that directly measure the desired variables", in this case, hydrogen partial pressure. The sensors are mounted within containment and are designed to survive LOCA environments.

CECo people noted that the sensors are designed to be replaced at refueling times but require a two-hour recalibration after a 27°F temperature change. In November 1979, GE stated that the sensor response is significantly slower than that observed in June 1979, and that there is significant data scatter which makes the reliability questionable. The CECo people did not observe a variation in time response nor degradation of sensor performance with time as seen by GE. At the 4% hydrogen level, however, the needle response was unstable even though the gas percentage was known to be stable. CECo says that GE abandoned work on the sensor after a staff of their best people was unable to obtain satisfactory operation. The supplier claims that GE abandoned the project because it was not likely to be sufficiently profitable.

## Semiconductor

The semiconductor sensor is probably the least expensive type available. It is very sensitive and a demonstration in the low ppm range was witnessed. It is not certain if high gas concentrations can be accurately measured. Radiation vulnerability may also be a problem.

The supplier with apparently the most successful system has no desire to do business with the nuclear industry because of the paperwork, regulations, qualification testing, and small market potential.

## Thin-film resistor

The manufacturer readily agreed that this type of detector would be unsuitable for reactor use since the sensor will not return to its original resistance after a measurement has been made. The sensor must be replaced when it has reached the desired, initial detection level.



## 5.6 References

1. A. L. Furno, E. B. Cook, J. M. Kuchta and D. S. Burgess, "Some Observations on Near-Limit Flames," 13 Sym. on Comb., (Pittsburg, Comb. Inst., 593-599, 1971).
2. B. C. Slifer and T. G. Peterson, "Hydrogen Flammability and Burning Characteristic in BWR Containments," NEDO-10812, 73NED49, General Electric (April, 1973).
3. W. C. Harrison, H. Tamm, R. MacFarlane, L. J. Clegg, "Canadian Hydrogen Combustion Studies Related to Nuclear Reactor Safety Assessment," 1980 Western States Section Meeting of Combustion Institute Oc. 1980, Los Angeles, CA.
4. M. P. Sherman, M. Berman, J. C. Cummings, G. W. Perkins, D. A. Powers, P. O. Bieniarz, and O. R. Green, "The Behavior of Hydrogen During Accidents in Light Water Reactors," NUREG/CR-1561, SAND80-1495 (August 1980).
5. B. Lewis and G. von Elbe, Combustion, Flames and Explosions of Gases, 2nd, Ed., (New York: Academic Press, 1961).
6. H. Hiroyasu and T. Kadota, Trans. Japan S.M.E. 40, 3147 (1974).
7. T. H. Pierce, "Blast-wave propagation in a spray," J. Fluid Mech. 88, 641-657 (1978).
8. C. L. Ford, "Halon 1301 Update: Research, Application, New Standard," Specifying Engineer (May 1977).
9. Anonymous, "Fluoro-carbons Find new Fires to Fight," Chemical Week, 44-45 (March 12, 1980).
10. E. T. McHale, "Hydrogen Suppression Study and Testing of Halon 1301: Phases I and II," Atlantic Research Corporation report No. ARC 47-5647 (December, 1976); Maritime Administration, U. S. Department of Commerce, contract RT-3900.
11. E. T. McHale, "Hydrogen Suppression Study and Testing of Halon 1301: Phase III," Atlantic Research Corporation report No. ARC 47-5702 (March 1978); Maritime Administration, U. S. Department of Commerce, contract T-38169.
12. D. Plunkett, Ansul Co., Marinette, Wisconsin, private communication (October, 1980).
13. B. L. Warner, Kidde Belleville, Belleville, New Jersey, private communication (Sept.-Oct., 1980).
14. S. N. Bajpai and J. P. Wagner, Ind. Eng. Chem., Prod. Res. Dev. 14, 54-59 (1975).
15. A. Macek, AIAA Journal 1, 1915-1918 (1963).
16. A. L. Johnson, A. L. Furno, and J. M. Kuchta, "Infrared Spectral Radiances and Explosion Properties of Inhibited Methane-Air Flames," Bu Mines RI 8246 (1977).

References continued

17. E. I. du Pont de Nemours and Co., "Du Pont Halon 1301 Fire Extinguishant," Report No. B-29D (1977).
18. S. L. Thompson, CSQII - An Eulerian Finite Difference Program for Two-Dimensional Material Response - Part 1. Material Sections, SAND77-1339, Sandia Laboratories, Albuquerque, NM, January 1979.
19. C. A. Powars and R. M. Kendall, "User's Manual Aerotherm Chemical Equilibrium (ACE) Computer Program," Aerotherm Corp., Mountain View, CA (May 1969).
20. W. B. Murfin (Ed.), Report of the Zion/Indian Point Study: Volume 1, NUREG/CR-1410, SAND80-0617/1, Sandia National Laboratories, Albuquerque, NM, August 1980.
21. M. Sherman, Sandia National Laboratories, private communication.

## 6. Combustible Gas in Containment Program

(V. M. Loyola, J. C. Cummings)

### 6.1 Summary

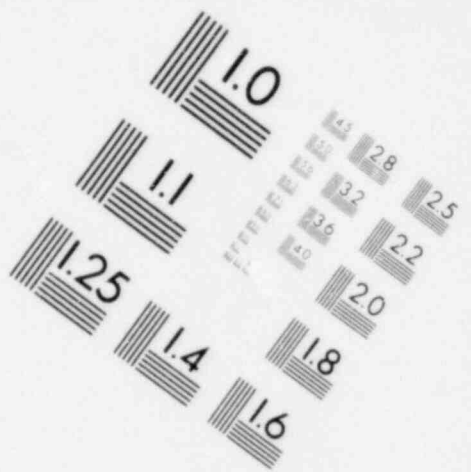
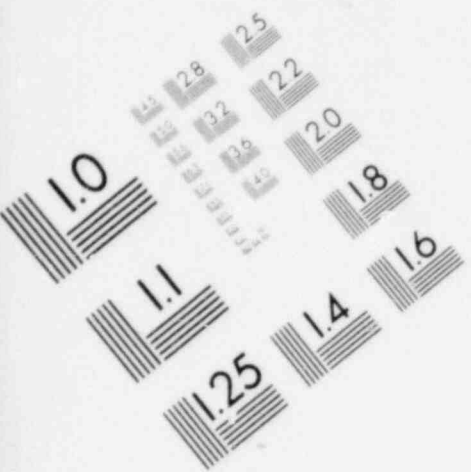
This program will study the generation of H<sub>2</sub> from the corrosion of zinc (both in galvanized steel and in zinc-based paints) and other materials located within light water reactor containment buildings. The program has two major objectives:

- (1) To determine the amounts of zinc, in both galvanized steel and zinc-bearing paints/primers, and other corrodible materials which are present in representative LWR containment buildings.
- (2) To determine the rates at which H<sub>2</sub> is generated from the corrosion of those materials in post-LOCA environments.

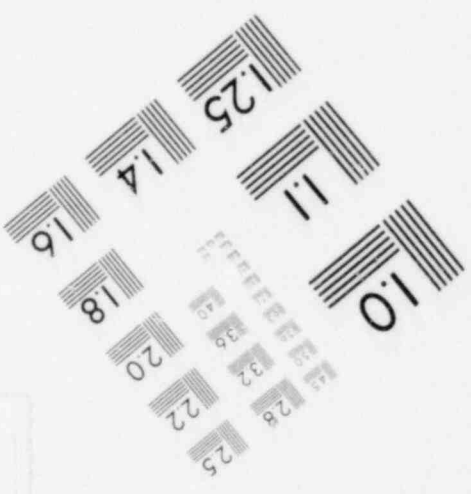
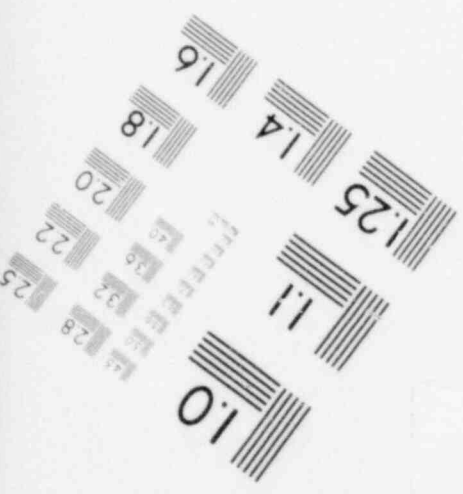
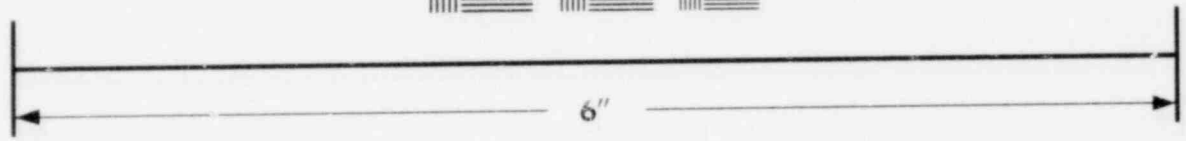
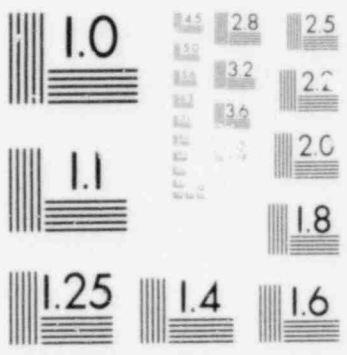
### 6.2 Zinc Inventory Investigation

Zinc inventories are being determined for both PWR and BWR nuclear power plants. The information is being extracted from the PSAR's and/or the FSAR's for each of the plants. The data thus far obtained are shown in Table 6.1 with total zinc inventories divided into quantities found in coatings (primers) and quantities found as galvanized steel, including the area (in square feet) over which each is spread. Some difficulties have been encountered, however, in collecting the required information. For example, Table 6.1 shows that in some cases no inventory of galvanized steel was located. Also, the data tabulated are primarily for power plants which have scheduled licensing dates some time in the future. Only one, Fort Calhoun I, is a pre-1975 plant; apparently information pertaining to the inventory of galvanized materials was not necessarily required prior to that time. The scarcity of data for BWR plants in Table 6.1 reflects the difficulty which we have encountered in obtaining data for that type of power plant. Some of the difficulties may be alleviated by requesting the pertinent information directly from either the Architect/Engineering firm or the utility associated with each power plant. Contacts have already been established with representatives of both Bechtel Corporation and Stone and Webster Engineering Corporation. These companies are in the process of making some information available to us and contacts with other engineering firms will also be sought.

It has become apparent, even from the limited amount of data found in Table 6.1, that establishing an "average" zinc inventory for a representative LWR containment may be a futile effort. The zinc inventories vary so greatly from plant to plant that any "average" becomes meaningless. It appears, therefore, that it will be prudent to determine zinc inventories specific to a few power plants.



**IMAGE EVALUATION  
TEST TARGET (MT-3)**



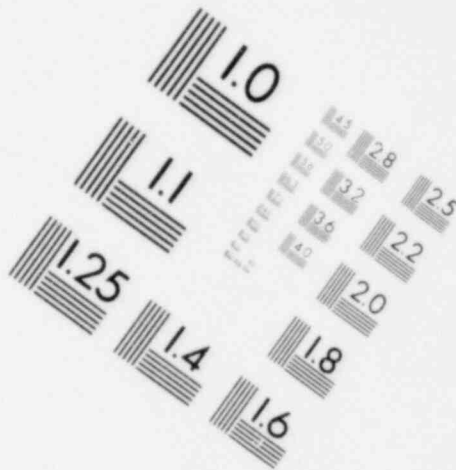
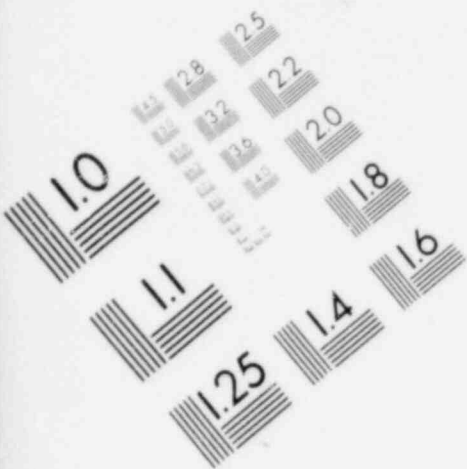


IMAGE EVALUATION  
TEST TARGET (MT-3)

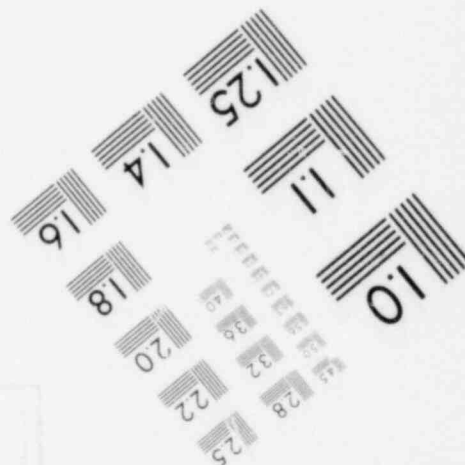
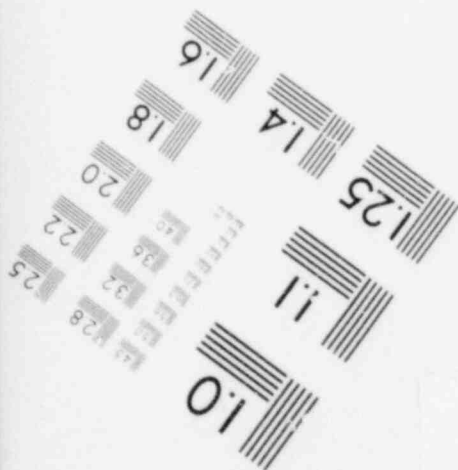
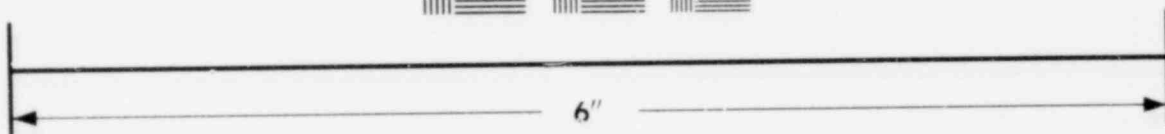
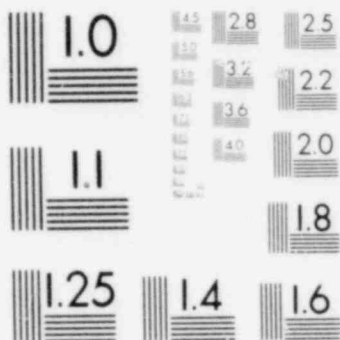


Table 6.1

## Inventory of Zinc in Several LWR Power Plant Containments

Power Plant	Type	Zinc Coating (Primer)		Zinc (Galvanized)		Total Zinc		Source of Information
		Area (ft <sup>2</sup> )	Amount (lbs)	Area (ft <sup>2</sup> )	Amount (lbs)	Area (ft <sup>2</sup> )	Amount (lbs)	
Beaver Valley 2	PWR	73,300	2,000*	60,000*	5,569*	133,300	7,569	PSAR Table 14.3-8.9
Davis-Besse 1	PWR	167,057	15,823	No data located				FSAR Table 6-1
Erie 1 & 2	PWR	187,221	20,875*	No galvanized steel or Zn alloy used inside R.B.*		187,221	20,875	OEC PSAR p.6.1-6 OEC PSAR Am. 3 p.6.2-54 PSAR Table 14.16-2
Fort Calhoun 1	PWR	16,600	1,578	No data located				PSAR Table 14.16-2
North Anna 1 & 2	PWR	74,412	7,048	No data located				FSAR Table 6.2.1.1-5
Pilgrim 2	PWR	193,000*	18,500*	51,000*	7,250*	244,000	25,750	PSAR Table 6.2-23, reproduced in Bechtel report (Job 8791), 5-80. FSAR Table 6.2-33
San Onofre 2 & 3	PWR	6,700*	850*	137,971*	15,601*	144,671	16,451	FSAR Table 6.2-33
Sequoyah 1	PWR	104,495	9,897	No data located				Referred to Watts Bar FSAR, data from Tables 6.2.1-34, 35, 36. FSAR, pp.3.8-21, 3.8-32, 6.2-18
Three Mile Island 2	PWR	No Zn based primers*		Used in R.B., but no data on amount located				FSAR Table 6.2.1-1, p.15.4-2
Watts Bar 1 & 2	PWR	84,831	5,358**	Used in R.B., but no data on amount located				FSAR Table 6.2.1-1, p.15.4-2
Yellow Creek	PWR	363,789	34,457	No data located				
Brunswick 1 & 2	BWR	No data found in FSAR, referred to Dresden 3 PSAR, Amendment.						
Dresden 3	BWR	No data found in PSAR, Amendment 23.						
Nine Mile Point 2	BWR	No data found in PSAR.						

\*Data obtained directly from Safety Analysis Report; otherwise data calculated assuming 0.003" Dry Film Thickness of Primer coat.

\*\*Calculated using a 0.002" DFT for primer coat, CarboZinc 11, 85% Zinc by weight.

### 6.3 Study of Hydrogen Generation Rates

The second objective of the program is to measure the rates of H<sub>2</sub> generation from zinc in both galvanized steel and coatings. There are two distinct parts to this task. The first part calls for a review of the pertinent regulatory basis for the experiments and for a review of the literature since BNL-NUREG-24532 relevant to these studies. The first part is essentially complete, the regulatory documents found to be most useful were the following reports from the American National Standards Institute: ANSI N101.2 - 1972, ANSI N101.4 - 1972, and ANSI NS12 - 1974. These documents, however, deal only with coatings (paint/primers) and do not address galvanized steels for the nuclear industry. Documents concerning galvanized steels are now being sought. The documents concerned with coatings do establish some criteria for the testing of such coatings, criteria such as minimum size of coated specimens to be tested, preparation of the test specimens, and specifications to be met by deionized water used for testing.

The review of the literature since BNL-NUREG-24532 indicates that most of the research dealing with corrosion of galvanized steel and/or zinc in other forms is to be found in foreign journals in the language of the country of origin (primarily German, French, and Japanese). Consequently, the literature search has been slowed due to the time required to obtain translations.

The second part of this task is presently being planned. A program for the experimentation is being set up to meet the needs and requirements of the NRC. A preliminary review has been held, but final program approval has not been obtained yet. In conjunction with this aspect of the program, a steam generator/reactor vessel is being designed to allow the actual experiments to be carried out; this design has also been reviewed, but the final design has not been submitted to the NRC for approval.

DISTRIBUTION:

US NRC Distribution Contractor (CDSI) (400 copies for R3)  
7300 Pearl Street  
Bethesda, MD 20014

US Nuclear Regulatory Commission (10)  
Office of Nuclear Regulatory Research  
Washington, DC 20555

Attn: R. DiSalvo  
S. Fabic  
D. A. Hoatson  
C. E. Johnson  
C. M. Kelber  
A. W. Serkiz  
R. R. Sherry  
M. Silberberg  
L. H. Sullivan  
L. S. Tong

US Nuclear Regulatory Commission (9)  
Division of Systems Safety  
Office of Nuclear Reactor Regulation  
Washington, DC 20555

Attn: T. P. Speis  
J. F. Meyer  
N. Lauben  
J. K. Long  
A. R. Marchese  
W. R. Butler  
C. G. Tinkler  
Z. Rosztoczy  
V. Benaroya

US Department of Energy  
Operational Safety Division  
Albuquerque Operations Office  
P. O. Box 5400  
Albuquerque, NM 87185  
Attn: J. R. Roeder, Director

Kraftwerk Union (2)  
Hammerbacher strasse 12 & 14  
Postfach 3220  
D-8520 Erlangen 2  
Federal Republic of Germany  
Attn: Dr. M. Peehs  
Dr. K. Hassman

Kernforschungszentrum Karlsruhe (2)  
Postfach 3640  
75 Karlsruhe  
Federal Republic of Germany  
Attn: Dr. J. P. Hosemann  
Dr. S. Hagen

Dr. H. Karwat  
Technische Universitaet Muenchen  
D-8046 Garching  
Federal Republic of Germany

A. Morici  
CNEN NUCLIT  
Rome, Italy

AEC, Ltd. (2)  
Whiteshell Nuclear Research  
Establishment  
Pinawa, Manitoba, Canada  
Attn: H. Tamm  
D. Liu

Prof. F. Mayinger  
Technische Universitaet Hannover  
3000 Hannover 1  
Federal Republic of Germany

Dr. M. V. Banaschik  
Gesellschaft für Reakforsicher-  
heit (GRS)  
Postfach 101650  
Glockengasse 2  
5000 Koeln 1  
Federal Republic of Germany

Swedish State Power Board (2)  
El-Och Vaermeteknik  
Sweden  
Attn: Eric Ahlstroem  
Wiktor Frid

M. El-Genk  
EG&G - Idaho, Inc.  
P. O. Box 1625  
Idaho Falls, ID 83401

R. A. Bari (2)  
Brookhaven National Laboratory  
Upton, New York 11973

M. L. Stevenson  
Los Alamos National Laboratory  
P. O. Box 1663  
Los Alamos, NM 87545



Electric Power Research Inst. (3)  
3412 Hillview Avenue  
Palo Alto, CA 94303  
Attn: G. Thomas  
L. B. Thompson  
K. A. Nilsson

Offshore Power System (2)  
8000 Arlington Expressway  
Box 8000  
Jacksonville, FL 32211  
Attn: D. H. Walker  
G. M. Fuls

Westinghouse Corporation (2)  
P. O. Box 355  
Pittsburgh, PA 15230  
Attn: L. Hochreiter  
J. Olhoeft

Argonne National Laboratory (2)  
9700 S. Cass Avenue  
Argonne, IL 60439  
Attn: C. H. Bowers  
Dae Cho

Cathy Anderson  
Nuclear Safety Oversight Comm.  
1133 15th St., NW  
Room 307  
Washington, DC 20005

P. Cybulskis  
Battelle Columbus Laboratory  
505 King Avenue  
Columbus, OH 43201

Wang Lau  
TVA  
400 Commerce, W9C157-CK  
Knoxville, TN 37902

J. E. Antill  
Berkeley Nuclear Laboratory  
Berkeley GL 139PB  
Gloucestershire  
United Kingdom

Prof. S. Abdul-Kalik  
Nuclear Engineering Department  
University of Wisconsin  
Madison, WI 53706

M. N. Fardis  
Massachusetts Inst. of Technology  
Rm. 1-276  
Cambridge, MASS 02139

H. J. Teague  
UKAEA Safety & Reliability Dir.  
Wigshaw Lane, Culcheth  
Warrington WA34NE  
Cheshire, England

B. R. Bowman  
Lawrence Livermore Nat'l Laboratory  
L-140  
P. O. Box 808  
Livermore, CA 94550

Gesellschaft fur Reaktorsicherheit  
(GRS mbH) (2)  
8046 Garching  
Federal Republic of Germany  
Attn: E. F. Hicken  
H. L. Jahn

R. Tosetti  
Bechtel Power Corp.  
P. O. Box 3965  
San Francisco, CA 94119

B. Tolley  
Dir. of Res., Sc. & Ed.  
CEC  
RueDeLaLoi 200  
1049 Brussels  
Belgium

S. G. Bankoff  
Chemical Engineering Dept.  
Northwestern University  
Evanston, IL 60201

DISTRIBUTION (Cont'd):

1223 R. R. Prairie  
 2510 D. H. Anderson  
 2513 J. E. Kennedy  
 2514 D. E. Mitchell  
 4000 A. Narath  
 4400 A. W. Snyder  
 4410 D. J. McCloskey  
 4412 J. W. Hickman  
 4414 G. B. Varnado  
 4414 A. S. Benjamin  
 4414 W. B. Murfin  
 4420 J. V. Walker  
 4421 R. L. Coats  
 4422 D. A. Powers  
 4422 R. M. Elrick  
 4424 W. Breitung  
 4424 M. A. Clauser  
 4425 Frank Briscoe  
 4425 W. J. Camp  
 4440 G. R. Otey (2)  
 4441 M. Berman (20)  
 4441 R. K. Cole, Jr.  
 4441 M. L. Corradini  
 4441 J. C. Cummings  
 4441 J. F. Muir  
 4441 M. P. Sherman  
 4441 G. G. Weigand  
 4442 W. A. Von Rieseemann  
 4443 D. A. Dahlgren  
 4444 S. L. Thompson  
 4444 L. D. Buxton  
 4444 R. K. Byers  
 4445 L. O. Cropp  
 4450 J. A. Reuscher  
 5131 B. Morosin  
 5131 W. B. Benedick  
 5512 D. W. Larson  
 5520 T. B. Lane  
 5521 L. W. Davison  
 5530 W. Herrmann  
 5534 J. F. Assay  
 5534 D. S. Drumheller  
 5836 J. L. Ledman  
 5836 L. S. Nelson  
 5846 E. K. Beauchamp  
 5846 R. A. Sallach  
 8214 M. A. Pound  
 3141 L. J. Erickson (5)  
 3151 W. L. Garner (3)  
 For DOE/TIC (Unlimited Release)  
 3154-3 R. P. Campbell (25)  
 For NRC Distribution to NTIS